POLITECNICO
MILANO 1863

SCUOLA DI INGEGNERIA INDUSTRIALE
E DELL'INFORMAZIONE

Formulation and numerical solution of quantum batteries optimal control problems

Tesi di Laurea Magistrale in
High Performance Computing Engineering - School of Industrial and Information Engineering

Author: **Emanuele Broggini**

Student ID: 222899
Advisor: Prof. Gabriele Ciaramella
Co-advisors: Dr. Kieran Hymas, Dr. James Quach
Academic Year: 2023-2024

Abstract

This thesis investigates the optimal control of a quantum battery system with the aim of maximizing its charging process. We develop a comprehensive model that incorporates interactions between the battery's components, including intermolecular hopping, as well as dissipation and decoherence effects arising from the interaction with the environment. The system dynamics is described using the Lindblad master equation, which is reformulated as a vector-matrix representation to enable numerical analysis and control design. We employ optimal control techniques, specifically the gradient descent method, to maximize the energy charging efficiency. Our analysis focuses on the convergence of the algorithm, the characteristics of the optimal control signal and the achievable energy transitions. We identify regimes of robustness where optimal control strategies remain effective despite the presence of intermolecular hopping and dissipation. Furthermore, we investigate the impact of intermolecular hopping on the system's state connectivity, revealing the emergence of new energy-transfer pathways. Although these new pathways do not contribute significantly to the charging process, their analysis provides valuable insights into the system's dynamics. Although computational limitations prevented us from achieving the initial goal of fully charging the quantum battery to a level capable of powering electronic devices, our study nonetheless provides significant contributions. We demonstrate the feasibility of controlled energy excitations using a time-driving field, highlighting the potential of optimal control techniques for quantum battery applications. Moreover, our in-depth analysis of the system dynamics and robustness provides a valuable foundation for future research aimed at overcoming the identified limitations and further exploring the capabilities of quantum batteries.

Keywords: quantum optics; optimal control; optimality conditions; quantum batteries; optimization; pontryagin maximum principle; gradient descent method; numerical methods for quantum control; quantum mechanics; exact controllability; differential models; numerical optimization

Abstract in lingua italiana

Questa tesi indaga il controllo ottimale di un sistema di batteria quantistica con l'obiettivo di massimizzare il suo processo di carica. Sviluppiamo un modello completo che incorpora le interazioni tra i componenti della batteria, incluso l'hopping intermolecolare, nonché gli effetti di dissipazione e decoerenza derivanti dall'interazione con l'ambiente. La dinamica del sistema è descritta utilizzando la Lindblad master equation, che viene riformulata in una rappresentazione vettore-matrice per consentire l'analisi numerica e la progettazione del controllo. Impieghiamo tecniche di controllo ottimale, in particolare il metodo della discesa del gradiente, per massimizzare l'efficienza della carica energetica. La nostra analisi si concentra sulla convergenza dell'algoritmo, sulle caratteristiche del segnale di controllo ottimale e sulle transizioni energetiche ottenibili. Identifichiamo regimi di robustezza in cui le strategie di controllo ottimale rimangono efficaci nonostante la presenza del termine di hopping intermolecolare e dissipazione. Inoltre, indaghiamo l'impatto del termine di hopping intermolecolare sulla connettività di stato del sistema, rivelando l'emergere di nuovi percorsi di trasferimento di energia. Sebbene questi nuovi percorsi non contribuiscano significativamente al processo di carica, la loro analisi fornisce preziose informazioni sulla dinamica del sistema. Sebbene le limitazioni computazionali ci abbiano impedito di raggiungere l'obiettivo iniziale di caricare completamente la batteria quantistica a un livello in grado di alimentare dispositivi elettronici, il nostro studio fornisce comunque contributi significativi. Dimostriamo la fattibilità di eccitazioni energetiche controllate utilizzando un campo di guida dipendente dal tempo, evidenziando il potenziale delle tecniche di controllo ottimale per le applicazioni di batterie quantistiche. Inoltre, la nostra analisi approfondita della dinamica del sistema e della robustezza fornisce una base preziosa per ricerche future volte a superare le limitazioni identificate e ad esplorare ulteriormente le capacità delle batterie quantistiche.

Parole chiave: ottica quantistica; controllo ottimale; condizioni di ottimalità; batterie quantistiche; ottimizzazione; principio di massimo di Pontryagin; metodo della discesa del gradiente; metodi numerici per il controllo quantistico; meccanica quantistica; controllabilità esatta; modelli differenziali; ottimizzazione numerica

Contents

Abstract **i**

Abstract in lingua italiana **iii**

Contents **v**

1 Introduction **1**
1.1 Context and Objectives 1
1.2 Thesis Structure 1
1.3 Novelty and Contributions 2
1.4 System Description and Lindblad Equation 3

2 Quantum battery modeling through the Lindblad equation **5**
2.1 Introduction to the quantum battery model 5
2.2 Quantum Battery's Hamiltonian 6
2.2.1 The hopping term 15
2.3 Interaction with the environment: Reservoirs and the Lindblad master equation 19
2.3.1 The Electronic Reservoirs $\mathcal{B}$ 21
2.3.2 Lindblad formulation of electrical discharge of the quantum battery 21
2.3.3 Role of Lindblad's superoperators 24

3 Real Formulation of the Lindblad equation **29**
3.1 Formulation of the master equation in a real matrix representation 30
3.1.1 The matrix A 39
3.2 Properties of the matrices A and B and norm preservation 43

4 Optimal Control **47**
4.1 Optimality Conditions 52
4.2 Pontryagin's Maximum Principle (PMP) 55

5 Gradient Descent Method **61**
5.1 Introduction 61
5.2 Application of Gradient descent method to the quantum battery optimization problem 61
5.2.1 The steepest descent algorithm 62

6 Numerical Experiments and Discussion **67**
6.1 Graph Connectivity Analysis 67
6.2 Spectral Properties of Matrix A 70
6.3 Free Evolution of the System 71
6.4 Optimization Results Analysis 75
6.4.1 Methodology and Optimization Parameters 75
6.4.2 System Analysis Without Hopping and Dissipation ($t_h = 0, \Gamma = 0$) . 78
6.4.3 Optimal Control Robustness Analysis 84
6.4.4 Effect of Intermolecular Hopping on State Connectivity 90
6.4.5 Optimization of Transitions with Hopping and Dissipation 93
6.4.6 Optimization of Battery Charge 95

7 Contribution of the Study and Conclusions **99**
7.1 Research Perspectives 100

Bibliography **101**

List of Figures **103**

List of Tables **107**

Acknowledgements **109**

1 | Introduction

This thesis explores the complex dynamics of quantum batteries, focusing on the development and control of an innovative model that extends beyond traditional two-level system representations. The principal objective is to examine and optimize the charging process of these systems, leveraging advanced control techniques to enhance their performance.

1.1. Context and Objectives

The exploration of quantum batteries has attracted significant attention due to their potential to revolutionize energy storage and transfer at the nanoscale. While conventional approaches often simplify molecular systems to two-level representations, our work introduces a more comprehensive model that incorporates additional redox states. This enhancement allows for a more accurate description of charge transport within the molecular subsystem. Furthermore, we explore the application of optimal control theory to manipulate the charging dynamics, with the aim of maximizing the stored energy and efficiency of the quantum battery.

1.2. Thesis Structure

This thesis is structured as follows:

- **Chapter 1: Quantum Battery Modeling Through the Lindblad Equation** This chapter provides a detailed overview of the quantum battery model, including the introduction of additional redox states and the derivation of the Lindblad master equation.
- **Chapter 2: Convenient Formulation of the Lindblad equation** This chapter focuses on transforming the Lindblad equation into a more convenient form for analysis and control design, with the introduction of a real vector-matrix representation of the density matrix and the transformation of the Lindblad equation into a system of differential equations.

- **Chapter 3: Optimal Control** Here, we delve into the application of optimal control techniques to enhance the charging dynamics. The chapter will cover the formulation of the optimal control problem for maximizing the charging efficiency, followed by the introduction of the cost functional and the constraints. Finally, the Pontryagin's Maximum Principle will be articulated, accompanied by a thorough elucidation of its application to the control problem.
- **Chapter 4: Gradient Descent Method** This chapter focuses on the numerical method used to solve the optimal control problem. The subsequent topics will be examined: an introduction to the Gradient Descent method along with its various forms, the implementation specifics of the algorithm concerning the quantum battery control problem and an exploration into the convergence characteristics and the selection of step size.
- **Chapter 5: Numerical Experiments and Discussion** Finally, this chapter presents the results of our simulations, showcasing the effectiveness of the proposed model and control strategies. We analyze the charging dynamics, discuss the impact of various parameters, and compare our findings with existing literature. We summarize the key contributions of this thesis and outline potential avenues for future research.

1.3. Novelty and Contributions

This thesis introduces several novel elements to the study of quantum batteries:

- A refined model that extends beyond two-level systems by incorporating additional redox states, enabling a more accurate description of charge transport.
- The application of optimal control theory to manipulate the charging dynamics, aiming to maximize the stored energy and efficiency of the quantum battery.
- A detailed analysis of the charging process, highlighting the impact of various parameters and control strategies.
- A numerical implementation of the model and control techniques, providing a robust platform for further investigations.

1.4. System Description and Lindblad Equation

The system under study comprises a molecular chain coupled to a cavity, with the dynamics governed by the following Lindblad master equation:

$$\dot{\hat{\rho}} = -i[\hat{H}, \hat{\rho}] + \sum_k \gamma_k \cdot \mathcal{L}[\hat{O}_k \otimes \hat{I}_{cav}](\hat{\rho}) \tag{1.1}$$

where $\hat{H}$ is the Hamiltonian of the quantum battery system, $\hat{\rho}$ is the density matrix, γ_k are dissipation rates, and $\mathcal{L}[\hat{O}_k]$ are Lindblad superoperators. The Hamiltonian, detailed in Section 2.2.1, includes terms for the molecular subsystem, the cavity, their interaction, with the control function $\eta(t)$ embedded within.

By transforming the Lindblad equation into a real-valued matrix form, we obtain the system

$$\dot{x} = Ax + uBx, \tag{1.2}$$

where x denotes a vector representing the density operator matrix, A and B are matrices that direct the evolutionary dynamics of the state, and u pertains to the control function $\eta(t)$. This framework enables the implementation of optimal control techniques to regulate the charging dynamics.

2 | Quantum battery modeling through the Lindblad equation

2.1. Introduction to the quantum battery model

Over the past half century, quantum mechanics has opened up new possibilities in understanding and developing cutting-edge technologies, such as quantum computers, solid-state sensors, and energy devices. One of the growing concepts is quantum batteries, devices that exploit quantum features such as entanglement and coherence to improve energy storage and transformation processes. The exotic and often non-intuitive aspects of quantum physics that underpin the charging of quantum batteries render them an attractive platform for the development of advanced energy storage technologies of the future.

A key part of quantum battery research is the specification of the interactions between the different elements involved, such as molecules, photons, and other constituents of the surrounding environment. In particular, the temporal evolution of such systems can be explained through equations derived from the total Hamiltonian of the system, while also accounting for dissipative effects that arise from the interaction with the environment. Quantum batteries, being open quantum systems, are inevitably subject to dissipative processes that affect their performance. Understanding and controlling these dissipative effects is crucial for optimizing the charging and discharging processes. The dynamics of open quantum systems, including quantum batteries, can be effectively described by the Lindblad master equation, which accounts for the interplay between coherent evolution and dissipative effects.

The growing scientific interest in quantum batteries is primarily motivated by their prospective advancements in energy storage capabilities and their potential to catalyze innovations in sustainable energy technology. Quantum batteries, a notable emerging concept, leverage quantum characteristics such as entanglement and coherence to enhance energy storage and transformation processes. This field attracts substantial scientific

attention owing to its potential to transcend the constraints of classical energy storage systems. One of the most fundamental challenges in developing practical quantum batteries is the ability to efficiently extract the stored energy as an electrical current that can be used to power devices and perform useful work, while minimizing dissipative losses. Recent experimental and theoretical work, such as the study of superabsorption in organic microcavities (Ref. [12]), has demonstrated the potential for superextensive scaling of charging power density. Specifically, these findings indicate that the charging power of a single microcavity containing N_p molecules can significantly exceed that of N_p individual single-molecule microcavities, even when charged simultaneously. This enhanced energy storage capacity, coupled with the increased charging power, makes the exploration and optimization of quantum batteries a crucial area of research for future energy technologies. The specific dissipative processes and their influence on the quantum battery dynamics will be discussed in detail in Section 2.3 where we introduce the Lindblad superoperators and their role in modeling the interaction with the environment.

2.2. Quantum Battery's Hamiltonian

We represent the battery Hamiltonian on the product basis of N_p two-level systems (chromophores) indexed by $1 \leq i \leq N_p$ with a given electronic configuration and the Fock state of the confined photon field (up to some cutoff $N_{ph} > N_p$). For simplicity, chromophore electrons are assumed to be spinless, reducing the configuration space of each chromophore to the four-dimensional basis: $\{|0,0\rangle_i, |1,0\rangle_i, |0,1\rangle_i, |1,1\rangle_i\}$ where $|n_0, n_1\rangle_i$ and n_k represents the number of electrons at the level k of the molecule i.

Using photon annihilation (creation) operators $\hat{a}^{(\dagger)}$ and electron annihilation (creation) operators $\hat{d}_{ik}^{(\dagger)}$ for an electron occupying level k of molecule i. The operators $\hat{a}^{(\dagger)}$ and $\hat{d}_{ik}^{(\dagger)}$ are discussed in more detail below, and their specific matrix representation will be provided.

The most general form of the battery Hamiltonian (written in the rotating reference frame of the laser charger, vide infra) is

$$\begin{aligned}\hat{H}(t) = \Delta_c \hat{a}^\dagger \hat{a} \\ &+ i\eta(t)\cos(\omega t)(\hat{a}^\dagger - \hat{a}) \\ &+ \sum_{i=1}^{N_p} \left(\Delta_0^{(i)} \hat{d}_{i0}^\dagger \hat{d}_{i0} + \Delta_1^{(i)} \hat{d}_{i1}^\dagger \hat{d}_{i1}\right) \\ &+ \sum_{i=1}^{N_p} g^{(i)} \left(\hat{a}^\dagger \hat{d}_{i0}^\dagger \hat{d}_{i1} + \hat{d}_{i1}^\dagger \hat{d}_{i0} \hat{a}\right) \\ &+ t_h \sum_{\langle ij \rangle}^{N_p} \left(\hat{d}_{i0}^\dagger \hat{d}_{j0} + \hat{d}_{i1}^\dagger \hat{d}_{j1} + H.c.\right),\end{aligned} \tag{2.1}$$

where the first term accounts for the number of excitations in the photon field (i.e. photons in the cavity), the second term represents a coherent injection of photons into the cavity via a laser with frequency ω and a temporal profile $\eta(t)$. The third term is the energy stored in the molecules due to a particular redox state and electronic configuration (note that $\Delta_k^{(i)} = \epsilon_k^{(i)} - V_g$ is the bare energy of the level shifted by an externally applied gate voltage). We consider the visible regime, where the energy levels $\epsilon_k^{(i)}$ and the cavity frequency Δ_c are chosen to match typical values for visible light transitions.

Specifically, the HOMO (highest occupied molecular orbital) level $\epsilon_0^{(i)}$ is assumed to be in the range of 1 to 5 eV, and the LUMO (lowest unoccupied molecular orbital) level $\epsilon_1^{(i)}$ is taken to be $\epsilon_0^{(i)}$ plus an energy difference in the range of 1 to 3 eV, corresponding to typical optical bandgaps in the visible range. The cavity frequency Δ_c is chosen to be resonant with the energy difference between the LUMO and HOMO levels, i.e., $\Delta_c \approx \epsilon_1^{(i)} - \epsilon_0^{(i)}$. The penultimate term describes the light-matter interaction between the molecules and the photons confined to the cavity (we have neglected counter-rotating terms here). $g^{(i)}$ represents the intensity of the interaction between the i-th molecule of the chain and the photon field. The final term represents an energy-conserving hopping of electrons between neighboring molecules in the battery. t_h represents the hopping amplitude, that is, the probability or ease with which an electron can jump from one molecule to another in the chain. This parameter is crucial to describe the movement of electrons along the molecular chain. Higher values of t_h mean that electrons can move more freely between molecules.

Although complete, the Hamiltonian proposed in Eq. (2.1) is more easily expressed in the rotating frame of the laser pulse. To transform to the rotating frame, we apply the similarity transformation:

$$\hat{H}^{RWA}(t) = e^{i\xi\omega t}\hat{H}(t)e^{-i\xi\omega t},$$

where ω is the frequency of the laser and $\hat{\xi}$ is the excitation operator

$$\hat{\xi} = \hat{a}^\dagger\hat{a} + \sum_{i=1}^{N_p}\hat{d}_{i1}^\dagger\hat{d}_{i1}.$$

After applying the similarity transformation, performing the necessary algebraic manipulations and making the rotating wave approximation:

$$i\eta(t)\cos(\omega t)(\hat{a}^\dagger - \hat{a}) \approx i\eta(t)\big(e^{-i\omega t}\hat{a}^\dagger - e^{i\omega t}\hat{a}\big),$$

we obtain the rotating frame battery Hamiltonian, which now takes the form:

$$\begin{aligned}\hat{H}^{RWA}(t) = &\tilde{\Delta}_c\hat{a}^\dagger\hat{a}\\ &+ i\eta(t)(\hat{a}^\dagger - \hat{a})\\ &+ \sum_{i=1}^{N_p}\big(\Delta_0^{(i)}\hat{d}_{i0}^\dagger\hat{d}_{i0} + \tilde{\Delta}_1{}^{(i)}\hat{d}_{i1}^\dagger\hat{d}_{i1}\big)\\ &+ \sum_{i=1}^{N_p} g^{(i)}\big(\hat{a}^\dagger\hat{d}_{i0}^\dagger\hat{d}_{i1} + \hat{d}_{i1}^\dagger\hat{d}_{i0}\hat{a}\big)\\ &+ t_h\sum_{\langle ij\rangle}^{N_p}\big(\hat{d}_{i0}^\dagger\hat{d}_{j0} + \hat{d}_{i1}^\dagger\hat{d}_{j1} + H.c.\big),\end{aligned} \tag{2.2}$$

where the quantities $\tilde{\Delta}_c = \Delta_c - \omega$ and $\tilde{\Delta}_1{}^{(i)} = \Delta_1^{(i)} - \omega$ are renormalized by the laser frequency. Of course, in the absence of a laser pulse this Hamiltonian reduces to the original by removing the lasing term and setting $\omega = 0$. We represent this Hamiltonian on the product basis of the Fock state of the photon field and the redox state of each molecule in the ensemble:

$$|n_{ph}\rangle \otimes |n_0^{(1)}, n_1^{(1)}\rangle \otimes \cdots \otimes |n_0^{(N_p)}, n_1^{(N_p)}\rangle\,, \tag{2.3}$$

In the following, the various terms of the Hamiltonian, the operators involved in their formulation, and the chosen basis set for the reduced system are presented in detail. Consistent with the notation employed in Ref. [3], the reduced system, denoted by $\mathcal{S}$,

now comprises the N_p molecules strongly coupled to the photon field within the cavity. The environment, represented by $\mathcal{B}$, consists of the reservoirs (source and drain) that facilitate the exchange of particles and energy with $\mathcal{S}$.

The Reduced System $\mathcal{S}$

It is possible to identify the reduced system as $\mathcal{S}$, i.e., the system of interest. In this context, $\mathcal{S}$ is constituted by the N_p molecules strongly coupled to the photon field within the cavity.

The respective Hilbert spaces associated with the molecules and the confined photon field are denoted by $\mathcal{H}_{\text{mol}}$ and $\mathcal{H}_{\text{cav}}$. The Hilbert space pertaining to $\mathcal{S}$ is represented by $\mathcal{H}_{\mathcal{S}}$, which is formulated as the tensor product between these Hilbert spaces:

$$\mathcal{H}_{\mathcal{S}} = \mathcal{H}_{\text{mol}} \otimes \mathcal{H}_{\text{cav}}. \tag{2.4}$$

The molecular subsystem of the quantum battery This thesis employs a methodology that transcends the conventional representation of two-level systems by including supplementary redox states for each molecule, thereby enhancing the precision of charge transport modeling within the system. Consequently, each molecule is characterized by a four-state basis set, comprising $B_j = \{|\downarrow\rangle, |\uparrow\rangle, |0\rangle, |D\rangle\}$.

For this reason, the dimension of the Hilbert space $\mathcal{H}_{\mathcal{S}}$ depends not only on the number of molecules but also on the number of photon modes considered. Assuming M Fock states for the photon field, and considering the four-state basis for each molecule, the total dimension of the Hilbert space $\mathcal{H}_{\mathcal{S}}$ becomes $4^{N_p} \times M$, namely, $dim\big(\mathcal{H}_{\mathcal{S}}\big) = 4^{N_p} \times M$.

The basis set B_j describes four states for each molecule, related to the distribution of electrons between the HOMO (Highest Occupied Molecular Orbital) and LUMO (Lowest Unoccupied Molecular Orbital) of the individual molecules. In this system, each molecule can exist in one of four electronic states, representing the occupation of the HOMO and LUMO levels by spinless electrons:

- Ground State $\big(|\downarrow\rangle\big)$: $|\downarrow\rangle = |1,0\rangle$: one electron in the HOMO (lower level), zero electron in the LUMO (upper level)
- Excited State $\big(|\uparrow\rangle\big)$: $|\uparrow\rangle = |0,1\rangle$: zero electron in the HOMO (lower level), one electron in the LUMO (upper level)
- Oxidised Molecule $\big(|0\rangle\big)$: $|0\rangle = |0,0\rangle$: no electrons in either HOMO or LUMO

- Reduced Molecule $\big(|1\rangle\big)$: $|1\rangle = |1,1\rangle$: one electron in the HOMO and one electron in the LUMO (both levels are occupied)

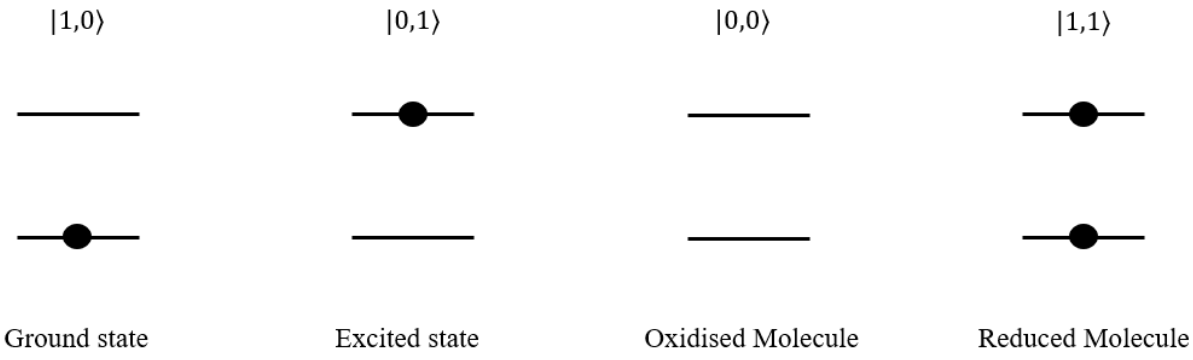

Figure 2.1: A schematic representation of the four possible states for each molecule.

In a classical two-level system (TLS), we consider each molecule as a system with two states: a ground state $|0\rangle$ and an excited state $|1\rangle$. Consequently, the dimension of the Hilbert space for each molecule is 2, and for N_p molecules it becomes 2^{N_p}. This description can be contrasted with the conventional approach to modeling microcavity quantum batteries via Pauli operator techniques, which often employ a simplified two-level representation. Our approach, inspired by the work of Keeling et al. [15], expands upon the state space by accounting for additional electronic configurations, such as oxidized and reduced states, leading to a more comprehensive description of the quantum battery dynamics.

However, with this new basis B_j, each molecule has four distinct states and the Hilbert space of each molecule has dimension 4. So, considering N_p molecules, the overall Hilbert space will have dimension 4^{N_p}, not 2^{N_p} anymore. Therefore, adding extra redox states to the molecular system facilitates the description of charge transport through the quantum battery at the expense of exponentially increasing the dimensionality of the molecular part of the reduced system.

$$\hat{H}_{\text{mol}} = \sum_{i=1}^{N_p} \left(\Delta_0^{(i)} \hat{d}_{i0}^{\dagger} \hat{d}_{i0} + \tilde{\Delta}_1^{(i)} \hat{d}_{i1}^{\dagger} \hat{d}_{i1}\right) \tag{2.5}$$

quantifies the energy stored in the molecular states via electronic occupation of the LUMO and HOMO levels (whose energies Δ_0 and $\tilde{\Delta}_1$ are given relative to the energy of the oxidised molecule). It is important to note that $\Delta_k^{(i)} = \epsilon_k^{(i)} - V_g$ corresponds to the intrinsic energy of the level, which is modified by an external gate voltage V_g.

In regard to the electron (creation) and annihilation operators $d_{ik}^{(\dagger)}$, their actions will be examined in the subsequent paragraph. For the purpose of this model, we focus on the frontier orbitals of the molecules, as these are most likely involved in the low-energy charge transport processes. While the molecules may possess additional excitation levels, we restrict our analysis to the highest occupied molecular orbital (HOMO) and lowest unoccupied molecular orbital (LUMO) to capture the essential dynamics of the quantum battery. These levels are denoted symbolically as 0 and 1; thus, k can exclusively adopt these two values. Within the formulation of the Hamiltonian of the molecular subsystem as presented in Eq. (2.5), the presence of the electron creation and annihilation operators is evident alongside $k = 0, 1$. More specifically, the annihilation operator of an electron $\hat{d}_{i0}$ at ground energy level functions to remove an excitation from level $k = 0$ pertaining to a molecule i, whereas the creation operator $\hat{d}_{i0}^{\dagger}$ generates an electron within the identical energy level for the same molecule i. Likewise, $\hat{d}_{i1}$ and $\hat{d}_{i1}^{\dagger}$ are responsible for the removal and creation of an excitation in the excited level for molecule i.

Some results that we can obtain by applying these operators on the states of the basis B_J are easily derivable as follows:

- Annihilation operator $\hat{d}_{i0}$ annihilates an electron in the ground level for the molecule i:
  - Transport $|1,0\rangle$ to $|0,0\rangle$
  - Transport $|1,1\rangle$ to $|0,1\rangle$
- Creation operator $\hat{d}_{i0}^{\dagger}$ creates an electron in the excited level for the molecule i:
  - Transport $|0,0\rangle$ to $|1,0\rangle$
  - Transport $|0,1\rangle$ to $|1,1\rangle$
- Annihilation operator $\hat{d}_{i1}$ annihilates an electron in the excited level for the molecule i:
  - Transport $|1,1\rangle$ to $|1,0\rangle$
  - Transport $|0,1\rangle$ to $|0,0\rangle$
- Creation operator $\hat{d}_{i1}^{\dagger}$ creates an electron in the excited level for the molecule i:
  - Transport $|0,0\rangle$ to $|0,1\rangle$
  - Transport $|1,0\rangle$ to $|1,1\rangle$

To provide a more concrete understanding of the operators $\hat{d}_{i0}$, $\hat{d}_{i0}^{\dagger}$, $\hat{d}_{i1}$, and $\hat{d}_{i1}^{\dagger}$, we can

express the states $|i,j\rangle$ in their vector representation and derive the corresponding matrix forms of the operators.

Vector Representation of States:

The states $|i,j\rangle$ can be represented as column vectors in the following manner:

$$|\downarrow\rangle = |1,0\rangle = \begin{pmatrix} 0 \\ 1 \\ 0 \\ 0 \end{pmatrix} \quad , \quad |\uparrow\rangle = |0,1\rangle = \begin{pmatrix} 0 \\ 0 \\ 1 \\ 0 \end{pmatrix}$$

$$|0\rangle = |0,0\rangle = \begin{pmatrix} 0 \\ 0 \\ 0 \\ 1 \end{pmatrix} \quad , \quad |1\rangle = |1,1\rangle = \begin{pmatrix} 1 \\ 0 \\ 0 \\ 0 \end{pmatrix}$$

Matrix Representation of Operators:

Based on the actions described above, we can derive the matrix representations of the operators:

$$\hat{d}_{i0} = \begin{pmatrix} 0 & 0 & 0 & 0 \\ 0 & 0 & 0 & 0 \\ 1 & 0 & 0 & 0 \\ 0 & 1 & 0 & 0 \end{pmatrix} \quad , \quad \hat{d}_{i0}^{\dagger} = \begin{pmatrix} 0 & 0 & 1 & 0 \\ 0 & 0 & 0 & 1 \\ 0 & 0 & 0 & 0 \\ 0 & 0 & 0 & 0 \end{pmatrix}$$

$$\hat{d}_{i1} = \begin{pmatrix} 0 & 0 & 0 & 0 \\ 1 & 0 & 0 & 0 \\ 0 & 0 & 0 & 0 \\ 0 & 0 & 1 & 0 \end{pmatrix} \quad , \quad \hat{d}_{i1}^{\dagger} = \begin{pmatrix} 0 & 1 & 0 & 0 \\ 0 & 0 & 0 & 0 \\ 0 & 0 & 0 & 1 \\ 0 & 0 & 0 & 0 \end{pmatrix}$$

These matrix representations can be verified by applying them to the vector representations of the states. For example, applying $\hat{d}_{i0}$ to $|1,0\rangle$ should yield $|0,0\rangle$.

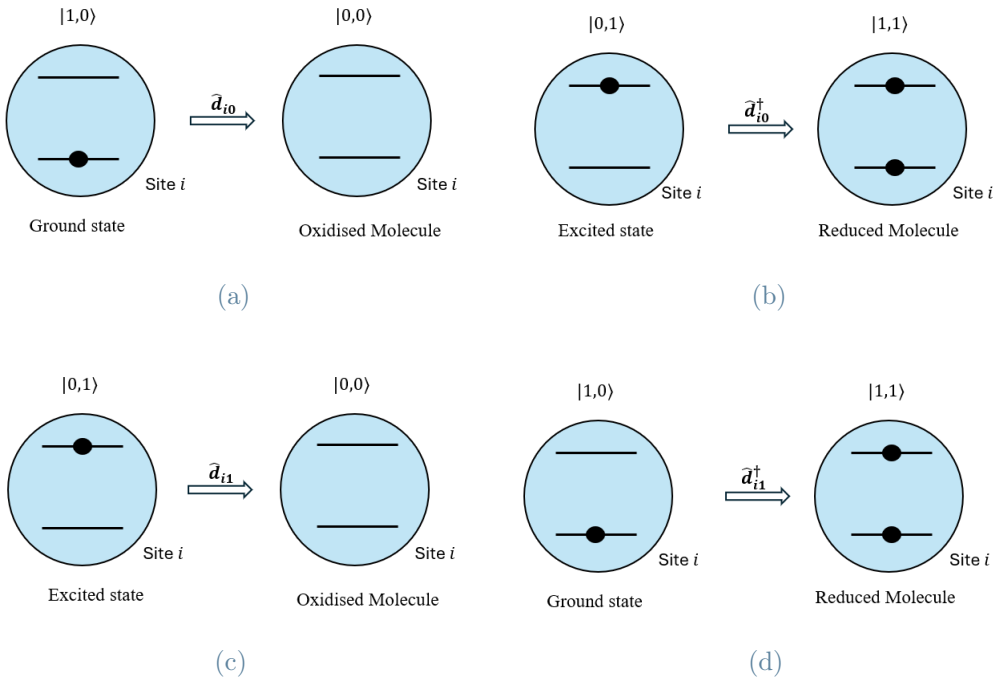

Figure 2.2: A schematic illustration of the processes of electron creation and annihilation as applied to some particular states of B_j.

Cavity Photon Field The photon field confined to the cavity forms an integral part of the microcavity quantum battery. It affords a collective coupling between all of the molecules in the cavity that scales as $\sqrt{N_p}$ in typical Tavis-Cummings quantum battery models [7]. When an electromagnetic field is confined to a finite volume of space by reflective mirrors, the field transforms from a continuum of modes to a quantised collection of allowed modes with energy $\Delta_c(n) = cn\pi/L$ where L is the length of the cavity and c is the speed of light. Here, we consider only the fundamental mode of the cavity field $(n = 1)$ to be hybridised with the molecular ensemble constituting the quantum battery. The state of the photonic component of the wavefunction is simply described by a photon occupation number n_{ph} that counts the number of photons in the fundamental mode of the cavity electromagnetic field.

The Hilbert space $\mathcal{H}_{cav}$ represents the space of photons confined within the cavity. While the number of Fock states for the photon field could be infinite, we consider a finite-dimensional subspace with dimension M for computational tractability. This finite dimension M is chosen to be larger than the number of molecules in the cavity, ensuring that the essential dynamics of the photon field are captured.

The free Hamiltonian of the photons, $\hat{H}_{\text{cav}}$, describes the internal energy of the photon

field and is given by

$$\hat{H}_{\text{cav}} = \tilde{\Delta}_c \hat{a}^\dagger \hat{a}. \tag{2.6}$$

Here, $\tilde{\Delta}_c$ is the cavity frequency Δ_c renormalized by the laser frequency ω: $\tilde{\Delta}_c = \Delta_c - \omega$. This term accounts for the number of excitations in the photon field, i.e., the number of photons in the cavity. The annihilation operator $\hat{a}$ acting on a Fock state $|n_{ph}\rangle$ representing n_{ph} photons or energy quanta, reduces the number of photons by one:

$$\hat{a}\,|n_{ph}\rangle = \sqrt{n_{ph}}\,|n_{ph}-1\rangle\,.$$

Thus, $\hat{a}\,|n_{ph}\rangle$ yields a new state with $n_{ph}-1$ photons, scaled by a factor of $\sqrt{n_{ph}}$. Conversely, the creation operator $\hat{a}^\dagger$ increases the number of particles by one:

$$\hat{a}^\dagger\,|n_{ph}\rangle = \sqrt{n_{ph}+1}\,|n_{ph}+1\rangle\,.$$

The action of $\hat{a}^\dagger$ on $|n_{ph}\rangle$ produces a Fock state with $n_{ph}+1$ photons, scaled by $\sqrt{n_{ph}+1}$. These definitions form the basis for the algebraic treatment of bosonic systems and are crucial for understanding phenomena such as light-matter interactions.

As the photon-number operator is defined by $\hat{n} = \hat{a}^\dagger\hat{a}$, it follows that the Hamiltonian can be expressed as $\hat{H}_{\text{cav}} = \tilde{\Delta}_c\hat{n}$. This representation clearly indicates that $\hat{H}_{\text{cav}}$ captures the energy of the electromagnetic modes present within the cavity.

To further illustrate the action of the creation and annihilation operators, we can represent the Fock states $|n_{ph}\rangle$ as column vectors and derive the corresponding matrix forms of $\hat{a}^\dagger$ and $\hat{a}$.

Vector Representation of Fock States

In the Fock basis, the state $|n_{ph}\rangle$ is represented by a column vector with a 1 in the $(n_{ph}+1)$-th position and 0 elsewhere. For example, some Fock states are

$$|0\rangle = \begin{pmatrix} 1 \\ 0 \\ 0 \\ 0 \\ \vdots \end{pmatrix}, \qquad |1\rangle = \begin{pmatrix} 0 \\ 1 \\ 0 \\ 0 \\ \vdots \end{pmatrix}, \qquad \ldots, \qquad |M\rangle = \begin{pmatrix} 0 \\ 0 \\ 0 \\ \vdots \\ 1 \end{pmatrix}$$

Matrix Representation of Operators

Using the definitions of $\hat{a}$ and $\hat{a}^\dagger$ and the vector representation of Fock states, we can derive their matrix representations. In the Fock basis, these operators are represented by infinite-dimensional matrices

$$\hat{a} = \begin{pmatrix} 0 & \sqrt{1} & 0 & 0 & \cdots \\ 0 & 0 & \sqrt{2} & 0 & \cdots \\ 0 & 0 & 0 & \sqrt{3} & \cdots \\ 0 & 0 & 0 & 0 & \ddots \\ \vdots & \vdots & \vdots & \vdots & \ddots \end{pmatrix}, \qquad \hat{a}^\dagger = \begin{pmatrix} 0 & 0 & 0 & 0 & \cdots \\ \sqrt{1} & 0 & 0 & 0 & \cdots \\ 0 & \sqrt{2} & 0 & 0 & \cdots \\ 0 & 0 & \sqrt{3} & 0 & \ddots \\ \vdots & \vdots & \vdots & \ddots & \ddots \end{pmatrix}.$$

These matrix representations can be verified by applying them to the vector representations of the Fock states. For example, applying $\hat{a}$ to $|2\rangle$ should yield $\sqrt{2}\,|1\rangle$.

Truncation for Numerical Simulations

In practice, for numerical simulations, the infinite-dimensional matrices representing $\hat{a}$ and $\hat{a}^\dagger$ are truncated to a finite size, depending on the number of Fock states considered in the simulation. As stated at the outset of this paragraph, the M parameter will be employed as the finite dimension. This truncation introduces an approximation, but it is generally valid if the probability of occupying high-energy Fock states is negligible.

2.2.1. The hopping term

The intermolecular electron hopping is modeled using a tight-binding approach with the Hamiltonian detailed in

$$\hat{H}_{hop} = t_h \sum_{<ij>}^{N_p} \left(\hat{d}_{i0}^\dagger \hat{d}_{j0} + \hat{d}_{i1}^\dagger \hat{d}_{j1} + H.c. \right) \tag{2.7}$$

and the associated hopping amplitude is specified in t_h. For the sake of simplicity, the electron hopping is assumed to be isoenergetic, which implies that electron transfer takes place exclusively between the HOMO levels or between the LUMO levels of adjacent molecules i and j.

The Light-Matter Interaction

The light-matter interaction between the molecules and the photons confined to the cavity is a crucial aspect of the quantum battery model. It is described by the Hamiltonian term:

$$\hat{H}_{int} = \sum_{i=1}^{N_p} g^{(i)} \left[\hat{d}_{i0}^{\dagger} \hat{d}_{i1} \otimes \hat{a}^{\dagger} + \hat{d}_{i1}^{\dagger} \hat{d}_{i0} \otimes \hat{a} \right]. \tag{2.8}$$

This term, often referred to as the "interaction" Hamiltonian, governs the energy exchange between the molecules subsystem and photons and thus acts on the entire product Hilbert space $\mathcal{H}_{\mathcal{S}}$.

The coupling strength between the i-th molecule and the photon field is given by $g^{(i)}$. This parameter quantifies the strength of the interaction and can, in general, vary for each molecule.

The form of $\hat{H}_{int}$ reflects the fundamental processes involved in light-matter interaction. The term $\hat{d}_{i0}^{\dagger} \hat{d}_{i1} \otimes \hat{a}^{\dagger}$ describes the process in which a molecule absorbs a photon and transitions from its ground state ($|\downarrow\rangle$) to its excited state ($|\uparrow\rangle$). Simultaneously, a photon is created in the cavity mode. In contrast, the term $\hat{d}_{i1}^{\dagger} \hat{d}_{i0} \otimes \hat{a}$ describes the reverse process: a molecule in the excited state emits a photon into the cavity mode and transitions to its ground state.

The summation over i accounts for the interaction of each of the N_p molecules with the photon field. Each molecule can independently absorb or emit photons, contributing to the overall energy exchange within the reduced system.

This interaction Hamiltonian $\hat{H}_{int}$ is essential for the operation of the quantum battery. It provides a mechanism by which energy can be transferred between the molecules and the photon field, enabling the charging and discharging processes. The specific form of H_{int}, and the values of the coupling strengths $g^{(i)}$, will determine the efficiency and characteristics of the energy transfer.

Time-dependent Driving Field

The term $\hat{I}_{\text{mol}} \otimes i\eta(t)(\hat{a}^{\dagger} - \hat{a})$ represents the interaction of the photon field within the cavity with an external, time-dependent driving field. To simplify the notation, we define the time-dependent operator $\hat{V}(t)$ as:

$$\hat{V}(t) = \hat{I}_{\text{mol}} \otimes i\eta(t)(\hat{a}^{\dagger} - \hat{a}). \tag{2.9}$$

This term describes the driving of the photon field within the reduced system $\mathcal{S}$. The presence of the identity operator $\hat{I}_{\text{mol}}$ emphasizes that this driving field acts on the photon field within the cavity, which is part of the reduced system $\mathcal{S}$. This is consistent with the

physical picture where the external control acts directly on the cavity photons, influencing their number and phase, without introducing external degrees of freedom. The time-dependent driving term $\hat{V}(t)$ plays a crucial role in controlling the energy dynamics of the quantum battery, as it allows for the manipulation of the photon population within the cavity, which in turn influences the energy transfer to and from the molecules via the interaction Hamiltonian $\hat{H}_{int}$. In fact, $\eta(t)$ is a real-valued function that modulates the strength of this driving field, effectively acting as a control parameter.

Noting that the imaginary part of the complex amplitude of $\hat{a}$ is given by the quadrature operator $\hat{p} = \frac{i}{2}(\hat{a}^\dagger - \hat{a})$, this term can also be expressed as $2\hat{I}_{\text{mol}} \otimes \eta(t)\hat{p}$.

The Total Hamiltonian

Having defined the individual components of the system's Hamiltonian, we are now equipped to express the total Hamiltonian, which governs the evolution of the system $\mathcal{S}$. The total Hamiltonian is given by:

$$\hat{H} = \hat{H}_{\text{mol}} \otimes \hat{I}_{\text{cav}} + \hat{I}_{\text{mol}} \otimes \hat{H}_{\text{cav}} + \hat{H}_{hop} \otimes \hat{I}_{\text{cav}} + \hat{H}_{int} + \hat{V}(t), \tag{2.10}$$

where

- $\hat{H}_{\text{mol}}$ represents the Hamiltonian of the molecule subsystem.
- $\hat{H}_{\text{cav}}$ represents the Hamiltonian of the photon subsystem.
- $\hat{H}_{hop}$ represents he intermolecular electron hopping.
- $\hat{H}_{int}$ describes the interaction between the two subsystems interacting in the Hilbert space $\mathcal{H}_{\mathcal{S}}$.
- $\hat{V}(t)$ represents the time-dependent driving field in which $\eta(t)$ appears and it will be the object of study and analysis for the optimal control problem.

The inclusion of the identity operators $\hat{I}_{\text{cav}}$ and $\hat{I}_{\text{mol}}$ is crucial to ensure that each term in the total Hamiltonian acts on the appropriate Hilbert space. Specifically:

- $\hat{H}_{\text{mol}} \otimes \hat{I}_{\text{cav}}$ represents the evolution of the molecular subsystem independently of the photons field. The identity operator I_{cav} ensures that $\hat{H}_{\text{mol}}$ acts solely on the Hilbert space $\mathcal{H}_{\text{mol}}$ of the reduced system, leaving the photon subsystem in the optical cavity unaffected.
- $\hat{I}_{\text{mol}} \otimes \hat{H}_{\text{cav}}$ represents the evolution of the photon subsystem independently of the

molecular subsystem. The identity operator $\hat{I}_{\text{mol}}$ ensures that $\hat{H}_{\text{cav}}$ acts solely on the Hilbert space $\mathcal{H}_{\text{cav}}$, leaving the molecules unaltered.

- $\hat{H}_{hop} \otimes \hat{I}_{\text{cav}}$ characterizes the phenomenon of electrons hopping inside the molecular chain; The Kronecker product with the identity operator in the photon's Hilbert space shows this term affects only the molecular dynamics of the reduced system.
- $\hat{H}_{int}$ describes the joint interaction between subsystems constituting the reduced system $\mathcal{S}$, and thus acts on the entire product Hilbert space $\mathcal{H}_{\text{mol}} \otimes \mathcal{H}_{\text{cav}}$.
- The term $\hat{V}(t)$ describes the control applied to the photon field within the cavity and the presence of the identity operator $\hat{I}_{\text{mol}}$ indicates that this control acts exclusively on the photons, leaving the molecular subsystem unaffected.

  To determine an appropriate dimension M of the photon Hilbert space, we ensure that it is at least as large as the number of two-level systems N_p, allowing sufficient photons to invert the entire molecular population. Moreover, the integral over $\eta(t)$ approximates the total photon count injected per pulse, suggesting that M should also account for this total. Therefore, choosing M based on both criteria will enable the coherent injection of photons that can drive molecular excitations effectively. The function $\eta(t)$ can represent various signal shapes, allowing for flexible control strategies. For instance, Ref. [12] demonstrates the use of a Gaussian profile for $\eta(t)$, defined as $\eta(t) = \frac{\eta_0}{\sqrt{2\pi\sigma}} e^{-\frac{(t-t_0)^2}{2\sigma}}$, with the temporal width of the pump pulse $\sigma = 20$ fs, to effectively manipulate the quantum battery's dynamics.

By incorporating the identity operators, we ensure that each term in the total Hamiltonian acts on the appropriate Hilbert space, guaranteeing a consistent description of the evolution of the composite system $\mathcal{S}$.

To simplify the notation, we may define the free Hamiltonian H_0, which delineates the intrinsic dynamics of the system and the bath in isolation, absent any interaction between them:

$$\hat{H}_0 = \hat{H}_{\text{mol}} \otimes \hat{I}_{\text{cav}} + \hat{I}_{\text{mol}} \otimes \hat{H}_{\text{cav}}. \tag{2.11}$$

By subsequently incorporating the influence of the photon field interaction within the cavity $\hat{I}_{\text{mol}} \otimes i\eta(t)(\hat{a}^\dagger - \hat{a})$ alongside the interaction light-matter term $\hat{H}_{int}$, we derive the comprehensive formulation of the total Hamiltonian governing the dynamics of the quantum battery:

$$\hat{H} = \hat{H}_0 + \hat{H}_{hop} \otimes \hat{I}_{\text{cav}} + \hat{H}_{int} + \hat{V}(t). \tag{2.12}$$

2.3. Interaction with the environment: Reservoirs and the Lindblad master equation

In the context of quantum battery development, it is essential to recognize that these devices operate as open systems, inevitably interacting with their environment. In contrast to isolated systems, which evolve in a deterministic manner according to the Schrödinger equation, open systems exchange energy and/or matter with the environment, leading to phenomena such as dissipation and decoherence. While the Schrödinger equation describes the evolution of pure quantum states, the more general framework of the density operator, $\hat{\rho}$, is required to describe mixed states, which arise naturally in open quantum systems due to coupling with the environment. These processes can sometimes facilitate the regulation and enhancement of battery performance; they are fundamental to its physical realization and must be carefully incorporated into the theoretical model. From this perspective, Refs. [12] and [11] provide valuable insights into the manner in which environmental decoherence inhibits the superradiant discharge of the battery. The environment of a quantum battery can be diverse, including photon baths (e.g., incoherent sunlight, indoor lighting), phonon baths (e.g., coupling to longitudinal phonons as in [14]), and fermionic reservoirs (e.g., electrodes for charge extraction). These external influences affect the state and evolution of the quantum system, playing a crucial role in the charging and discharging processes.

Therefore, an accurate description of the dynamics of a quantum battery necessitates a theoretical framework capable of explicitly addressing the interaction with the environment, such as the Lindblad master equation, which will be introduced in the subsequent sections.

In order to model open quantum systems, we examine a system $\mathcal{S}$ engaged in interaction with an environment $\mathcal{B}$. The quantum system of interest, denoted as $\mathcal{S}$, comprises the molecules and the photons within the cavity. These molecules are strongly coupled to the photons, forming a composite system. The surrounding reservoirs (source and drain) are symbolized by $\mathcal{B}$, with which $\mathcal{S}$ exchanges energy and particles. It is crucial to note that the photons within the cavity are not part of the thermal bath $\mathcal{B}$. They are an integral part of the system $\mathcal{S}$ and contribute to its quantum dynamics.

In our quantum battery model, we take a novel approach by considering the electronic component, specifically the electrodes, as the thermal bath $\mathcal{B}$. This differs from the typical treatment where the bath consists of photons or phonons. By modeling the electrodes as a non-interacting electron gas, we can directly incorporate their influence on the system

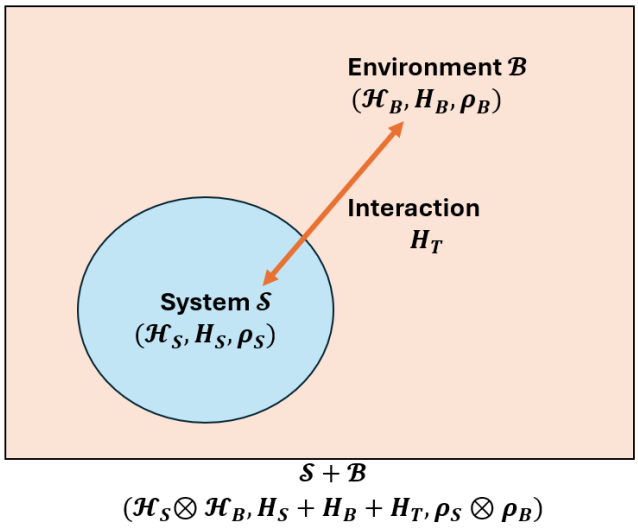

Figure 2.3: A schematic representation of open quantum system.

dynamics and explore the crucial role they play in the charging and discharging processes of the quantum battery.

The entire system $\mathcal{S}+\mathcal{B}$ is assumed to be closed, adhering to Hamiltonian dynamics. Nonetheless, the interactions between $\mathcal{S}$ and $\mathcal{B}$ result in the dynamics of $\mathcal{S}$ alone, known as reduced system dynamics, deviating from pure unitary behavior and being affected by these interactions.

Let $\mathcal{H}_\mathcal{S}$ symbolize the Hilbert space of the system $\mathcal{S}$, and $\mathcal{H}_\mathcal{B}$ stand for the Hilbert space of the environment $\mathcal{B}$. Consequently, the Hilbert space $\mathcal{H}$ of the total system is expressed through the tensor product

$$\mathcal{H} = \mathcal{H}_\mathcal{S} \otimes \mathcal{H}_\mathcal{B}.$$

This study aims to explore a quantum battery system in which the reduced system $\mathcal{S}$ comprises N_p molecules with two energy levels, showing strong coupling to a photon field within a cavity. The system's Hamiltonian incorporates elements of light-matter interaction, an external radiation field depicted by $\eta(t)$, and a coupling between the molecules and the photon field. The primary goal of this thesis is to investigate the temporal evolution of the system under the influence of an external control $\eta(t)$, with the intention of enhancing the efficiency of energy transfer between photons and molecules in the presence of a fermonic leads that facilitate charge separation and energy extraction as an electrical current.

2.3.1. The Electronic Reservoirs $\mathcal{B}$

In the context of our quantum battery model, the environment $\mathcal{B}$ is represented by a thermal bath, specifically the reservoirs (source and drain), which play a crucial role in the system's dynamics. The bath can be defined as an environment with an ∞ number of degrees of freedom such that the frequencies of the reservoir modes form a continuum. The term 'bath' can be used for a reservoir that is in a thermal equilibrium state.

These reservoirs are macroscopic systems maintained at thermal equilibrium, characterized by a constant temperature and chemical potential. Their primary function is to interact with the reduced system $\mathcal{S}$ (molecules and photons) through the exchange of both energy and particles.

The reservoirs are assumed to be significantly larger than the reduced system $\mathcal{S}$, ensuring that their equilibrium state remains largely unaffected by the interactions with $\mathcal{S}$. This assumption is essential for treating $\mathcal{B}$ as a true thermal bath, capable of providing a stable environment for the quantum battery.

The Hilbert space of the thermal bath $\mathcal{B}$ is denoted as $\mathcal{H}_{\mathcal{B}}$, which is the space of the reservoirs. Due to the macroscopic nature of the reservoirs, the dimension of $\mathcal{H}_{\mathcal{B}}$ is considerably larger than the dimension of $\mathcal{H}_{\mathcal{S}}$ reflecting the vast number of degrees of freedom in the thermal bath.

In our model, we focus on the interaction between the reduced system $\mathcal{S}$ and the thermal bath $\mathcal{B}$, rather than on the detailed microscopic description of the reservoirs themselves. This approach is consistent with many models of open quantum systems, where the environment is treated as a bath providing statistical influences on the system. Therefore, we do not explicitly specify a detailed Hamiltonian for the reservoirs, but rather describe their influence through interaction terms with the reduced system. This simplification allows us to concentrate on the essential dynamics of the quantum battery, namely the energy and particle exchange between molecules, photons, and the reservoirs, without the need for a complex microscopic model of the bath.

2.3.2. Lindblad formulation of electrical discharge of the quantum battery

To model the time-evolution of the open quantum battery under external driving from a laser field $\eta(t)$ we utilise a Lindblad master equation for the reduced density operator $\eta(t)$ of the quantum battery. Importantly, $\eta(t)$ contains dynamical information concerning the matter and the photonic degrees of freedom of the battery and allows for the calculation

of useful thermodynamic quantities such as energy stored in the battery as function of time. The quantum battery is open in the sense that charge carriers can be exchanged with two fermionic leads (depicted schematically in Fig.2.4). The detailed dynamics of the fermionic leads are assumed unimportant for the detailed time-evolution of the reduced density operator $\eta(t)$ and thus are treated as memoryless Markovian reservoirs in the Born approximation.

The influence of charge transport through the quantum battery is thus captured at the level of an effective Lindblad equation where the correlation functions of the leads are Fermi-Dirac functions $f(\epsilon) = (1 + \exp((\epsilon_f - V_b)/(kT)))^{-1}$ whose Fermi energy is shifted by an external bias voltage V_b. Illustrated below is a schematic representing the coupling between the electrode and the quantum battery, wherein the colored arrows indicate the electron exchange between each subsystem, corresponding with the Lindblad master equation introduced subsequently. The quantum battery itself consists of N_p two-level systems. Unlike existing models that utilize a simplified Pauli spin framework, our approach employs a frontier molecular orbital picture of the molecules constituting the battery. In this model, we account for electron population across the highest occupied molecular orbital (HOMO) and lowest unoccupied molecular orbital (LUMO) of the optical absorbers. This model expands upon the state space of a simple Pauli spin approach by accounting also for oxidized and reduced states of the molecules, providing a more detailed description of the electronic dynamics within the quantum battery.

The explicit form of the Linblad equation used in this work is

$$
\begin{aligned}
\dot{\hat{\rho}} = &-i[\hat{H}, \hat{\rho}] \\
&+ \Gamma f\left(\epsilon_F + \Delta_0^{(1)} - V_b\right) \mathcal{L}[\hat{d}_{10}^{\dagger} \otimes \hat{I}_{cav}](\hat{\rho}) \\
&+ \Gamma f\left(\epsilon_F + \Delta_1^{(1)} - V_b\right) \mathcal{L}[\hat{d}_{11}^{\dagger} \otimes \hat{I}_{cav}](\hat{\rho}) \\
&+ \Gamma\left(1 - f\left(\epsilon_F + \Delta_0^{(1)} - V_b\right)\right) \mathcal{L}[\hat{d}_{10} \otimes \hat{I}_{cav}](\hat{\rho}) \\
&+ \Gamma\left(1 - f\left(\epsilon_F + \Delta_1^{(1)} - V_b\right)\right) \mathcal{L}[\hat{d}_{11} \otimes \hat{I}_{cav}](\hat{\rho}) \\
&+ \Gamma f\left(\epsilon_F + \Delta_0^{(N_p)} + V_b\right) \mathcal{L}[\hat{d}_{N_p 0}^{\dagger} \otimes \hat{I}_{cav}](\hat{\rho}) \\
&+ \Gamma f\left(\epsilon_F + \Delta_1^{(N_p)} + V_b\right) \mathcal{L}[\hat{d}_{N_p 1}^{\dagger} \otimes \hat{I}_{cav}](\hat{\rho}) \\
&+ \Gamma\left(1 - f\left(\epsilon_F + \Delta_0^{(N_p)} + V_b\right)\right) \mathcal{L}[\hat{d}_{N_p 0} \otimes \hat{I}_{cav}](\hat{\rho}) \\
&+ \Gamma\left(1 - f\left(\epsilon_F + \Delta_1^{(N_p)} + V_b\right)\right) \mathcal{L}[\hat{d}_{N_p 1} \otimes \hat{I}_{cav}](\hat{\rho})
\end{aligned}
\tag{2.13}
$$

which describes the dynamics of the reduced density operator of the quantum battery,

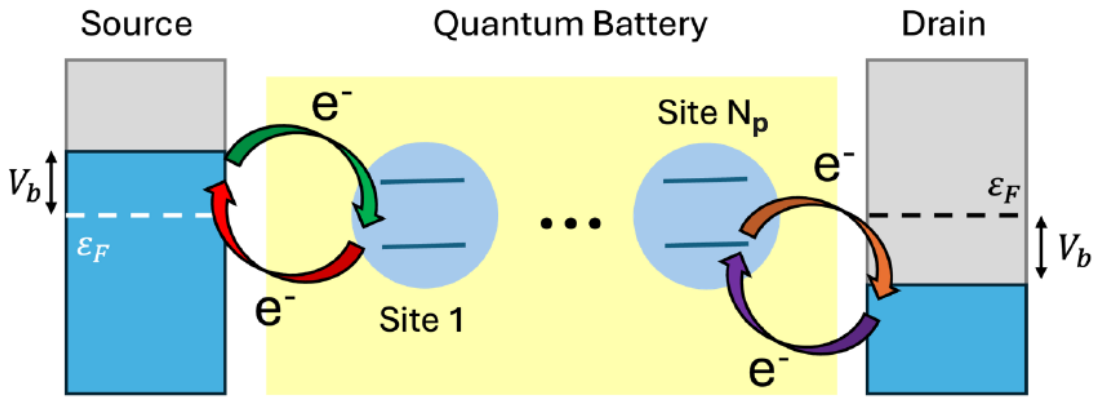

Figure 2.4: Schematic representation of the quantum battery model, illustrating the coupling between the battery and the electrodes. The system consists of N_p molecular sites (blue circles) representing the quantum battery, connected to a source and drain electrode. The electrodes are modeled as fermionic reservoirs with a bias voltage V_b applied between them, creating a difference in their Fermi levels (ϵ_F). The arrows indicate the flow of electrons (e^-) between the electrodes and the molecular sites, highlighting the charging and discharging processes. The red and green arrows represent electron transfer from the source to the battery, while the orange and purple arrows represent electron transfer from the battery to the drain.

coupled to the two electronic reservoirs with interaction strength set by Γ. Notably, electrons can hop to and from molecules that are proximal to the leads (i.e. the first and N_p^{th} molecule in the quantum battery chain). The Lindblad in Eq.(2.13) was written using different colors to highlight the electron flows between the sites of the quantum battery. The colors used in Eq.(2.13) correspond to those in Figure 2.4, which shows a schematic representation of the quantum battery with colored arrows indicating the electron flows. In particular, the Lindblad terms that have the same color represent the same electron flow as described in Figure 2.4. For example, the red term in Eq.(2.13) represents the electron flow from site 1 to the source, as shown by the red arrow in Figure 2.4. Similarly, the green term represents the flow from the source to site 1, and so on for the other colors.

The physical significance of Γ can be understood as the charge hopping rate between the quantum battery and the leads. An increased Γ denotes a more rapid exchange of electrons between the quantum battery and the reservoirs, thereby facilitating accelerated relaxation and charge transfer (dissipation). In contrast, a reduced Γ indicates a weaker coupling between the system and the reservoirs, with dissipative effects emerging over an extended timescale. Generally, its value, often within the range of $10^8 - 10^{10} s^{-1}$ for numerous physical systems, establishes the characteristic timescale over which the

quantum battery experiences charging or discharging through incoherent processes. The charge hopping rate is integral in defining both the velocity and efficacy of the electrical discharge (or charging) process in the quantum battery, as it directly regulates the rate at which dissipation and decoherence proceed via the Lindblad superoperators.

In quantum transport models, $f(\epsilon)$ modulates the rates of electron injection and extraction. For example, a term like $\Gamma \cdot f(\epsilon_F + \Delta - V_b)$ indicates that the efficiency of charge transfer depends on the thermal probability that the state with energy $\epsilon_F + \Delta - V_b$ is occupied. Such microscopic models have been developed and used successfully to explain phenomena in electronic and spin transport experiments (Ref.[6, 8, 9, 13]).

$\mathcal{L}[\hat{O}\otimes\hat{I}_{cav}](\hat{\rho})$ corresponds to the Lindblad super operators acting on the reduced quantum system. Their action and and their fundamental role in the evolution of the system dynamics will be discussed extensively later in this chapter.

2.3.3. Role of Lindblad's superoperators

Within the framework of our model, Lindblad superoperators are exclusively applied to the boundary molecules, specifically the first and last molecules in the chain. This approach accurately represents the physical reality of the system, whereby the source and drain (or the associated fermionic reservoirs) are directly coupled solely to the molecules in direct contact with them. Consequently, the dissipative processes responsible for charge injection and extraction are confined to these boundary sites. The molecules situated within the interior of the quantum battery remain substantially decoupled from the reservoirs and predominantly evolve under coherent dynamics dictated by the system Hamiltonian.

In the context of the quantum battery model, the Lindblad superoperators take the general form:

$$\mathcal{L}[\hat{O} \otimes \hat{I}_{cav}](\hat{\rho}) = (\hat{O} \otimes \hat{I}_{cav})\hat{\rho}(\hat{O}^\dagger \otimes \hat{I}^\dagger_{cav}) - \frac{1}{2}\{(\hat{O}^\dagger \otimes \hat{I}^\dagger_{cav})(\hat{O} \otimes \hat{I}_{cav}), \hat{\rho}\}. \tag{2.14}$$

In this context, $\hat{O}$ denotes an operator governing the interaction between the molecular subsystem of the quantum battery and the reservoirs, while $\hat{I}_{cav}$ serves as the identity operator within the cavity subsystem. The curly brackets indicate the anti-commutator. This representation elucidates that the Lindblad superoperator $\mathcal{L}[\hat{O}]$ operates non-trivially solely on the molecular component of the density matrix, thereby maintaining the cavity subsystem unaffected.

To model these irreversible processes, the Lindblad master equation introduces additional

terms in the form of superoperators:

$$\dot{\hat{\rho}} = -i[\hat{H}, \hat{\rho}] + \sum_k \gamma_k \mathcal{L}[\hat{O}_k \otimes \hat{I}_{cav}](\hat{\rho}), \tag{2.15}$$

where each Lindblad superoperator is defined as seen in Eq. (2.14).

The sum in Eq. (2.15) is a compact notation to represent the eight terms appearing in the extended Lindblad equation (Eq. (2.13)), which describes the specific interaction of the quantum battery with the charge reservoirs:

$$\begin{aligned}
\Gamma \Bigg[& f\left(\epsilon_F + \Delta_0^{(1)} - V_b\right) \mathcal{L}[\hat{d}_{10}^\dagger \otimes \hat{I}_{cav}] + f\left(\epsilon_F + \Delta_1^{(1)} - V_b\right) \mathcal{L}[\hat{d}_{11}^\dagger \otimes \hat{I}_{cav}] \\
& + \left(1 - f\left(\epsilon_F + \Delta_0^{(1)} - V_b\right)\right) \mathcal{L}[\hat{d}_{10} \otimes \hat{I}_{cav}] + \left(1 - f\left(\epsilon_F + \Delta_1^{(1)} - V_b\right)\right) \mathcal{L}[\hat{d}_{11} \otimes \hat{I}_{cav}] \\
& + f\left(\epsilon_F + \Delta_0^{(N_p)} + V_b\right) \mathcal{L}[\hat{d}_{N_p0}^\dagger \otimes \hat{I}_{cav}] + f\left(\epsilon_F + \Delta_1^{(N_p)} + V_b\right) \mathcal{L}[\hat{d}_{N_p1}^\dagger \otimes \hat{I}_{cav}] \\
& + \left(1 - f\left(\epsilon_F + \Delta_0^{(N_p)} + V_b\right)\right) \mathcal{L}[\hat{d}_{N_p0} \otimes \hat{I}_{cav}] + \left(1 - f\left(\epsilon_F + \Delta_1^{(N_p)} + V_b\right)\right) \mathcal{L}[\hat{d}_{N_p1} \otimes \hat{I}_{cav}] \Bigg]
\end{aligned}$$

To have a better general overview of the various terms, in Eq. (2.15), the coefficients γ_k and the Lindblad superoperators $\mathcal{L}[\hat{O}_k]$ correspond to the terms in Eq. (2.13) as follows:

- $\gamma_1 = \Gamma f\left(\epsilon_F + \Delta_0^{(1)} - V_b\right)$, $\hat{O}_1 = \hat{d}_{10}^\dagger$
- $\gamma_2 = \Gamma f\left(\epsilon_F + \Delta_1^{(1)} - V_b\right)$, $\hat{O}_2 = \hat{d}_{11}^\dagger$
- $\gamma_3 = \Gamma\left(1 - f\left(\epsilon_F + \Delta_0^{(1)} - V_b\right)\right)$, $\hat{O}_3 = \hat{d}_{10}$
- $\gamma_4 = \Gamma\left(1 - f\left(\epsilon_F + \Delta_1^{(1)} - V_b\right)\right)$, $\hat{O}_4 = \hat{d}_{11}$
- $\gamma_5 = \Gamma f\left(\epsilon_F + \Delta_0^{(N_p)} + V_b\right)$, $\hat{O}_5 = \hat{d}_{N_p0}^\dagger$
- $\gamma_6 = \Gamma f\left(\epsilon_F + \Delta_1^{(N_p)} + V_b\right)$, $\hat{O}_6 = \hat{d}_{N_p1}^\dagger$
- $\gamma_7 = \Gamma\left(1 - f\left(\epsilon_F + \Delta_0^{(N_p)} + V_b\right)\right)$, $\hat{O}_7 = \hat{d}_{N_p0}$
- $\gamma_8 = \Gamma\left(1 - f\left(\epsilon_F + \Delta_1^{(N_p)} + V_b\right)\right)$, $\hat{O}_8 = \hat{d}_{N_p1}$

These terms are fundamentally responsible for the dissipation and decoherence in the system.

Dissipation The dissipative part of the dynamics introduces irreversible processes, such as energy relaxation or charge transfer. In our model, these processes account for the incoherent charge transport between the quantum battery and the fermionic reservoirs. The Lindblad terms ensure that, even though the coherent part of the evolution (given by $-i[\hat{H}, \hat{\rho}]$) would preserve the state's norm, the net evolution results in a decay of excitations or a redistribution of population among the available energy levels.

Decoherence In addition to energy dissipation, the Lindblad superoperators also lead to the loss of quantum coherence. The anti-commutator part $\frac{1}{2}\{\hat{O}^\dagger\hat{O}, \hat{\rho}\}$ acts to suppress off-diagonal elements of $\hat{\rho}$ in the energy eigenbasis, which corresponds to the loss of quantum correlations (coherence) in the system.

Thus, while the term $-i[\hat{H}, \hat{\rho}]$ governs the reversible, unitary evolution of the system, it is the Lindblad terms that are solely responsible for the non-unitary effects, namely, dissipation and decoherence. In the context of our quantum battery, these dissipative terms are crucial; they not only model the electron transport (charging/discharging) processes but also capture the irreversible loss of coherence due to the interaction with the reservoirs.

In summary, the full Lindblad equation (2.15) combines the reversible unitary dynamics (through the commutator) with the irreversible dissipative dynamics (through the Lindblad superoperators). This combination is essential for accurately describing open quantum systems such as the quantum battery, where both coherent evolution and environmental interactions (dissipation and decoherence) play pivotal roles.

Physical Interpretation of the Lindblad Terms Each Lindblad superoperator in Eq. (2.13) corresponds to a specific physical process governing electron exchange between the quantum battery and the reservoirs:

- **Electron Injection ($\mathcal{L}[\hat{d}^\dagger_{p\sigma}]$)** These terms describe the process by which an electron is injected from the reservoir into the quantum battery.
- **Electron Extraction ($\mathcal{L}[\hat{d}_{p\sigma}]$)** These terms model the extraction of an electron from the quantum battery into the reservoir.

The interplay between the coherent evolution dictated by the Hamiltonian and the dissipative terms introduced by the Lindblad superoperators determines the steady-state properties of the quantum battery, influencing key physical properties, such as charge accumulation and relaxation dynamics. By systematically incorporating Lindblad superoperators, the proposed model offers a flexible approach to describe the realistic charge dynamics of a quantum battery, accounting for both coherent and dissipative transport

mechanisms.

3 | Real Formulation of the Lindblad equation

The Lindblad master equation, as delineated in the preceding chapter, offers a comprehensive framework for elucidating the dynamics of open quantum systems in the context of our quantum battery model, capturing the sophisticated interrelation between coherent evolution and dissipative processes. Nevertheless, the intrinsic complexity of the operator formalism poses considerable obstacles in practical computations and further analytical efforts.

The vector-matrix formulation presented in this thesis offers two significant advantages: firstly, it avoids the complexities associated with calculations in the complex domain, simplifying numerical simulations. Secondly, it facilitates the study of system properties by transforming the master equation into a more tractable form, enabling the application of linear algebra techniques and providing deeper insights into the system's behavior. The computational challenges encountered when operating within the complex domain are notably significant in the realm of quantum optimal control, where the adept manipulation of the system's evolution is paramount.

To overcome these constraints and harness the full potential of the Lindblad formalism, we undertake a pivotal transformation: the conversion to a real matrix representation. This transition extends beyond a mere mathematical convenience; this is a strategic step that bridges the gap between the abstract world of operators and the concrete realm of efficient numerical computation and control theory. By reformulating the Lindblad equation in terms of real-valued matrices and vectors, we avail ourselves of a powerful array of tools.

From a computational point of view, using real matrix representation reduces computational complexity, conserving memory and processing power by avoiding complex-valued operators. This is crucial for systems with many degrees of freedom, where Hilbert space dimensions can expand significantly. Techniques in quantum optimal control, including gradient-based and variational approaches, rely on real parameters. The real matrix form of the Lindblad equation is crucial for developing control protocols to improve quantum

battery performance. Furthermore, real matrix representations often uncover latent structures and symmetries in system dynamics, aiding in developing analytical approximations, clarifying fundamental mechanisms and guiding control strategy design.

The transition to a real matrix representation is particularly crucial when considering quantum optimal control problems. As highlighted in Ref. [2], [4], [5], many applications, including NMR spectroscopy, spin dynamics and quantum information processing, require the precise and efficient manipulation of quantum states. These control problems often involve minimizing a cost functional that depends on both the state of the system and the applied control fields. The real matrix formulation of the Lindblad equation allows us to leverage powerful optimization techniques from control theory, such as gradient-based methods and Newton-type algorithms. Furthermore, as discussed in [2], [4], [5], the matrix representation is essential for handling control constraints, which are often encountered in practical applications, such as limitations on the intensity of radiofrequency pulses in NMR. The ability to efficiently compute control functions, while satisfying these constraints, is paramount for achieving high fidelity and performance in quantum control tasks.

In the next chapter, we shall provide a comprehensive exposition on the transformation from the Lindblad equation in its operator format to its corresponding real matrix representation. This entails the construction of an appropriate basis for the operator space, the expression of the density matrix and the Lindblad superoperator in this basis, and the derivation of the ensuing real-valued equation of motion. This real matrix formulation will serve as the foundation for our subsequent investigation of quantum optimal control strategies applied to the quantum battery system.

3.1. Formulation of the master equation in a real matrix representation

In order to emphasize the importance, the operator-based formulation of the Lindblad equation presents significant computational challenges, especially for larger systems. To overcome these limitations, we now transform the Lindblad equation into a real matrix representation, which will be crucial for our subsequent analysis and control design.

Construction of the basis

To represent the Lindblad equation in matrix form, we need a suitable basis for the space of operators acting on the Hilbert space $\mathcal{H}_S = \mathcal{H}_{\text{mol}} \otimes \mathcal{H}_{\text{cav}}$ related to the reduced

system. A convenient choice is to construct an orthonormal basis consisting of Hermitian operators. We first construct orthonormal bases for the individual Hilbert spaces $\mathcal{H}_{\text{mol}}$ and $\mathcal{H}_{\text{cav}}$, and then combine them using the Kronecker product.

Basis for $\mathcal{H}_{\text{mol}}$ We define $N = 4^{N_p}$, where N_p is the number of molecules and this represents the dimensionality of the Hilbert space $\mathcal{H}_{\text{mol}}$. The space of Hermitian operators acting on $\mathcal{H}_S$ has dimension $N^2 = 4^{2N_p}$. A basis for this space, denoted as $\mathfrak{her}(N)$, is generated by the Kronecker product of $2N_p$ matrices. These matrices are combinations of the identity matrix I_2 and the Pauli matrices $\{\sigma_\alpha\}_{\alpha\in\{0,x,y,z\}}$.

$$\sigma_0 = \begin{pmatrix} 1 & 0 \\ 0 & 1 \end{pmatrix}, \quad \sigma_x = \begin{pmatrix} 0 & 1 \\ 1 & 0 \end{pmatrix}, \quad \sigma_y = \begin{pmatrix} 0 & -i \\ i & 0 \end{pmatrix}, \quad \sigma_z = \begin{pmatrix} 1 & 0 \\ 0 & -1 \end{pmatrix}.$$

Here, $\sigma_0 = I_2$ is the 2×2 identity matrix, and σ_x, σ_y, and σ_z are the Pauli matrices.

Each element of the basis for $\mathcal{H}_S$ is therefore given by

$$\hat{B}_{(\alpha_1,\ldots,\alpha_{N_p})} = \sigma_{\alpha_1} \otimes \sigma_{\alpha_2} \otimes \cdots \otimes \sigma_{\alpha_{2N_p}}, \quad i = 1, \ldots, N^2,$$

where each σ_{α_j} is one of the four Pauli matrices. Each basis matrix $\hat{B}_i$ has dimension $(N \times N)$, i.e., $(4^{N_p} \times 4^{N_p})$. This construction yields a basis with $N^2 = 4^{2N_p}$ elements $\hat{B}_{(\alpha_1,\ldots,\alpha_{N_p})}$.

Using the matrices described above, we construct a basis for $\mathfrak{her}(N)$:

$$\hat{\mathcal{B}}_{N_p} = \{\hat{B}_{(\alpha_1,\ldots,\alpha_{N_p})} \mid \alpha_k \in \{0, x, y, z\}\}. \tag{3.1}$$

Introducing the following inner product on the space $\mathfrak{her}(N)$:

$$\langle A, B\rangle = \text{Tr}(A^\dagger B) \text{ for } A, B \in \mathfrak{her}(N) \tag{3.2}$$

with the usual notation in which $\dagger$ denotes the transpose conjugate and the trace Tr is applied on the matrices product. The scalar product induces the Hilbert-Schmidt norm:

$$||A|| = \sqrt{\langle A^\dagger A\rangle} = \sqrt{\text{Tr}(A^\dagger A)}. \tag{3.3}$$

Noticing that the basis $\hat{\mathcal{B}}_{N_p}$ results to be orthogonal with respect to the inner product,

we observe that:

$$\mathrm{Tr}(\hat{B}_i^\dagger \hat{B}_k) = \delta_{ik} \cdot 4^{N_p}, \tag{3.4}$$

where δ_{ik} is the Kronecker delta and the elements $\hat{B}_i$ that belongs to $\hat{\mathcal{B}}_{N_p}$ have norm equal to $\sqrt{4^{N_p}}$. The basis can be normalized by multiplying all its elements by the normalization factor $\beta_{N_p} := 1/\sqrt{4^{N_p}}$, obtaining the following orthonormal basis:

$$\hat{\mathcal{B}}_{N_p} = \{\tilde{B}_{(\alpha_1,\ldots,\alpha_{N_p})} := \beta_{N_p} \hat{B}_{(\alpha_1,\ldots,\alpha_{N_p})} \mid \alpha_k \in \{0, x, y, z\}\}. \tag{3.5}$$

Basis for $\mathcal{H}_{\mathbf{cav}}$ The space of Hermitian operators $\mathfrak{her}(M)$ acting on $\mathcal{H}_{\mathrm{cav}}$ has dimension M^2, namely, $\dim\big(\mathfrak{her}(M)\big) = M^2$. A basis for this space, denoted by $\hat{\mathcal{B}}_M$, is constructed using orthonormal Hermitian matrices $\tilde{B}_j$, where $j = 1, \ldots, M^2$.

For $M = 2$, the Pauli matrices, as defined in the previous section, form a suitable basis. For $M > 2$, we generalize this construction to obtain a set of M^2 orthonormal Hermitian matrices. Specifically, we construct the basis by considering diagonal matrices, and then specific combinations of off-diagonal elements that ensure hermiticity. We first create a set of M diagonal matrices, where each matrix has a single non-zero element (equal to 1) on the diagonal. Then, for each pair of indices (i, j) with $i < j$, we construct two matrices: one with real values (1 at positions (i, j) and (j, i)), and another with imaginary values ($-i$ at position (i, j) and i at position (j, i)). These matrices are then combined linearly to form M^2 orthonormal Hermitian matrices. Finally, all the constructed matrices are normalized such that $\mathrm{Tr}(\tilde{B}_j^\dagger \tilde{B}_l) = \delta_{jl}$, where δ_{jl} is the Kronecker delta. This procedure yields a set of M^2 orthonormal Hermitian matrices $\hat{\mathcal{B}}_M$, each of dimension $M \times M$.

Total basis for $\mathcal{H}_{\mathcal{S}}$ The basis formed by hermitian matrices for the total Hilbert space $\mathcal{H}_{\mathcal{S}} = \mathcal{H}_{\mathrm{mol}} \otimes \mathcal{H}_{\mathrm{cav}}$ is then formed by taking the Kronecker product of the individual bases:

$$\widehat{B}_{ij} = \hat{B}_i \otimes \tilde{B}_j, \quad i = 1, \ldots, N^2, \quad j = 1, \ldots, M^2.$$

The dimension of this total basis is $N^2 \times M^2$, namely $\dim\big(\mathfrak{her}(N \times M)\big) = N^2 \times M^2$. We can define the basis for the total Hilbert space $\mathcal{H}$ as $\mathcal{B}$:

$$\mathcal{B} = \{\widehat{B}_{ij} = \hat{B}_i \otimes \tilde{B}_j \mid \hat{B}_i \in \mathcal{B}_{N_p}, \quad \tilde{B}_j \in \mathcal{B}_M, \quad i = 1, \ldots, N^2, \quad j = 1, \ldots, M^2\}. \tag{3.6}$$

Matrix representation of the density operator

Using the set of bases $\mathcal{B} = \{\widehat{B}_{ij}\}$, where $i = 1, \ldots, N^2$ and $j = 1, \ldots, M^2$, obtained from the Kronecker product between the operator bases acting in the different Hilbert spaces $\mathcal{H}_S$ and $\mathcal{H}_B$, the density operator $\hat{\rho}$ can be represented as a vector of real values x of dimension $N^2 \times M^2$. To establish this representation, we first define the linear map $V : \mathfrak{her}(N \times M) \to \mathbb{R}^{N^2 \times M^2}$ as

$$V(\hat{\rho}) = \Big(\langle \hat{\rho}|\widehat{B}_1\rangle, \langle \hat{\rho}|\widehat{B}_2\rangle, \ldots, \langle \hat{\rho}|\widehat{B}_{N^2\times M^2}\rangle\Big)^T, \tag{3.7}$$

where $\langle\cdot|\cdot\rangle$ is the inner product defined in (3.2). This map associates the density operator $\hat{\rho}$ with a unique vector in $\mathbb{R}^{N^2\times M^2}$. Using this map, we can express the density operator $\hat{\rho}$ as a linear combination of the basis elements:

$$\hat{\rho} = \sum_{i=1}^{N^2}\sum_{j=1}^{M^2} x_{(i-1)M^2+j}\hat{B}_{ij} = \sum_{i=1}^{N^2}\sum_{j=1}^{M^2} x_{(i-1)M^2+j}(\hat{B}_i \otimes \tilde{B}_j),$$

where the coefficients $x_{(i-1)M^2+j}$ are given by $x_{(i-1)M^2+j} = \langle\hat{\rho}|\hat{B}_i \otimes \tilde{B}_j\rangle = \mathrm{Tr}\big((\hat{B}_i \otimes \tilde{B}_j)^\dagger\hat{\rho}\big)$, $i = 1, \ldots, N^2, j = 1, \ldots, M^2$, and are real valued due to the hermiticity of $\hat{\rho}$ and $\hat{B}_{ij}$. The generalized Bloch vector $x = (x_1, x_2, \ldots, x_{N^2\times M^2})^T := V(\hat{\rho})$ is then formed by arranging these coefficients into a column vector:

$$x = \begin{pmatrix} x_1 \\ x_2 \\ \vdots \\ x_{N^2\times M^2} \end{pmatrix}.$$

This Bloch vector represents the density operator $\hat{\rho}$ in the chosen basis $\mathcal{B}$. Conversely, given the Bloch vector x, we can reconstruct the density operator $\hat{\rho}$ using the inverse mapping.

Lindblad equation in matrix form

Now, we show how to construct a real matrix representation of the Lidnblad equation given by Eq.(2.15). Important premise: in order to better understand which terms of the Hamiltonian $\hat{H}$ contribute through the commutator and through the Lindblad superoperators, we rewrite the equation separating the terms as in the reduced form present in Eq. (2.12).

We can reformulate the Lindblad in Eq.(2.15) as:

$$\dot{\hat{\rho}} = -i\big[\hat{H}_0 + \hat{H}_{int} + \hat{V}(t) + \hat{H}_{hop}, \hat{\rho}\big] + \sum_k \gamma_k \cdot \mathcal{L}[\hat{O}_k](\hat{\rho}).$$

Applying the linearity property of the commutator, i.e., $\Big[\sum_j X_j, Y\Big] = \sum_j \Big[X_j, Y\Big]$, we get

$$\dot{\hat{\rho}} = -i[\hat{H}_0, \hat{\rho}] - i[\hat{H}_{int}, \hat{\rho}] - i[\hat{H}_{hop}, \hat{\rho}] + \sum_k \gamma_k \cdot \mathcal{L}[\hat{O}_k](\hat{\rho}) - i[\hat{V}(t), \hat{\rho}]. \tag{3.8}$$

The terms on the right-hand side represent different contributions to this evolution. Specifically, the terms involving commutators with Hamiltonians describe the coherent evolution of the system, while the term involving $\mathcal{L}[\hat{O}_k]$ describes the incoherent (dissipative) evolution due to the interaction with the environment.

To simplify the notation and emphasize the role of the different Hamiltonians in driving the coherent evolution, we introduce the concept of Liouville superoperators. A Liouville superoperator $\mathcal{L}_{\hat{H}}$ associated with a Hamiltonian $\hat{H}$ is defined as:

$$\mathcal{L}_{\hat{H}}(\cdot) := -i[\hat{H}, \cdot]. \tag{3.9}$$

Using this definition, we can rewrite the coherent terms in Equation (3.8) as:

$$\begin{aligned}
\mathcal{L}_{\hat{H}_0}(\hat{\rho}) &= -i[\hat{H}_0, \hat{\rho}], \\
\mathcal{L}_{\hat{H}_{int}}(\hat{\rho}) &= -i[\hat{H}_{int}, \hat{\rho}], \\
\mathcal{L}_{\hat{H}_{hop}}(\hat{\rho}) &= -i[\hat{H}_{hop}, \hat{\rho}], \\
\mathcal{L}_{\hat{V}(t)}(\hat{\rho}) &= -i[\hat{V}(t), \hat{\rho}].
\end{aligned}$$

These are all examples of Liouville superoperators, each corresponding to a different Hamiltonian: $\hat{H}_0$ (free Hamiltonian), $\hat{H}_{int}$ (interaction Hamiltonian), $\hat{V}(t)$ (the control time-drivingf field) and $\hat{H}_{hop}$, that accounts for the hopping Hamiltonian. The Liouville superoperators describe the unitary evolution of the system induced by these Hamiltonians.

It is crucial to distinguish the Liouville superoperators from the Lindblad superoperators $\mathcal{L}[\hat{O}_k]$. While both are superoperators (i.e., operators acting on operators), they represent fundamentally different types of evolution. The Liouville superoperators describe

coherent, Hamiltonian-driven evolution, whereas the Lindblad superoperators describe incoherent, dissipative evolution due to the system's interaction with its environment. The Lindblad superoperators have a specific form, ensuring that the density operator remains physical. They account for processes such as spontaneous emission, dephasing, and other forms of dissipation. In Equation (3.8), the term $\sum_k \gamma_k \mathcal{L}[\hat{O}_k](\hat{\rho})$ represents the sum of the contributions from different dissipative processes, each characterized by a Lindblad operator $\hat{O}_k$ and a rate γ_k.

Then we can reformulate the equation as

$$\dot{\hat{\rho}} = \mathcal{L}_{\hat{H}_0}(\hat{\rho}) + \mathcal{L}_{\hat{H}_{int}}(\hat{\rho}) + \mathcal{L}_{\hat{H}_{hop}}(\hat{\rho}) + \sum_k \gamma_k \cdot \mathcal{L}[\hat{O}_k](\hat{\rho}) + \mathcal{L}_{\hat{V}(t)}(\hat{\rho}). \tag{3.10}$$

The equation has been reformulated to highlight that the initial two commutators, namely the terms $\mathcal{L}_{\hat{H}_0}(\hat{\rho})$, $\mathcal{L}_{\hat{H}_{int}}(\hat{\rho})$, $\mathcal{L}_{\hat{H}_{hop}}(\hat{\rho})$, together with the superoperator terms $\sum_k \gamma_k \cdot \mathcal{L}[\hat{O}_k](\hat{\rho})$, are solely responsible for the construction of matrix $A \in \mathbb{R}^{N^2 \times M^2}$. Concurrently, the commutator $\mathcal{L}_{\hat{V}(t)}(\hat{\rho})$ is the only term responsible for the construction of the matrix $B \in \mathbb{R}^{N^2 \times M^2}$. This methodology is essential as it facilitates the subsequent transformation of $\eta(t)$ into the scalar control parameter $u(t) \in \mathbb{R}$, enabling the derivation of the linear differential equation system $\dot{x} = Ax + uBx$.

Consider the expression of the density operator $\hat{\rho}$ in terms of the operator basis $\{\hat{B}_i \otimes \tilde{B}_j\}$:

$$\hat{\rho} = \sum_{i=1}^{N^2} \sum_{j=1}^{M^2} x_{(i-1)M^2+j}(t) \left(\hat{B}_i \otimes \tilde{B}_j \right). \tag{3.11}$$

It is crucial to note that the coefficients $x_{(i-1)M^2+j}$ are functions of time, as they describe the temporal evolution of the state of the system. The basis operators $\hat{B}_i$ and $\tilde{B}_j$, on the other hand, are constant in time. To emphasize this time dependence, we have explicitly added the variable t in the coefficients.

Let us compute the time derivative of $\hat{\rho}$ as:

$$\dot{\hat{\rho}} = \frac{d}{dt}\hat{\rho} = \sum_{i=1}^{N^2} \sum_{j=1}^{M^2} \dot{x}_{(i-1)M^2+j}(t) \left(\hat{B}_i \otimes \tilde{B}_j \right).$$

Substituting the expression of $\hat{\rho}$ highlighted in Eq.(3.11) into the reformulated Lindblad equation in (3.10), we get

$$\begin{aligned}\sum_{i,j}\dot{x}_{(i-1)M^2+j}(t)\hat{B}_i\otimes\tilde{B}_j = &\mathcal{L}_{\hat{H}_0}\left(\sum_{i,j}x_{(i-1)M^2+j}(t)\hat{B}_i\otimes\tilde{B}_j\right)\\ &+\mathcal{L}_{\hat{H}_{int}}\left(\sum_{i,j}x_{(i-1)M^2+j}(t)\hat{B}_i\otimes\tilde{B}_j\right)\\ &+\mathcal{L}_{\hat{H}_{hop}}\left(\sum_{i,j}x_{(i-1)M^2+j}(t)\hat{B}_i\otimes\tilde{B}_j\right)\\ &+\sum_k\gamma_k\cdot\mathcal{L}[\hat{O}_k]\left(\sum_{i,j}x_{(i-1)M^2+j}(t)\hat{B}_i\otimes\tilde{B}_j\right)\\ &+\mathcal{L}_{\hat{V}(t)}\left(\sum_{i,j}x_{(i-1)M^2+j}(t)\hat{B}_i\otimes\tilde{B}_j\right).\end{aligned}\tag{3.12}$$

To extract the matrix elements for the real matrix representation, we project both sides of Eq. (3.12) onto an arbitrary element of the Hermitian basis, $\left(\hat{B}_k\otimes\tilde{B}_l\right)$, using the inner product defined as $\langle A|B\rangle = \mathrm{Tr}(A^\dagger B)$. Projecting an operator, such as $\mathcal{L}_{\hat{H}_0}(\hat{\rho})$, onto a basis element $\left(\hat{B}_k\otimes\tilde{B}_l\right)$ via the inner product effectively determines the coefficient of the basis element in the operator's expansion.

This yields

$$\begin{aligned}&\sum_{i,j}\dot{x}_{(i-1)M^2+j}(t)\left\langle\hat{B}_i\otimes\tilde{B}_j\middle|\hat{B}_k\otimes\tilde{B}_l\right\rangle =\\ &\quad\left\langle\mathcal{L}_{\hat{H}_0}\left(\sum_{i,j}x_{(i-1)M^2+j}(t)\hat{B}_i\otimes\tilde{B}_j\right)\middle|\hat{B}_k\otimes\tilde{B}_l\right\rangle\\ &\quad+\left\langle\mathcal{L}_{\hat{H}_{int}}\left(\sum_{i,j}x_{(i-1)M^2+j}(t)\hat{B}_i\otimes\tilde{B}_j\right)\middle|\hat{B}_k\otimes\tilde{B}_l\right\rangle\\ &\quad+\left\langle\mathcal{L}_{\hat{H}_{hop}}\left(\sum_{i,j}x_{(i-1)M^2+j}(t)\hat{B}_i\otimes\tilde{B}_j\right)\middle|\hat{B}_k\otimes\tilde{B}_l\right\rangle\\ &\quad+\sum_k\gamma_k\left\langle\mathcal{L}[\hat{O}_k]\left(\sum_{i,j}x_{(i-1)M^2+j}(t)\hat{B}_i\otimes\tilde{B}_j\right)\middle|\hat{B}_k\otimes\tilde{B}_l\right\rangle\\ &\quad+\left\langle\mathcal{L}_{\hat{V}(t)}\left(\textstyle\sum_{i,j}x_{(i-1)M^2+j}(t)\hat{B}_i\otimes\tilde{B}_j\right)\middle|\hat{B}_k\otimes\tilde{B}_l\right\rangle\end{aligned}\tag{3.13}$$

The contribution of $\mathcal{L}_{\hat{H}_0}$

The contribution of the scalar products $\left\langle \mathcal{L}_{\hat{H}_0}\left(\sum_{i,j} x_{(i-1)M^2+j}(t)\hat{B}_i \otimes \tilde{B}_j\right) \middle| \hat{B}_k \otimes \tilde{B}_l \right\rangle$ generates the matrix $A_{\mathcal{L}_{\hat{H}_0}}$ here raffigurated:

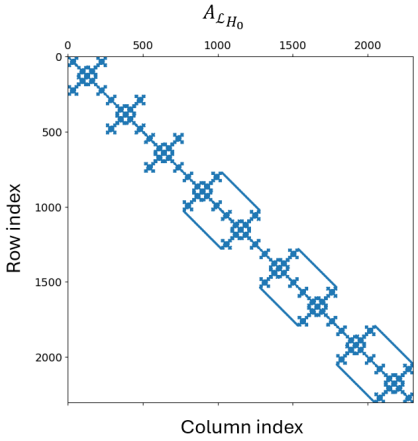

Figure 3.1: Sparsity pattern of $A_{\mathcal{L}_{\hat{H}_0}}$: visualization of the matrix structure related to the free Hamiltonian, $(N_p = 2, M = 3)$.

The contribution of $\mathcal{L}_{\hat{H}_{int}}$

The contribution of the scalar products $\left\langle \mathcal{L}_{\hat{H}_{int}}\left(\sum_{i,j} x_{(i-1)M^2+j}(t)\hat{B}_i \otimes \tilde{B}_j\right) \middle| \hat{B}_k \otimes \tilde{B}_l \right\rangle$ generates the matrix $A_{\mathcal{L}_{\hat{H}_{int}}}$ here raffigurated:

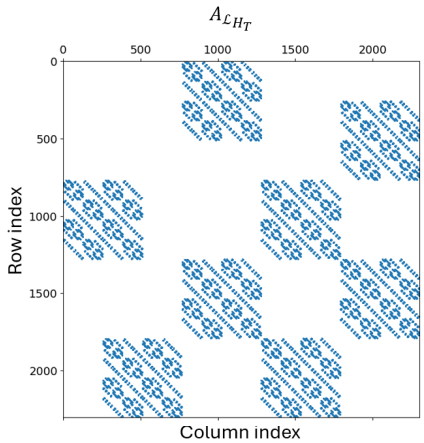

Figure 3.2: Sparsity pattern of $A_{\mathcal{L}_{\hat{H}_{int}}}$: visualization of the structure of the matrix related to the interaction Hamiltonian, $(N_p = 2, M = 3)$.

The contribution of Lindblad superoperators $\mathcal{L}[\hat{O}]$

The contribution of the scalar products $\sum_k \gamma_k \left\langle \mathcal{L}[\hat{O}_k] \left(\sum_{i,j} x_{(i-1)M^2+j}(t) \hat{B}_i \otimes \tilde{B}_j \right) \middle| \hat{B}_k \otimes \tilde{B}_l \right\rangle$ involving Lindblad superoperators generates the matrix $A_{\mathcal{L}[\hat{O}]}$ here raffigurated:

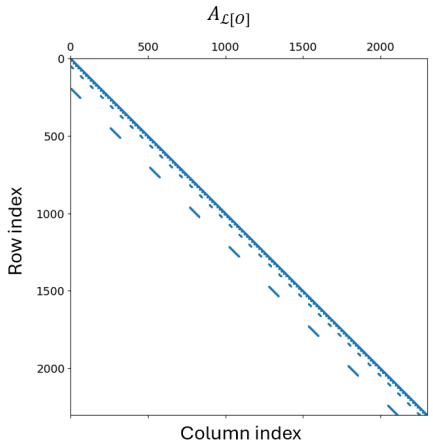

Figure 3.3: Sparsity pattern of $A_{\mathcal{L}[O]}$: visualization of the matrix structure related to Lindblad superoperators, $(N_p = 2, M = 3)$.

The contribution of the hopping term

The contribution of the scalar products $\left\langle \mathcal{L}_{\hat{H}_{hop}} \left(\sum_{i,j} x_{(i-1)M^2+j}(t) \hat{B}_i \otimes \tilde{B}_j \right) \middle| \hat{B}_k \otimes \tilde{B}_l \right\rangle$ generates the matrix $A_{\mathcal{L}_{\hat{H}_{hop}}}$ here raffigurated:

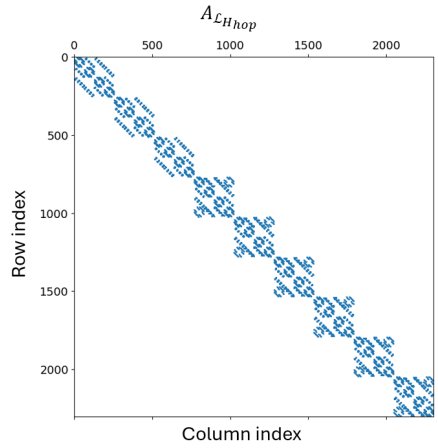

Figure 3.4: Sparsity pattern of $A_{\mathcal{L}_{\hat{H}_{hop}}}$: visualization of the matrix structure related to the hopping Hamiltonian, $(N_p = 2, M = 3)$.

3.1.1. The matrix A

The total matrix A in the the system of linear differential equations is composed of the contributions from the free Hamiltonian, the interaction Hamiltonian, and the Lindblad superoperators:

$$A = A_{\mathcal{L}_{\hat{H}_0}} + A_{\mathcal{L}_{\hat{H}_{int}}} + A_{\mathcal{L}[\hat{O}]} + A_{\mathcal{L}_{\hat{H}_{hop}}} \tag{3.14}$$

where:

- $A_{\mathcal{L}_{\hat{H}_0}}$ represents the contribution from the free Hamiltonian $\hat{H}_0$, as derived in subsection 3.1.
- $A_{\mathcal{L}_{\hat{H}_{int}}}$ represents the contribution from the interaction Hamiltonian $\hat{H}_{int}$, as derived in subsection 3.1.
- $A_{\mathcal{L}[\hat{O}]}$ represents the contribution from the Lindblad superoperators, as derived in subsection 3.1.
- $A_{\mathcal{L}_{\hat{H}_{hop}}}$ represents the contribution from the hopping Hamiltonian, as derived in subsection 3.1.

Each contribution has been obtained by taking the scalar product of the pertinent superoperator, which acts on the system-bath density operator, with a basis element $(\hat{B}_k \otimes \tilde{B}_l)$. Subsequently, the results are reformulated in a matrix-vector representation. The matrix elements pertaining to each contribution are elaborated in their respective sections. The overall matrix A is employed to characterize the temporal evolution of the system's reduced density operator as prescribed by the master equation.

The matrix A, crucial for governing a substantial portion of the system's dynamics, demonstrates a pronounced level of sparsity. This feature arises not by chance but as a direct result of the inherent sparsity present in its constituent matrices $A_{\mathcal{L}_{\hat{H}_0}}$, $A_{\mathcal{L}_{\hat{H}_{int}}}$, $A_{\mathcal{L}[O]}$ and $A_{\mathcal{L}_{\hat{H}_{hop}}}$. As depicted in Figures 3.1, 3.2, 3.3 and 3.4, each of these matrices exhibits a sparse configuration, indicative of the localized interactions and transitions characterizing the system.

The free Hamiltonian component, as referenced by $A_{\mathcal{L}_{\hat{H}_0}}$ and depicted in Figure 3.1, encapsulates the inherent dynamics of the system. The observed sparsity pattern is a direct consequence of the selection rules that dictate transitions between energy levels. In parallel, the interaction Hamiltonian component, denoted by $A_{\mathcal{L}_{\hat{H}_{int}}}$ and illustrated in Figure 3.2, delineates the particular manners in which the system engages with the

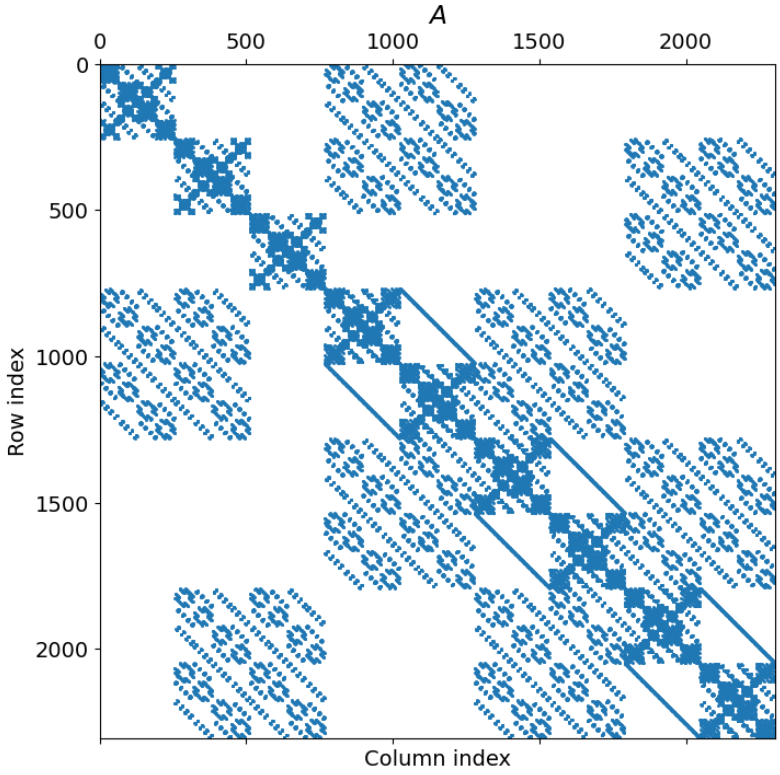

Figure 3.5: Structure of A: the sparsity pattern reveals how the components of the free Hamiltonian, the interaction Hamiltonian and the Lindblad superoperators contribute to the dynamic matrix, $(N_p = 2, M = 3)$.

driving field. The matrix $A_{\mathcal{L}_{\hat{H}_{hop}}}$, indicative of the role of the hopping Hamiltonian within the comprehensive matrix A, similarly manifests a sparse structure, as demonstrated in 3.4. This sparsity emerges due to the intrinsic localized nature of the hopping interaction, wherein each molecule engages solely with its proximate neighbors. Consequently, the matrix elements of $A_{\mathcal{L}_{\hat{H}_{hop}}}$ attain non-zero values exclusively for those basis elements that pertain to transitions between adjacent molecules. This characteristic resultantly engenders a substantial diminution in the quantity of non-zero elements, thereby rendering the matrix sparse. The extent of this sparsity is contingent upon the specific topology of the system (i.e., the connectivity of the molecules); nevertheless, for systems characterized by localized interactions, $A_{\mathcal{L}_{\hat{H}_{hop}}}$ will be a sparse matrix. Lastly, the contribution of the Lindblad superoperators, referenced by $A_{\mathcal{L}[O]}$ and shown in Figure 3.3, which accounts for the coupling of the system with its environment, similarly demonstrates a sparse configuration due to the constrained number of decay channels and transitions considered.

Given that A is composed as the sum of four sparse matrices, it consequently manifests their inherent sparsity. Indeed, the sparsity inherent in each component substantively en-

hances the cumulative sparsity of A. From a computational perspective, this pronounced sparsity is particularly advantageous as it facilitates the efficient storage and manipulation of matrix A, thereby markedly reducing the computational resources necessary for simulating the dynamics of the system. Although the exact percentage of sparsity may fluctuate depending on system parameters such as N_p and M, the fundamental principle persists: the sparse character of the individual contributions culminates in a matrix A of substantial sparsity.

The matrix B

The matrix B originates from the time-dependent driving field operator $\hat{V}(t)$, which is characterized by $\hat{V}(t) = \hat{I}_S \otimes i\eta(t)(\hat{a}^\dagger - \hat{a})$. This operator plays a role in the master equation via the term $\mathcal{L}_{\hat{V}(t)}$, and its influence on the matrix A is delineated by the scalar products $\left\langle \mathcal{L}_{\hat{V}(t)} \left(\sum_{i,j} x_{(i-1)M^2+j}(t) \hat{B}_i \otimes \tilde{B}_j \right) \middle| \hat{B}_k \otimes \tilde{B}_l \right\rangle$.

The matrix is depicted in the following image:

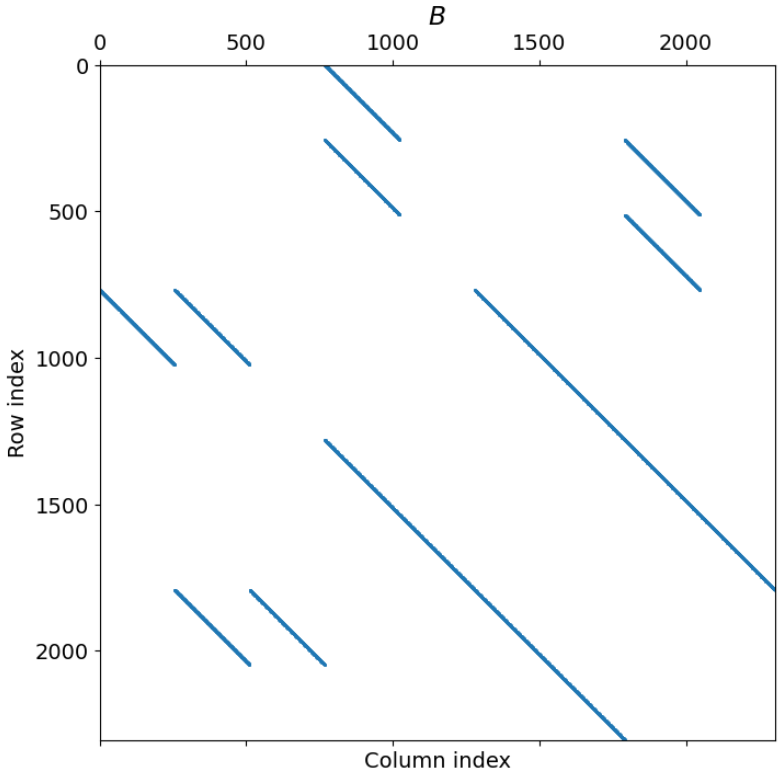

Figure 3.6: Structure of the B matrix: sparsity pattern that highlights coupling with external control, $(N_p = 2, M = 3)$.

The matrix B, which describes the system's interaction with the external control field, exhibits an extremely sparse structure. As shown in Figure 3.6, the vast majority of its

elements are zero. This high degree of sparsity is strikingly evident from the simulation results ($N_p = 2, M = 3$), which revealed a sparsity percentage of approximately 99.92%. This indicates that less than 0.08% of the elements in B are non-zero.

All the above transformation allow us to rewrite the Lindblad equation in the following dynamical system form:

$$\dot{x} = Ax + uBx, \tag{3.15}$$

where

- x constitutes a vector of dimension N^2M^2 that encapsulates the density operator $\hat{\rho}$ in its vectorized form. Each component x_l within x corresponds directly to a particular element of the density matrix, as elaborated in Section 3.1.
- A represents a matrix of dimension $(N^2M^2) \times (N^2M^2)$ that consolidates the effects of the free Hamiltonian ($\mathcal{L}_{\hat{H}_0}$), the interaction Hamiltonian ($\mathcal{L}_{\hat{H}_{int}}$), the hopping Hamiltonian ($\mathcal{L}_{\hat{H}_{hop}}$) and the Lindblad superoperators ($\mathcal{L}[\hat{O}]$). This is elucidated in detail in Section 3.1.1.
- B constitutes a matrix with dimensions $(N^2M^2) \times (N^2M^2)$, representing the impact of the time-dependent driving field operator $\hat{V}(t)$.
- u is a scalar representing the time-dependent control function $u(t)$. Since we have only one control parameter, $\eta(t)$, which is mapped to $u(t)$, u is a scalar. In more intricate scenarios, it is possible to execute quantum optimization control by incorporating the number of controls as indicated in N_C, and treating u as a vector. However, such considerations fall outside the scope of our examination.

The real matrix formulation of the Lindblad equation, as presented in (3.15), constitutes the foundational equation governing our dynamic system. It delineates the temporal progression of the system's density operator, accounting for the effects of both the intrinsic dynamics of the system (as characterized by A) and the external control field (as characterized by B and u). The subsequent phase involves a rigorous analysis of this equation and its utilization in the optimization of the control field $u(t)$ to attain a specified quantum control objective.

3.2. Properties of the matrices A and B and norm preservation

In the context of closed quantum systems, norm preservation of the state vector is a crucial property, ensuring that the system remains in a valid physical state. In [4], the authors demonstrate this property for their specific system, where the matrices A and B are skew-symmetric. Specifically, they prove that if A and B are skew-symmetric, then the dynamical system $\dot{x} = Ax + uBx$ is norm-preserving. This is a direct consequence of the properties of skew-symmetric matrices and their relationship to unitary evolution.

However, the system under consideration in this thesis is an open quantum system, interacting with an environment. This fundamentally changes the dynamics and, crucially, affects norm preservation. While the contributions to the matrix A from the free Hamiltonian ($\mathcal{L}_{\hat{H}_0}$), the interaction Hamiltonian ($\mathcal{L}_{\hat{H}_{int}}$) and from the hopping term ($\mathcal{L}_{\hat{H}_{hop}}$) may still be skew-symmetric, the contribution from the Lindblad superoperators ($\mathcal{L}[\hat{O}]$), denoted as $A_{\mathcal{L}[\hat{O}]}$, is not skew-symmetric. The term associated with the Lindblad superoperators represents the dissipation of energy and information from the system to its surrounding environment, a hallmark of open quantum systems. The non-skew-symmetry inherent in this interaction is intrinsically linked to its dissipative characteristics, resulting in the depletion of energy and information from the system. Furthermore, the terms for the Lindblad superoperators describe the system's interaction with an external environment, and the failure to preserve norms underscores that the system's evolution does not occur in isolation.

In conclusion, the non-skew-symmetrical nature of the Lindblad term plays a significant role in rendering the evolution of open quantum systems more intricate and nuanced in comparison to closed systems.

The presence of the Lindblad term $A_{\mathcal{L}[\hat{O}]}$ in the matrix A implies that the overall matrix A is not skew-symmetric. Consequently, the norm of the state vector x is not preserved in general. This is consistent with the physical picture of an open system, where the interaction with the environment can lead to a decrease in the system's energy and, correspondingly, a change in the norm of the state vector.

To illustrate this mathematically, consider the time derivative of the norm squared of x:

$$\begin{aligned}\frac{d}{dt}||x||^2 &= \frac{d}{dt}(x^\dagger x)\\ &= \dot{x}^\dagger x + x^\dagger \dot{x}\\ &= (Ax + uBx)^\dagger x + x^\dagger(Ax + uBx)\\ &= x^\dagger(A^\dagger + A)x + ux^\dagger(B^\dagger + B)x. \end{aligned} \tag{3.16}$$

To ensure that the norm is preserved, it is crucial that we satisfy condition $\frac{d}{dt}||x||^2 = 0$, which entails that the norm remains invariant over time and is maintained as a constant. The preservation of this property would be ensured if conditions A and B satisfied the skew-hermitian criteria, specifically $A^\dagger = -A$ and $B^\dagger = -B$. Considering both $A, B \in \mathbb{R}^{(N^2M^2)\times(N^2M^2)}$, this condition implies that their symmetries are equivalent to their negations, denoted by $a_{ij} = -a_{ij}, b_{ij} = -b_{ij}$, thus accurately reflecting the skew-symmetry condition, namely $A^T = -A$ and $B^T = -B$.

However, as previously delineated, the incorporation of the Lindblad term $A_{\mathcal{L}[\hat{O}]}$ within A impedes A from attaining a skew-symmetric form. Consequently, the preservation of the norm of x is typically unfeasible.

In conclusion, although norm preservation is a fundamental attribute of closed quantum systems characterized by skew-symmetric Hamiltonians, this property is not maintained in open quantum systems. This discrepancy arises from the intrinsic dissipative interactions with the environment, as represented by the Lindblad superoperators. The matrix A in our analysis of open system dynamics lacks the skew-symmetric characteristic requisite for the preservation of norm.

A key indicator of dissipation within a system is the time variation of the system's "magnitude" or "energy," represented by $||x||^2$. Specifically, the condition

$$\frac{d}{dt}||x||^2 < 0 \tag{3.17}$$

indicates that the energy (or a relevant analogous quantity for the system) is decreasing over time. This is a defining characteristic of dissipative systems, where energy is continuously lost due to interaction with the external environment.

In our quantum battery system, $||x||^2$ represents the norm of the state vector squared, that is related to energy of the system.

The time derivative $\frac{d}{dt}||x||^2$ represents the rate at which this energy or magnitude is changing. The condition $\frac{d}{dt}||x||^2 < 0$ implies that this change is negative, meaning that

the energy is decreasing.

This loss of energy is a clear signature of dissipation. In open quantum systems, dissipation is often modeled through the Lindblad master equation. The Lindblad terms in this equation ensure that the trace of the density operator (which represents total probability) is conserved, but the system's energy can decrease because of interaction with the environment. The condition $\frac{d}{dt}||x||^2 < 0$ can then be used to confirm that the system is indeed losing energy because of this interaction.

By examining the derivative of the squared norm of the state x within Eq. (3.16), and subsequently incorporating the distinct individual contributions of A into the expression, it follows that:

$$\begin{aligned}\frac{d}{dt}||x||^2 &= x^\dagger \left(A^\dagger + A\right) x + u x^\dagger \left(B^\dagger + B\right) x \\ &= x^\dagger \left(A^T_{\mathcal{L}[\hat{O}]} + A_{\mathcal{L}[\hat{O}]}\right) x, \end{aligned} \tag{3.18}$$

where the skew-symmetric property, as delineated in $A_{\mathcal{L}_{\hat{H}_0}}$, $A_{\mathcal{L}_{\hat{H}_{int}}}$, $A_{\mathcal{L}_{\hat{H}_{hop}}}$ and B, has been taken into account. An Hermitian matrix A, with dimension $n \times n$, is deemed negative definite if $x^\dagger A x < 0$ holds for all non-zero elements $x \in \mathbb{R}^n$. Consequently, it is logical to assert that the temporal derivative in Eq. (3.18) would be negative provided that $A^T_{\mathcal{L}[\hat{O}]} + A_{\mathcal{L}[\hat{O}]}$ is negative definite.

As demonstrated in Eq. (3.18), it is the matrix $A_{\mathcal{L}[\hat{O}]}$ that is responsible for processes such as dissipation, which lead to the system losing energy as a result of its interaction with the external environment.

4 | Optimal Control

Optimal control theory is a branch of control theory that concentrates on determining an appropriate control input for a dynamical system over a specified period of time, with the aim of optimizing a predefined objective function. This optimization process may entail either the minimization of a cost function or the maximization of a reward function. Optimal control theory is applicable across a wide range of disciplines, including aerospace engineering (for instance, trajectory optimization for spacecraft), economics (such as the regulation of unemployment through fiscal and monetary policy), and robotics (such as robot path planning). It offers a robust mathematical framework for addressing problems where it is necessary to direct a system towards a desired state or behavior in the most efficient manner possible. The essence of an optimal control problem resides in the formulation of the following elements:

- **Dynamical System:** A mathematical model capturing the temporal evolution of the state of the system. This framework is frequently represented as a set of differential equations, known as the state equations.
- **State Variables:** The parameters that characterize the state of the system at any given moment evolve in accordance with the intrinsic dynamics of the system.
- **Control Inputs:** These variables can be adjusted to affect the behavior of the system. The optimal control problem aims to determine the most effective method of varying these inputs.
- **Objective Function (Cost or Reward Functional):** A mathematical expression that quantifies the performance of a specific control strategy with respect to desired goals and criteria. The objective is to either minimize a cost functional or maximize a reward functional.
- **Constraints:** Constraints on state variables or control inputs. These limitations may represent the physical restrictions inherent in the system (such as maximum force or available fuel) or prescriptive conditions for operation.

The objective of optimal control is to find the control input that optimizes the objective

function while satisfying all constraints. Mathematically, this can be formulated as follows:

Minimize the cost functional

$$J[x(\cdot), u(\cdot), t_0, t_f] = E[x(t_0), t_0, x(t_f), t_f] + \int_{t_0}^{t_f} F[x(t), u(t), t]dt \tag{4.1}$$

subject to the dynamic constraints (state equations)

$$\dot{x}(t) = f[x(t), u(t), t], \tag{4.2}$$

the algebraic path constraints

$$h[x(t), u(t), t] \leq 0, \tag{4.3}$$

and the endpoint conditions

$$e[x(t_0), t_0, x(t_f), t_f] = 0, \tag{4.4}$$

where $x(t)$ is the state, $u(t)$ is the control, t is time, t_0 is the initial time, and t_f is the final time. E is the endpoint cost, and F is the running cost.

In order to solve the optimal control problem in this thesis, we will follow the approach proposed by Pontryagin. The Pontryagin's Maximum Principle provides a necessary condition for optimality. It introduces the concept of a Hamiltonian and derives a set of equations that the optimal control and state must satisfy.

Motivation for Optimal Control of $\eta(t)$ in the Quantum Battery

The external driving field, denoted by the time-dependent term $\hat{V}(t) = \hat{I}_{\text{mol}} \otimes i\eta(t)(\hat{a}^\dagger - \hat{a})$ in (2.9), plays an essential role in modulating the energy dynamics within the quantum battery. This term elucidates the coherent injection of photons into the cavity, thereby directly affecting the photon field while exerting no influence on the molecular system. The real-valued function $\eta(t)$ regulates the magnitude of this driving field, serving as a control parameter that facilitates the modulation of the photon population and phase within the cavity.

The interaction Hamiltonian $\hat{H}_{int}$ enables energy exchange between cavity photons and molecules. By adjusting $\eta(t)$, it is possible to regulate the energy transfer to and from

the molecular system, thereby optimizing the charging and discharging processes of the battery. The complexities inherent in quantum dynamics, combined with the requirement for precise energy management, necessitate the employment of optimal control theory.

Our objective is to determine the optimal temporal configuration of $\eta(t)$ that maximizes energy accumulation during the charging process or minimizes energy dissipation during discharge, within the limits of physical constraints. The application of optimal control constitutes a rigorous mathematical framework to facilitate this endeavor, allowing us to:

- Accurately regulate the photon population and phase within the cavity through $\eta(t)$.
- Enhance the energy transfer between the cavity and the molecules by configuring the driving field.
- Attain optimal charging efficiency and reduce energy dissipation during the discharging process.
- Consider physical limitations and potential noise within the control process.
- Investigate the fundamental performance limits of the battery and devise efficient control strategies.

Subsequent sections will provide a more detailed exploration of these concepts, with a focus on applying them to the specific challenge of optimizing the operation of a quantum battery. The methodology employed in this thesis will be based on the principles outlined by Pontryagin's Maximum Principle.

Problem Formulation for Quantum Battery Charging and Discharging

This section explores the optimal control problem concerning the maximization of the charging process and the minimization of the discharging process in a quantum battery. To enhance the efficiency of the battery's energy storage, the expectation value of the molecular Hamiltonian, including the hopping term, at the terminal time T, that is $\langle\hat{\rho}(T), \left(\hat{H}_{mol} + \hat{H}_{hop}\right) \otimes \hat{I}_{cav}\rangle$, is utilized as the cost functional. This decision is supported by the fact that the scalar product $\langle\hat{\rho}(T), \left(\hat{H}_{mol} + \hat{H}_{hop}\right) \otimes \hat{I}_{cav}\rangle$ precisely encapsulates the mean energy stored in the battery at the final time istant T related to the matter subsystem. This can be understood by recognizing that $\hat{\rho}(T)$ represents the density matrix of the system at time T, encoding the probabilities of the system occupying various energy eigenstates. The Hamiltonian $\left(\hat{H}_{mol} + \hat{H}_{hop}\right) \otimes \hat{I}_{cav}$ describes the total energy of

the molecular subsystem. Consequently, taking the trace of the product of the density matrix and the Hamiltonian effectively averages the energy over all possible states, weighted by their respective probabilities, yielding the expected value of the energy stored in the battery at time T.

Cost Functional and Optimization Problem The objective of the optimal control problem is to find a control input $u(t)$ that steers the quantum battery towards a desired state, either maximizing its energy during charging or minimizing its energy during discharging. To achieve this, we define the following cost functional:

$$J(x,u) := g(x(T)) + \frac{\nu}{2}\|u\|^2_{L^2(0,T)} = \pm c^T x(T) + \frac{\nu}{2}\|u\|^2_{L^2(0,T)} \tag{4.5}$$

where:

- $g\left(x(T)\right) = \pm c^T x(T)$ represents the expectation value of the free energy Hamiltonian at the final time T, i.e., $\langle\hat{\rho}(T)|\hat{H}_0 + \hat{H}_{int}\rangle$. Here, $x(T)$ is a vector representing the state of the system at time T, and c is a vector of coefficients that depends on $\hat{H}_0+\hat{H}_{int}$ and the chosen basis for representing the system's operators. In particular, the $+$ sign is employed in the minimization problem pertaining to the optimization of the discharging process, whereas the $-$ is utilized in the minimization problem related to the optimal charging process.
- $\frac{\nu}{2}\|u\|^2_{L^2(0,T)}$ is a regularization term that penalizes large or rapidly varying control inputs $u(t)$. This term helps to prevent solutions that are not physically realizable or difficult to implement in practice. ν is a positive parameter that tunes the strength of the regularization.

The dynamics of the system are governed by the following equation:

$$\dot{x} = [A + uB]\, x, \quad x(0) = x_0, \tag{4.6}$$

where:

- $x(t)$ is a vector representing the state of the system at time t.
- $u(t)$ is the control input at time t.
- A is a matrix that describes the intrinsic dynamics of the system (without control).
- B is a matrix that couples the control input to the system.

- x_0 is the initial state of the system.

The optimization problem is then formulated as follows:

$$\min_{x,u} J(x,u) := g\left(x(T)\right) + \frac{\nu}{2}\|u\|^2_{L^2(0,T)} = c^T x(T) + \frac{\nu}{2}\|u\|^2_{L^2(0,T)} \tag{4.7}$$

subject to:

$$\begin{aligned} &\dot{x} = [A + uB]x, \quad x(0) = x_0, \\ &t \in (0,T], \quad u \in U_{ad} \subset U = L^2(0,T;\mathbb{R}), \quad x \in X = \left(H^1(0,T)\right)^{N^2 \times M^2} \end{aligned} \tag{4.8}$$

where $A, B \in \mathbb{R}^{(N^2\times M^2)(N^2\times M^2)}$ are given matrices, $U_{ad} := \{u \in L^2(0,T;\mathbb{R}) \,|\, u(0) = 0\}$ represents the set of admissible control inputs, $H^1(0,T)$ is the Sobolev space of functions with weak derivatives in $L^2(0,T)$ and ν is a non-negative parameter.

From Expectation Value to Optimization Problem In order to establish a connection between the expectation value $\langle\hat{\rho}(T), \left(\hat{H}_{mol} + \hat{H}_{hop}\right) \otimes \hat{I}_{cav}\rangle$ and the optimization problem, it is imperative to formulate it in a manner that aligns with the control framework. By referring to the complete basis of the Hermitian matrices $\mathcal{B}$ as presented in Eq. (3.6), we designate the matrices that constitute this basis as $\hat{B}_i$. Consequently, the density operator $\rho(T)$ at final time T can be expressed as a linear combination of these basis matrices:

$$\rho(T) = \sum_{i=1}^{N^2\times M^2} x_i(T)\hat{B}_i$$

where $x_i(T) = \mathrm{Tr}\left(\hat{\rho}(T)\hat{B}_i\right)$ are the expansion coefficients. Similarly, the Hamiltonian $\left(\hat{H}_{mol} + \hat{H}_{hop}\right) \otimes \hat{I}_{cav}$ that describes only the energy related to the matter subsystem, can be written as

$$\left(\hat{H}_{mol} + \hat{H}_{hop}\right) \otimes \hat{I}_{cav} = \sum_{j=1}^{N^2\times M^2} c_j \hat{B}_j \tag{4.9}$$

where c_j are the coefficients of $\left(\hat{H}_{mol} + \hat{H}_{hop}\right) \otimes \hat{I}_{cav}$ in the chosen basis. Then, the expectation value is

$$\begin{aligned}
\langle \hat{\rho}(T), \left(\hat{H}_{mol} + \hat{H}_{hop}\right) \otimes \hat{I}_{cav} \rangle &= \mathrm{Tr}\left(\hat{\rho}(T)\left(\hat{H}_{mol} + \hat{H}_{hop}\right) \otimes \hat{I}_{cav}\right) \\
&= \mathrm{Tr}\left(\sum_{i=1}^{N^2\times M^2} x_i(T)\hat{B}_i \sum_{j=1}^{N^2\times M^2} c_j \hat{B}_j\right) \\
&= \sum_{i=1}^{N^2\times M^2}\sum_{j=1}^{N^2\times M^2} c_j x_i(T)\mathrm{Tr}\left(\hat{B}_i\hat{B}_j\right) \\
&= \sum_{i=1}^{N^2\times M^2}\sum_{j=1}^{N^2\times M^2} c_j x_i(T)\delta_{ij} \\
&= \sum_{i=1}^{N^2\times M^2} c_i x_i(T) \\
&= c^T x(T) = g(x(T)) \qquad (4.10)
\end{aligned}$$

where c is the vector of coefficients c_i, and $x(T)$ is the vector of coefficients $x_i(T)$. This shows how the expectation value $\langle \hat{\rho}(T), \left(\hat{H}_{mol} + \hat{H}_{hop}\right) \otimes \hat{I}_{cav} \rangle$ can be expressed as the term $c^T x(T)$ in the cost functional.

The proposed formulation facilitates the application of optimal control techniques to determine the control input $u(t)$ that minimizes the cost functional, thereby effectively reducing the energy extracted from the battery during discharge or augmenting the energy stored during charging.

4.1. Optimality Conditions

In this section, we delineate the formulation of the optimal control problem pertaining to the quantum battery and examine the requisite conditions for optimality necessary to discern an optimal solution. Consider a general framework of an optimal control problem wherein the objective is to identify a control function $u(t)$ that minimizes the associated cost functional $J(x, u)$, as defined below:

$$J(x, u) = g(x(T)) + \ell(x) + \frac{\nu}{2}\|u\|^2_{L^2(0,T)}. \qquad (4.11)$$

In this context, $x(t)$ denotes the system's state at time t, whereas $u(t)$ signifies the control input. Additionally, $g(x(T))$ corresponds to the cost incurred due to the final state of the battery, while $\ell(x) = \int_0^T \tilde{\ell}(x(t))dt$ pertains to the cost related to the battery's intermediate state. It is relevant to state that, in the quantum battery charging and discharging

optimization problem, no attention is needed to the cost of an intermediate state of the battery. For this reason, in the general cost functional in (4.7), this function $\ell(x)$ does not appear. It has been included in this section for completeness of the discussion and for greater clarity regarding the Pontryagin Maximum Principle of the next section. Furthermore, $\frac{\nu}{2}\|u(t)\|^2_{L^2(0,T)}$ serves as a penalty term imposed on the control. The dynamics of the system are characterized by the differential equation presented below:

$$\dot{x}(t) = f(x(t), u(t)) \quad \text{for} \quad t \in [0, T], \quad x(0) = x_0, \quad u \in U_{ad}. \tag{4.12}$$

In this context, $f(x(t), u(t))$ characterizes the rate of change of the state $x(t)$ as a function that depends on both the state and the control parameters. Specifically, $x(t) \in \mathbb{R}^{N^2 \times M^2}$ denotes the Bloch vector associated with the density matrix $\hat{\rho}$ of the quantum battery. The component $u(t)$ signifies the control mechanism employed for charging or discharging the battery. The temporal progression of the Bloch vector $f(x(t), u(t))$ under the influence of the control u is derived from the Lindblad equation. As mentioned in the previous section, the aim is to determine the optimal control $u^*(t)$ that minimizes the target $J(x, u)$ while adhering to the dynamic constraint $\dot{x} = f(x, u)$.

This general formulation encapsulates a wide range of optimal control problems, including our specific case of quantum battery control. In the following subsections, we will introduce the Hamiltonian formalism and derive the necessary conditions for optimality, leading to the application of Pontryagin's Maximum Principle to our system.

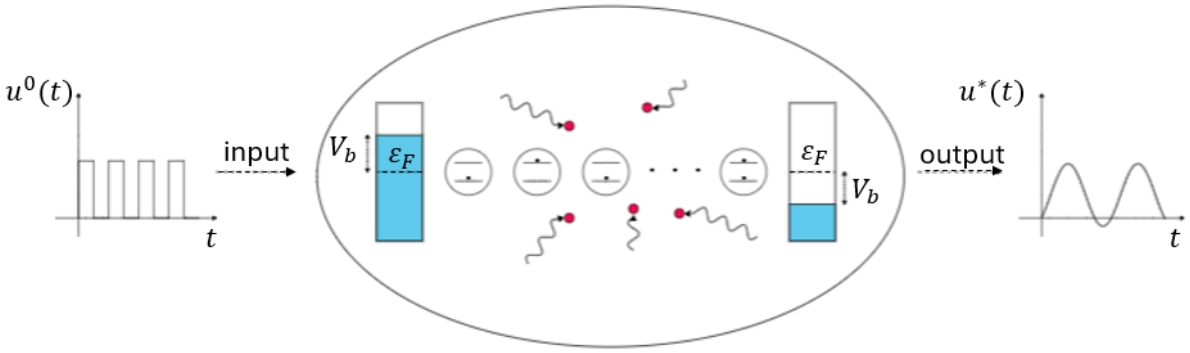

Figure 4.1: The schematic represents a simplified model of a quantum battery and its control process. The goal is to show how an input control signal $u^0(t)$ influences the state of the battery, leading to a desired output signal $u^*(t)$.

Pivotal Role of the Initial State

The initial state x_0 plays a crucial role in defining the objective of the optimal control problem. Its selection depends on whether we aim to maximize the energy stored in the battery (charging process) or minimize the energy extracted from it (discharging process).

Discharge Process For the discharge process, the initial state x_0 is chosen to correspond to the eigenstate of $\hat{H}_0 + \hat{H}_{int}$ that possesses the highest eigenvalue. This represents the state of the battery when it is fully charged. The optimal control objective in this case is to minimize the energy extracted from the battery, driving the system towards a state with lower energy. This translates to minimizing the cost functional $J(x, u)$, which is defined as:

$$\min_{x,u} J(x,u) := c^T x(T) + \frac{\nu}{2}\|u\|^2_{L^2(0,T)} \tag{4.13}$$

subject to:

$$\begin{aligned} &\dot{x} = [A + Bu]x, \quad x(0) = x_0^{\uparrow} \\ &t \in (0,T], \quad u \in U_{ad} \subset U = L^2(0,T;\mathbb{R}), \quad x \in X = \left(H^1(0,T)\right)^{N^2 \times M^2} \end{aligned} \tag{4.14}$$

The specification of the initial state $x(0) = x_0^{\uparrow}$ plays a pivotal role in defining the discharge procedure. To prepare for discharging, the quantum battery is initialized in a state corresponding to its maximal energy configuration. This configuration is achieved by identifying the eigenstate associated with the largest eigenvalue of the composite Hamiltonian $\left(\hat{H}_{mol} + \hat{H}_{hop}\right) \otimes \hat{I}_{cav}$. This particular eigenstate characterizes the maximal energy state of the system, effectively modeling the battery as fully charged. From this fully charged state, our objective is to minimize the residual energy within the system through an optimal control process, thereby achieving the discharging of the quantum battery. The method for determining this initial state begins with the diagonalization of the Hamiltonian $\left(\hat{H}_{mol} + \hat{H}_{hop}\right) \otimes \hat{I}_{cav}$ to derive its eigenvalues and eigenvectors. Among these, the eigenvector aligned with the largest eigenvalue is selected because it embodies the highest-energy state sought. This highest energy state is then conceptualized as a density matrix $\hat{\rho}_0 = |\psi_0\rangle \langle\psi_0|$ where $|\psi_0\rangle$ is the selected eigenvector, and it is accordingly mapped to the suitable vector representation $x_0^{\uparrow}$ within our chosen operator basis via the mapping $V(\hat{\rho})$ (defined in Eq. (3.7)). This mapping produces $x_0^{\uparrow} = V(\hat{\rho}_0)$ and constitutes the initial condition for the optimization problem, ensuring that the discharging process is initiated from the highest energy state of the battery. To further support this framework, it is val-

idated that the norm of $\left(A_{\mathcal{L}_{\hat{H}_{mol}}} + A_{\mathcal{L}_{\hat{H}_{hop}}}\right) x_0^{\uparrow}$ is zero, thus confirming that $x_0^{\uparrow}$ is indeed an eigenvector of $A_{\mathcal{L}_{\hat{H}_{mol}}} + A_{\mathcal{L}_{\hat{H}_{hop}}}$ with an eigenvalue of zero, as would be anticipated for a highest energy (stationary) state.

Charging Process In the context of the charging process, the initial state x_0 is selected to be the eigenstate of $\left(\hat{H}_{mol} + \hat{H}_{hop}\right) \otimes \hat{I}_{cav}$ associated with the lowest eigenvalue. This eigenstate represents the condition of the battery in its ground state, indicating a minimal charge level. The objective of optimal control is to transition the system towards a state of elevated energy, thereby effectively charging the battery. This objective is achieved by minimizing the functional cost $J(x, u)$, which is formally specified as $-c^T x(T) + \frac{\nu}{2}\|u\|^2_{L^2(0,T)}$.

Consequently, the optimization problem associated with the maximization of the charging process is formulated as follows:

$$\min_{x,u} J(x, u) := -c^T x(T) + \frac{\nu}{2}\|u\|^2_{L^2(0,T)} \tag{4.15}$$

subject to:

$$\begin{aligned} &\dot{x} = [A + uB]x, \quad x(0) = x_0^{\downarrow}, \\ &t \in (0, T], \quad u \in U_{ad} \subset U = L^2(0, T; \mathbb{R}), \quad x \in X = \left(H^1(0, T)\right)^{N^2 \times M^2} \end{aligned} \tag{4.16}$$

The initial state, denoted $x_0^{\downarrow}$, is obtained from the eigenvector associated with the smallest eigenvalue of $\hat{H}_0 + \hat{H}_{int}$. This eigenvector, identified as $|\psi_0\rangle$, signifies a ground state of the quantum battery. Subsequently, the associated density matrix, $\hat{\rho}_0 = |\psi_0\rangle \langle\psi_0|$, is transformed into the vector representation x_0 by applying the mapping V, that is, $x_0^{\downarrow} = V(\hat{\rho}_0)$. This procedure guarantees that the charging process begins from the least charged state of the battery.

In summary, the choice of x_0 as the lowest or highest eigenstate of $\left(\hat{H}_{mol} + \hat{H}_{hop}\right) \otimes \hat{I}_{cav}$ allows us to tailor the optimal control problem to the specific task of charging or discharging the quantum battery.

4.2. Pontryagin's Maximum Principle (PMP)

In the previous section, we established the general framework for optimal control problems and their optimality conditions. We now proceed to apply these concepts to our

specific quantum battery system, utilizing Pontryagin's Maximum Principle (PMP). The PMP provides a powerful tool for determining the necessary conditions for optimality in constrained optimal control problems.

Hamiltonian Formulation for the Quantum Battery and Necessary Conditions for Optimality

Having established the general framework for optimal control problems and their optimality conditions, we now proceed to apply these concepts to our specific quantum battery system. To enhance comprehension of Pontryagin's principle, we shall restate the generic optimality problem:

$$\min_{x,u} J(x,u) = g(x(T)) + \ell(x) + \frac{\nu}{2}\|u\|^2_{L^2(0,T)} \tag{4.17}$$

as referred in (4.11) at the beginning of the section 4.1.

The system's dynamics is dictated by the linear differential equation and the accompanying constraints as expressed in:

$$\dot{x}(t) = f(x(t),u(t)) \quad \text{for} \quad t \in [0,T], \quad x(0) = x_0, \quad u(t) \in U_{ad} \tag{4.18}$$

where $x(t)$ represents the state vector, $u(t)$ is the control input, A is the system matrix, B is the control matrix and U_{ad} is the set of admissible control inputs.

In order to employ Pontryagin's Maximum Principle, it is necessary to formulate the Hamiltonian function $\mathcal{H}(x(t),u(t),p(t))$, which integrates the system dynamics with the cost functional. Furthermore, the introduction of the time-dependent co-state vector p is essential, with its components referred to as the costates of the system.

In the context of a general problem characterized by a cost functional akin to Eq. (4.17) and state dynamics as delineated in Eq. (4.18), the Hamiltonian function, universally defined in reference $t \in [0,T]$, is articulated as:

$$\begin{aligned} \mathcal{H} : \mathbb{R}^{N^2\times M^2} \times \mathbb{R} \times \mathbb{R}^{N^2\times M^2} \to \mathbb{R}, \quad \text{s.t.} \\ \mathcal{H}(x(t),u(t),p(t)) := (t), f(x(t),u(t))\rangle + \ell(x(t)) + \frac{\nu}{2}\|u\|^2_{L^2(0,T)} \end{aligned} \tag{4.19}$$

It is important to emphasize that the dimensions of the generic vectors x and p have been configured to correspond with those of the specific optimal control problem pertaining to

the quantum battery being analyzed.

In accordance with [1] we recall the following result:

Theorem 4.1. *(Pontryagin's Maximum Principle). Let* (x^*, u^*) *be a minimizer for* (4.17)-(4.18) *with the set of admissible control inputs defined as* $U_{ad} := \{u \in L^2(0,T;\mathbb{R}) \,|\, u(0) = 0\}$*, and let* p^* *be the solution to*

$$-\dot{p^*} = \mathcal{H}_x(x^*, u^*, p^*), \quad p^*(T) = \big(\nabla_x g(x(T))\big)^T, \quad \forall t \in [0,T] \tag{4.20}$$

it holds that

$$\mathcal{H}(x^*, u^*, p^*) \leq \mathcal{H}(x^*, v, p^*), \quad \forall v \in \mathbb{R}. \tag{4.21}$$

Starting from the generalized formulation provided in (4.19), we establish the Hamiltonian function pertinent to our specific optimization problem as follows:

$$\mathcal{H}\,(x,u,p) := p^T\,[A + uB]\,x + \frac{\nu}{2}\|u\|^2_{L^2(0,T)}. \tag{4.22}$$

As stated in theorem (4.1), we can derive the adjoint equation for the optimal co-state vector p^* as in Eq. (4.20):

$$\begin{aligned} -\dot{p^*} &= \mathcal{H}_x(x^*, u^*, p^*) \\ &= \nabla_x \,, f\,(x,u)\rangle \\ &= \nabla_x \left(f(x^*, u^*)^T p\right) \\ &= \nabla_x \left(x^T [A + u^* B]^T p^*\right) \\ &= (A + u^* B)^T\, p. \end{aligned} \tag{4.23}$$

The final condition for the optimal Lagrange multiplier vector p becomes:

$$\begin{aligned} p^*(T) &= \big(\nabla_x g(x(T))\big)^T \\ &= \big(\nabla_x \left(c^T x(T)\right)\big)^T \\ &= \left(\frac{\partial}{\partial x}\left(c^T x(T)\right)\right)^T \\ &= c. \end{aligned} \tag{4.24}$$

The adjoint equation, as formulated in $\dot{p^*} = -(A + u^* B)^T p$, characterizes the temporal evolution of the co-state vector p^* backward in time. Within the framework of optimal

control, p^* may be interpreted as the sensitivity of the cost functional $J(x, u)$ with respect to variations in the state vector x. Fundamentally, it elucidates the relationship between alterations in the state at a specific point in time and the cumulative cost of the control process.

The final condition $p^*(T) = c$ delineates the value of the co-state vector at the terminal time T. In this context, c denotes the gradient of the terminal cost function $g(x(T))^T$, identified as $\left(\nabla_x g(x(T))\right)^T$. This condition serves to ensure that the co-state vector appropriately reflects the sensitivity of the terminal cost to variations in the final state. Within the framework of our quantum battery system, this implies that $p^*(T)$ encapsulates the manner in which alterations in the final energy state of the battery impact the aggregate cost of the charging or discharging process.

Furthermore, the state equation is given by:

$$\dot{x}^*(t) = \frac{\partial \mathcal{H}}{\partial p}(x^*(t), u^*(t), p^*(t)). \tag{4.25}$$

In the context of our designated Hamiltonian function $\mathcal{H}$ as described in (4.22), it can be expressed as follows:

$$\dot{x}^*(t) = [A + u^*(t)B]\, x^*(t). \tag{4.26}$$

Equation (4.26) delineates the temporal evolution of the optimal state trajectory $x^*(t)$. It indicates that the derivative of the optimal state with respect to time corresponds to the partial derivative of the Hamiltonian with respect to the co-state vector, evaluated under the optimal conditions of state, control, and co-state. This stipulation ensures that the state progresses in alignment with the optimal control and co-state trajectories, as determined by the Hamiltonian.

The optimality conditions, as derived from Pontryagin's Maximum Principle, for the quantum battery system are delineated as follows:

$$\begin{aligned}
\dot{x}^*(t) &= \frac{\partial \mathcal{H}}{\partial p}(x^*(t), u^*(t), p^*(t)) = [A + u^*(t)B]\, x^*(t), \\
\dot{p}^*(t) &= -\mathcal{H}_x(x^*, u^*, p^*) = -\left(A + u^*(t)B\right)^T p^*(t), \\
p^*(T) &= \left(\nabla_x g(x(T))\right)^T = c, \\
\mathcal{H}(x^*, u^*, p^*) &\leq \mathcal{H}(x^*, v, p^*), \quad \forall v \in \mathbb{R}.
\end{aligned} \tag{4.27}$$

These conditions provide a system of equations that must be solved to obtain the optimal

control and state trajectories.

It is pertinent to note that the transition from the optimal condition for the Hamiltonian function $\mathcal{H}$ through Eq. (4.27) facilitates the establishment of the gradient condition of the reduced problem as introduced in Eq. (5.2), which will result in a key point for the implementation of the algorithm used for optimization. In fact, we can show that

$$\nabla_u \mathcal{H}(x, u, p) = \nu u + p^T B x = \nu u + \langle Bx, p \rangle, \tag{4.28}$$

upon examination of the solutions (x^*, p^*) derived from the control u^* within the framework of Theorem 4.1, it is observed that Eq. (4.28) aligns with condition $\nabla_u \hat{J}(u) = 0$. This observation serves to bridge the numerical implementation of the gradient descent algorithm presented in Chapter 5 as informed by the Pontryagin Maximum Principle.

5 | Gradient Descent Method

The gradient descent method is a widely used iterative optimization algorithm with applications spanning various fields, from machine learning to optimal control. Its simplicity and ability to converge to a local minimum make it a valuable tool in situations where the objective function has a complex structure and is highly nonlinear.

5.1. Introduction

Within the domain of quantum control, the gradient descent method provides an effective means for the optimization of control parameters. Its implementation facilitates the iterative exploration of the control space, allowing for the adjustment of parameters in the direction of the steepest descent. This methodology is especially beneficial in the context of our complex quantum battery system, where alternative optimization techniques may prove to be computationally prohibitive or challenging to execute.

The decision to investigate the gradient descent method within the scope of our research was influenced by its relative ease of implementation and robustness, making it an appealing candidate for control optimization within our quantum battery system. Furthermore, its iterative nature facilitates the monitoring of optimization progress and permits dynamic adjustments to the control parameters. This approach aims to achieve a desired final state for the quantum system while minimizing the energy consumed by the control, ultimately maximizing the charge of the quantum battery.

5.2. Application of Gradient descent method to the quantum battery optimization problem

It is important to note that the charge maximization problem in our quantum battery system can be formulated as:

$$\max_{x,u} J(x,u) = c^T x(T) - \frac{\nu}{2}\|u\|^2_{L^2(0,T)}.$$

However, to apply the Gradient Descent method, which is a minimization algorithm, we reformulate the problem as a minimization problem by inverting the sign of the charge term:

$$\min_{x,u} J(x,u) = -c^T x(T) + \frac{\nu}{2}\|u\|^2_{L^2(0,T)}. \tag{5.1}$$

In this formulation, we are minimizing the opposite of the charge, which is equivalent to maximizing the original charge. The regularization term $\frac{\nu}{2}\|u\|^2_{L^2(0,T)}$ remains unchanged, as it penalizes the control energy regardless of the sign of the charge. This reformulation allows us to apply the Gradient Descent method to find the optimal controls that maximize the charge in the quantum battery system.

The charge optimization problem is governed by the constraint equations outlined in Eq. (4.16) related to the optimization problem of the charging process. The state x is unequivocally determined by the initial conditions and the control variables, rendering the mapping $u \mapsto x = x(u)$ well defined for the optimization problem. Moreover, the minimization problem $\min_{x,u} J(x,u)$ can be reformulated into the following equivalent reduced form $\min_u \hat{J}(u) := J(x(u),u)$.

The gradient of this reduced problem can be calculated as

$$\nabla_u \hat{J}(u) = \nu u - \langle Bx, p\rangle, \tag{5.2}$$

where $x = x(u)$ is the unique solution to the state equation (4.16) and p is the unique solution to the adjoint equation which depends on the final state $x(T)$. The choice of x_d is crucial as it influences the computation of the functional cost, ultimately affecting the performance of the optimization algorithm.

5.2.1. The steepest descent algorithm

The Gradient Descent method constitutes an iterative optimization algorithm designed to ascertain the minimum of a function through successive movements in the direction of the negative gradient. The foundation of this algorithm lies in the principle that the negative gradient of a function at a given point signifies the direction of most rapid descent.

The principal procedures of the Gradient Descent algorithm integrated with Armijo Line Search method are enumerated as follows:

Algorithm 5.1 Gradient Descent with Armijo Line Search

Choose initial control u^0, initial state x^0, desired state x_d, step size $\alpha \in \mathbb{R}^+$, tolerance $\eta \in (0,1)$, Armijo parameters $\sigma \in (0,1)$, $\beta \in (0,1)$, minimum step size $\delta \in (0,1)$ and maximum iterations k_{max}.
Set $k \leftarrow 0$, $u \leftarrow u^0$, $x \leftarrow x^0$, $J \leftarrow 0$.
while $\|\nabla_u J(u^k)\|_\infty \geq \eta$ and $k < k_{max}$ **do**
    Compute state x^k by solving the constraint equation (Eq. 5.7) for $u \leftarrow u^k$ and $x \leftarrow x^k$.
    Compute p^k by solving the adjoint equation (Eq. (5.8) -(5.9)), for $x \leftarrow x^k$ and $u \leftarrow u^k$.
    Compute cost $J(u^k)$ with x^k, u^k, x_d, ν.
    Compute cost gradient $\nabla_u J(u^k)$.
    Set step size $s \leftarrow \alpha$.
    while $J(u^{k+1}) > J(u^k) - \sigma s \|\nabla_u J(u^k)\|_2^2$ **do**
        Compute new control $u^{k+1} \leftarrow u^k - s\nabla_u J(u^k)$.
        Compute new state x^{k+1} by solving the constraint equation (Eq. 5.7) for $u \leftarrow u^{k+1}$ and $x \leftarrow x^k$.
        Compute new cost $J(u^{k+1})$ with $x \leftarrow x^{k+1}, u \leftarrow u^{k+1}, \nu$.
        Set $s \leftarrow \beta s$.
        if $s < \delta$ **then**
            Break inner loop.
        end if
    end while
    Set $k \leftarrow k + 1$.
end while
return u^k, x^k

The choice of the step size α_k is crucial for the convergence of the algorithm. A too large step size may cause the algorithm to overshoot the minimum, while a too small step size may lead to slow convergence. In our implementation, we used the Armijo line search to determine the step size. The Armijo line search is a backtracking line search method that guarantees sufficient decrease of the objective function at each iteration.

The convergence characteristics of the Gradient Descent method are contingent upon various parameters, such as the selection of step size and the initial estimation. The determination of an appropriate stopping criterion holds significant importance. Typical stopping criteria encompass the establishment of a maximum iteration count, a tolerance

level for the gradient norm, or a tolerance for variations in the objective function. As delineated in the algorithmic steps, a tolerance-based stopping criterion predicated on the gradient norm and a predefined iteration ceiling was employed. More precisely, the algorithm concludes when the gradient norm descends below a specified threshold, η, or when the iteration count attains the maximum allowable limit. This selection underscores our focus on guaranteeing that the optimization procedure converges toward a state where the gradient is adequately minimized, suggesting an approach to a local minimum.

Numerical Methodology and Implementation

The numerical implementation of the Gradient Descent algorithm involves several key steps, including the initialization of parameters, the iterative update of the control, and the numerical solution of the state and adjoint equations. In the following, we will detail the procedure for our implementation.

Initial Parameters

- $\alpha > 0$ **(Initial Step Size)**: determines the initial step size for the Armijo line search. This parameter influences the convergence speed and the stability of the algorithm.
- $\eta > 0$ **(Convergence Tolerance)**: defines the tolerance for the norm of the gradient. The algorithm stops when the norm of the gradient is less than η.
- $\sigma \in (0, 1)$ **(Armijo Parameter)**: controls the sufficient decrease condition in the Armijo line search.
- $\beta \in (0, 1)$ **(Backtracking Factor)**: used to reduce the step size in the Armijo line search when the sufficient decrease condition is not satisfied.
- $\delta > 0$ **(Minimum Step Size)**: defines the minimum step size allowed in the Armijo line search.

Initial Control $u^0(t)$ We explored various signal types for the initial control $u^0(t)$ to assess their impact on the convergence and performance of the Gradient Descent algorithm. This approach allows us to experimentally determine the most effective initial control for our quantum battery charging process. The initial controls considered include step functions and constant signals.

Control Update

The core iterative loop of the Gradient Descent algorithm focuses on updating the control u to minimize the cost function J.

1. **Gradient Calculation:** At each iteration k, the gradient of the cost function J with respect to the control u is computed using the formula:

$$\nabla_u \hat{J}(u) = \nu u - \langle Bx, p \rangle,$$

where x is the solution of the state equation and p is the solution of the adjoint equation. The cost functional gradient was calculated using a discretized version of the analytical formula described in Eq. (5.2). In particular, the discrete gradient g^j was computed as follows:

$$\begin{aligned} g^j &= -\frac{1}{4}\left\langle B\left(x^{j+1}+x^j\right), p^{j+1}\right\rangle - \frac{1}{4}\left\langle B\left(x^j+x^{j-1}\right), p^j\right\rangle, \quad \text{for} \quad j=2,\ldots,N_t-1 \\ g^{N_t} &= -\frac{1}{4}\left\langle B\left(x^{N_t}+x^{N_t 1}\right), p^{N_t}\right\rangle = 0. \end{aligned} \tag{5.3}$$

This approach ensures that the computed gradient is exact at the discrete level, avoiding approximations introduced by methods such as finite differences.

The final discretized gradient used in the Gradient Descent algorithm was obtained by adding the regularization term νu to the discrete gradient g, namely

$$\nabla_u J(u^k) = \nu u^k + g^k \tag{5.4}$$

for the k-th iteration of the algorithm.

2. **Armijo Line Search:** The step size s is determined using the Armijo line search, which ensures sufficient decrease of the cost function:

$$J(u^{k+1}) \leq J(u^k) - \sigma s \|\nabla_u J(u^k)\|_2^2, \tag{5.5}$$

where $u^{k+1} = u^k - s\nabla_u J(u^k)$.

3. **Control Update:** The control is updated using the formula

$$u^{k+1} = u^k - s\nabla_u J(u^k). \tag{5.6}$$

This loop is repeated until the norm of the gradient is less than the tolerance η.

Solving State and Adjoint Equations

The state and adjoint equations are ordinary differential equations (ODEs) that describe the temporal evolution of the system's state and adjoint state. We use a modified Crank-Nicolson method to numerically integrate these equations.

Modified Crank-Nicolson Method The state and adjoint equations are discretized using the modified Crank-Nicolson method as follows:

1. **State equation:**

$$x^{j+1} = x^j + \frac{h}{4}\left[\left(A + Bu^{j+1}\right) + \left(A + Bu^j\right)\right]\left(x^{j+1} + x^j\right)$$
$$\text{for} \quad j = 1, \ldots, N_t \quad \text{and with} \quad x^1 = x(0). \tag{5.7}$$

2. **Adjoint equation:**

$$p^j = p^{j+1} + \frac{h}{4}\left[\left(A + Bu^j\right) + \left(A + Bu^{j-1}\right)\right]^* p^j$$
$$+ \frac{h}{4}\left[\left(A + Bu^{j+1}\right) + \left(A + Bu^j\right)\right]^* p^{j+1} \quad \text{for} \quad j = N_t - 1, \ldots, 2, \tag{5.8}$$

with the final condition

$$h\Big(\frac{1}{h}I - \frac{1}{4}\Big[(A + Bu^{N_t}) + (A + Bu^{N_t-1})\Big]^*\Big)p^{N_t} = -c. \tag{5.9}$$

6 | Numerical Experiments and Discussion

In this chapter, we present the numerical results obtained from the quantum control optimization. The main objective is to determine optimal controls that allow for specific state transitions within the system. We also analyze the connectivity of the adjacency graph of matrices A and B, which describe the interactions in the system, to better understand the structure and properties of the system itself. To gain a deeper understanding of the quantum battery intrinsic behavior, we analyze its free dynamics in the absence of external control. This investigation explores how the battery state evolves when the time-driving field $\hat{V}(t)$, responsible for manipulating the photon population within the cavity and influencing energy transfer with the molecules, is absent. By examining this scenario, we can discern the natural tendencies of the system and establish a baseline for comparison when control mechanisms are introduced. This analysis offers key insights into the quantum battery energy storage and dissipation traits, supporting the development of efficient control strategies to enhance performance.

6.1. Graph Connectivity Analysis

Examining the connectivity of the adjacency graph derived from matrices A and B is crucial for comprehending the structure of the quantum battery system. These matrices encapsulate the interactions among the various degrees of freedom present in the system. The adjacency graph constructed from these matrices illustrates the connections between the distinct states within the system.

The adjacency graph presented in Fig. 6.1 illustrates the connectivity between states in the quantum battery system. Each node in the graph represents a distinct state, and an edge connecting two nodes indicates a significant interaction between the corresponding states. These interactions are determined by the absolute values of the elements in the matrix $IAI + IBI$, with edges being established when these values exceed a threshold of 10^{-8}.

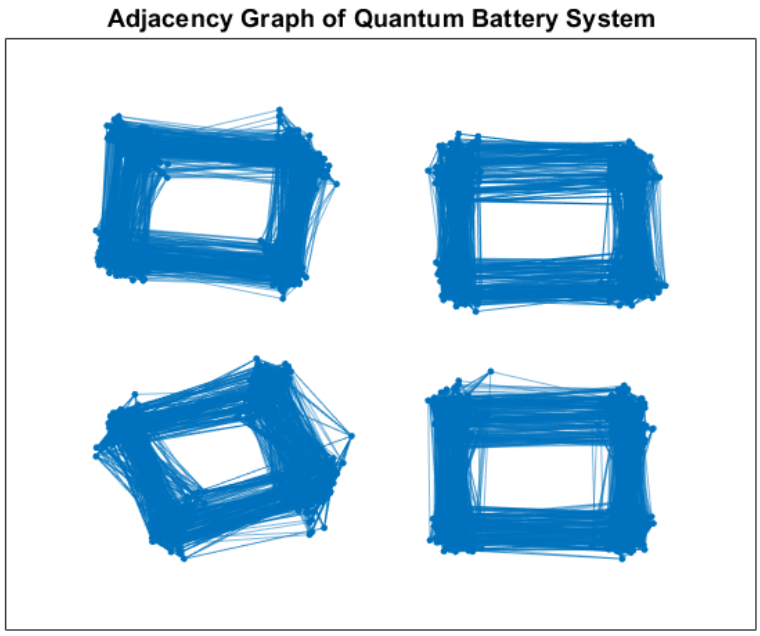

Figure 6.1: Adjacency graph representing the connectivity between states in the quantum battery system. Nodes represent states and edges indicate interactions exceeding a threshold of 10^{-8}.

The graph structure is dense and complex. The four blocks that can be seen suggest that there are substructures with very high connectivity within these blocks. Furthermore, the graph reveals the structure of the system's state space, highlighting which states are strongly coupled and which are relatively isolated. The distribution and density of edges provide insights into the flow of energy and information within the system. For instance, clusters of highly connected nodes indicate groups of states that readily interact with each other, potentially facilitating efficient energy transfer.

By analyzing the four connected components of the graph, we can identify subsets of states that are strongly interconnected. This information is crucial for understanding the system's dynamics and for designing effective control strategies. The graph also allows us to visualize the pathways for state transitions, which is essential for optimizing the charging and discharging processes of the quantum battery.

Fig.6.2 shows the structure of the $A+B$ matrices before the connectivity analysis. Fig.6.3 shows the structure of the matrices reordered according to the identified connected blocks. The analysis revealed the presence of four connected blocks, with the first main block containing most of the states. Crucially, the components within each block are intercon-

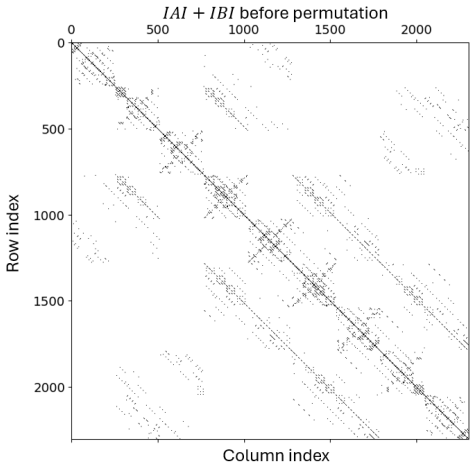

Figure 6.2: $A+B$ showed before the permutation.

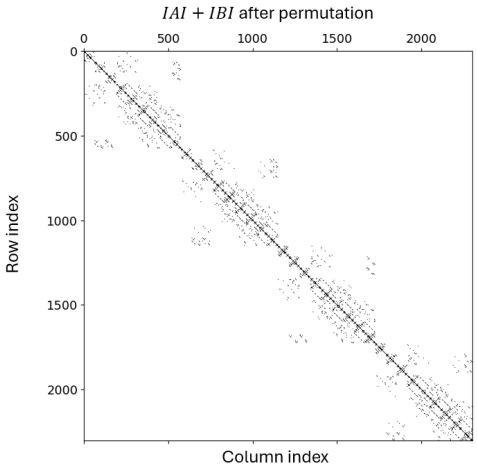

Figure 6.3: $A + B$ showed after the permutation.

nected, while there are no connections between the four blocks themselves. This isolation means that these blocks do not interact with each other, either through direct interactions or through the control mechanism.

Moreover, the ground state x_0 is fully contained within the first block. This indicates that the system dynamics, under the influence of the applied control, will remain restricted to this block, as no mechanism exists for the system to transition to any of the other three blocks.

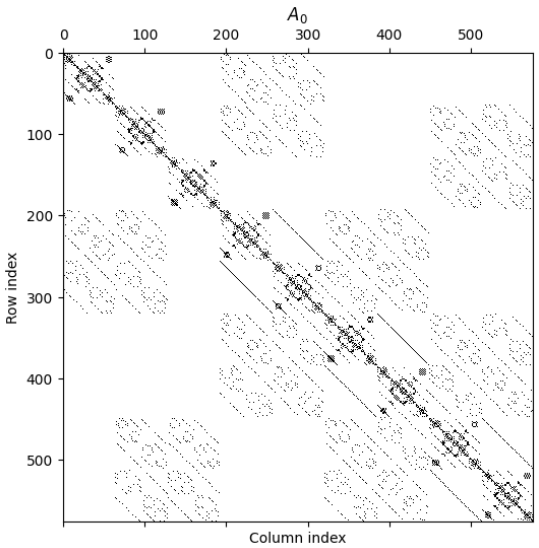

Figure 6.4: Submatrix of A for the primary connected block.

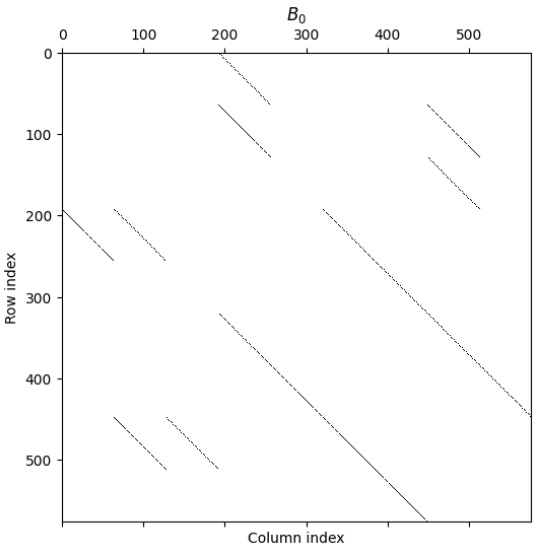

Figure 6.5: Submatrix of B for the primary connected block.

To further illustrate the structure of the primary connected block, we present in Fig. 6.4-

6.5 the submatrices of A and B corresponding to this block. These submatrices clearly show the internal connectivity within the block, highlighting the strong interactions among its constituent states.

The decision to concentrate on the principal connected block is driven by the advantage that implementing control optimization on a reduced block notably decreases computational time. Moreover, the principal block encompasses the most significant interactions in the system, which are assumed to be paramount for the system's dynamics. Consequently, conducting the analysis on a smaller block facilitates an easier interpretation of the results.

6.2. Spectral Properties of Matrix A

In this section, we focus on the analysis of the spectral properties of matrix A, which plays a fundamental role in the dynamics of our quantum battery system. The eigenvalues of A provide crucial information about the natural oscillation frequencies of the system, its stability, and energy levels. Understanding the spectrum of A is essential for interpreting the results of numerical simulations and for evaluating the effectiveness of the optimized control.

Matrix A describes the interactions between the different degrees of freedom. By calculating the eigenvalues of A, we can obtain a detailed view of the oscillation modes and evolution times of the system in the absence of external control. This analysis will allow us to establish a baseline for comparing the free evolution of the system with that obtained through the application of the optimized control, as will be discussed in the following sections.

The analysis of the spectrum of matrix A reveals important characteristics of the dynamics of our quantum system. Fig. 6.6 shows the distribution of the eigenvalues of A in the Gauss plane.

Upon examination of the graph, a number of remarkable observations are apparent. Primarily, the eigenvalues exhibit symmetry with respect to the real axis, a common property of Hermitian matrices. In addition, multiple distinct clusters of eigenvalues are evident, arranged in vertical bands, implying the existence of well-defined oscillation modes within the system. The real component of the eigenvalues appears quantized, adopting discrete values, potentially signifying quantization of the energy levels. Conversely, the imaginary component spans a broader range, yet maintains an identifiable structure, indicative of various oscillation frequencies. The symmetry concerning the real axis signifies that each

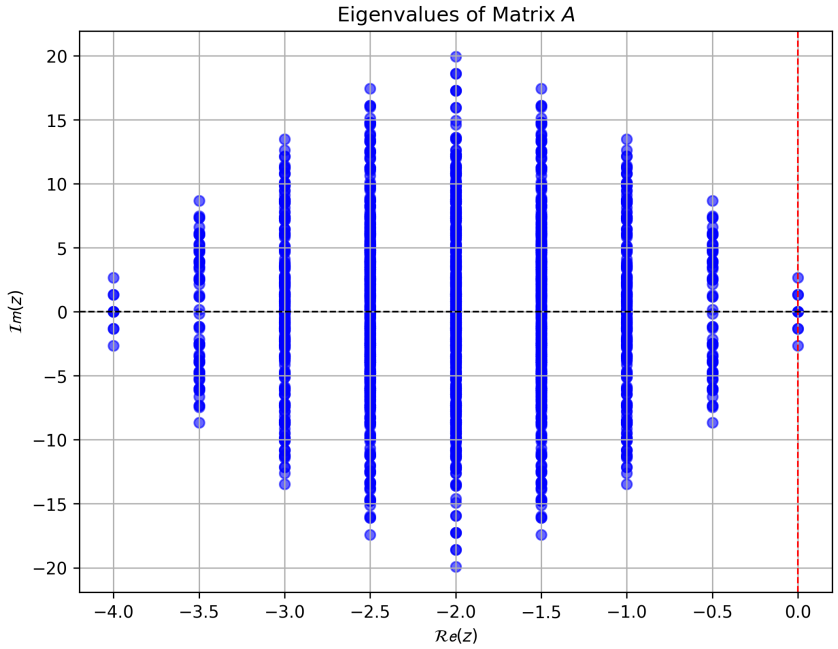

Figure 6.6: Spectrum of matrix A.

eigenvalue with a positive imaginary component has a corresponding eigenvalue with a negative imaginary component, a symmetry linked to the nature of the system's interactions. Additionally, the observation of eigenvalues with both zero real and imaginary components suggests the existence of stationary states or modes characterized by slow evolution within the system. A zero eigenvalue signifies the presence of one or more stationary states, which are states in which the system remains temporally invariant, unless it is subject to external perturbations. Within the framework of quantum mechanics, these states may denote equilibrium configurations.

6.3. Free Evolution of the System

To fully understand the effectiveness of the optimized control we have developed, it is essential to analyze the behavior of our quantum battery system in the absence of external control. This section is dedicated to examining the free evolution of the system, providing a crucial baseline for evaluating the impact of control.

To study the dissipation effects and the evolution toward a ground state, we set initial conditions to reflect a ground state of the system that was slightly perturbed. We then monitored the temporal evolution of the states, obtaining the vector $x(t)$.

The simulation results show that the vector $y(t) = Ax(t)$ exhibits interesting behavior.

Some components of $y(t)$ stabilize rapidly, reaching a constant zero value over time. Other components, however, show persistent oscillatory behavior.

In particular, we observe that the components of $y(t)$ that stabilize are associated with the kernel of A discussed in the previous section. These indicate the presence of stationary states or slow evolution modes in the system. The components of $y(t)$ that oscillate, on the other hand, are associated with the eigenvalues with zero real part but nonzero imaginary parts. These oscillating components tend to behave like sinusoidal functions, corresponding to the eigenvectors of A associated with the imaginary eigenvalues. These imaginary eigenvalues directly relate to the natural oscillation frequencies of the system.

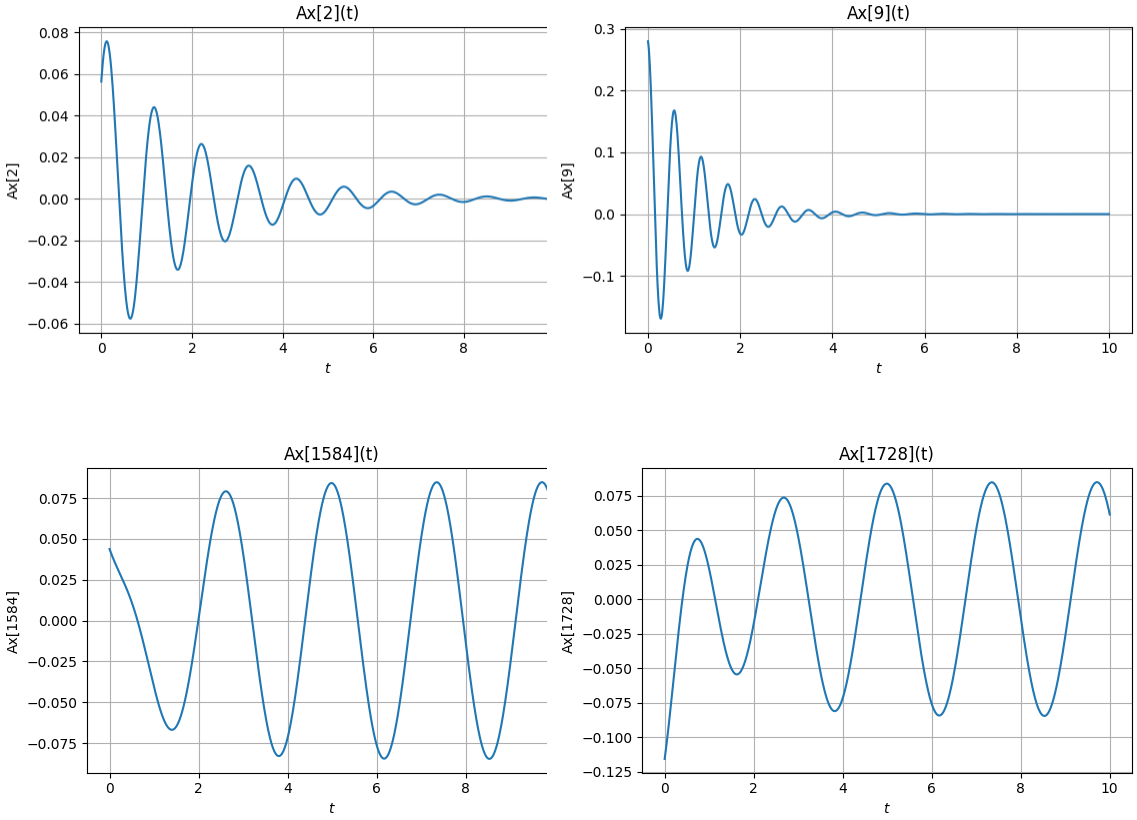

Figure 6.7: Some examples of components of $y(t)$ during free evolution. In top-left, top-middle and top-right we can see the evolutions of the components $y_2(t) = Ax_2(t)$ and $y_9(t) = Ax_9(t)$ which stabilize over time. Instead, in bottom-left, bottom-middle and bottom-right there are the evolutions of $y_{1584}(t) = Ax_{1584}(t)$ and $y_{1728}(t) = Ax_{1728}(t)$ which are oscillating over time.

System's Dynamics The analysis of the eigenvalues of matrix A provides valuable insights into the system dynamics. A key aspect of the system dynamics can be observed:

starting from an arbitrary initial state x_0, the system naturally evolves towards the lowest-energy eigenstates of the Hamiltonian. These eigenstates correspond to the eigenvectors of matrix A with null or purely imaginary eigenvalues. This observation is consistent with our simulation results, where the stabilizing components of $y(t)$ are associated with real, negative eigenvalues (representing energy dissipation), while the oscillating components are associated with imaginary eigenvalues (representing persistent oscillations at specific frequencies).

Our findings confirm this behavior. The components of $y(t)$ that stabilize are associated with the purely real and negative eigenvalues of A, indicating a dissipation of energy as the system converges towards these lower energy states. On the other hand, the oscillating components of $y(t)$ are associated with the eigenvalues with non-zero imaginary parts, reflecting the natural oscillation frequencies around these lower energy states. These oscillations persist because there is no dissipation associated with purely imaginary eigenvalues.

Therefore, the spectrum of A reveals a rich interplay between decaying and oscillatory modes in the free evolution of the system. This analysis provides a crucial baseline for understanding how the optimized control can manipulate these modes to achieve specific state transitions, as we will explore in the following sections.

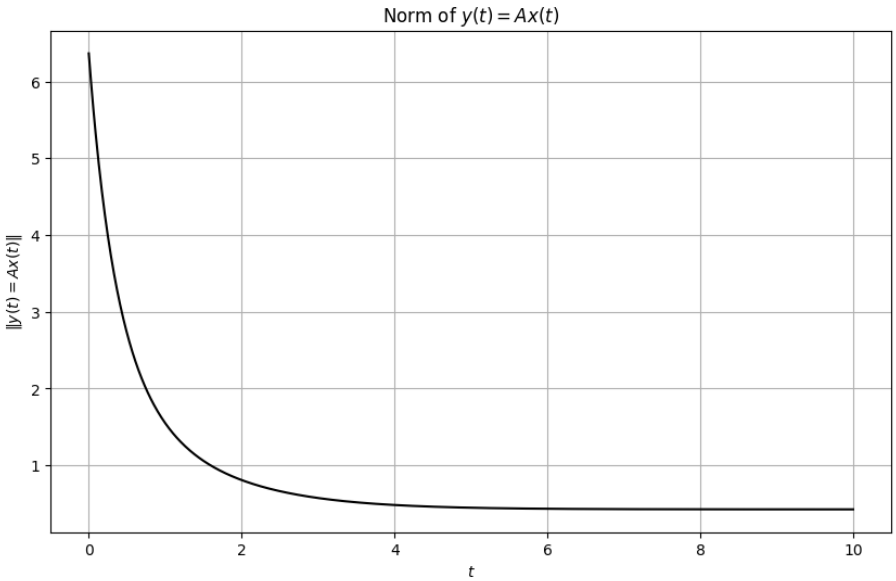

Figure 6.8: Norm $\|y(t)\|$ evolution over time.

Figures 6.8-6.9 illustrate the behavior of the norm of $y(t) = Ax(t)$ and its time derivative during the system free evolution. The left subplot (Figure 6.8) shows the norm of $y(t)$ rapidly decreasing and then stabilizing, indicating the tendency of the system towards

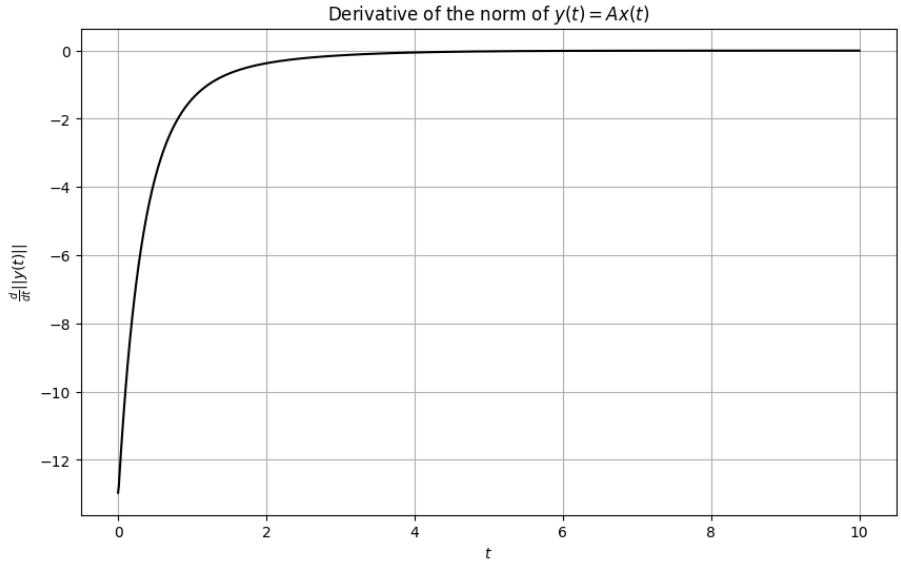

Figure 6.9: Norm derivative $\frac{d}{dt}\|y(t)\|$ over time.

a steady state. The right subplot (Figure 6.9) displays the time derivative of the norm, which is initially negative and then approaches zero, confirming the stabilization trend. This consistent behavior in both the norm and its derivative reinforces the observation of decaying modes within the system, as previously discussed in relation to the real, negative eigenvalues of matrix A.

6.4. Optimization Results Analysis

In this section, we present and analyze the numerical results obtained from the optimization of the control for the quantum battery system. Building upon the spectral analysis of matrix A and the free evolution of the system discussed in the previous sections, we now delve into the dynamic behavior of the system with the presence of functions control. To enable a more accurate analysis of the fundamental behavior of the system, we considered the smallest possible system dimensions, namely $N_p = 2$ and $M = 3$.

We present the results of the optimization process, focusing on the convergence of the algorithm and the characteristics of the optimal control. Finally, we investigate the possible energetic transitions that we can achieve with the charging process, shedding light on the effectiveness and limitations of our optimization approach.

6.4.1. Methodology and Optimization Parameters

As previously stated, the Gradient Descent algorithm with Armijo Line Search, described in Chapter 5 has been employed for optimizing the control of the quantum battery with regard to the charging process. In this specific section, we will explain which quantities will characterize the numerical simulations and their physical meaning.

The cost functional J In our specific application to quantum battery charging, we aim to minimize the following cost functional:

$$J(x, u) = -x_d^T x(T) + \frac{\nu}{2}\|u\|^2_{L^2(0,T)}, \tag{6.1}$$

where $x(T)$ is the final state of the system at time T, x_d is the desired final state, ν is the regularization parameter, u is the control signal parameter.

By setting the regularization parameter ν to a sufficiently small magnitude, the significance of term $\frac{\nu}{2}||u||^2_{L^2}$ becomes negligible in comparison to the scalar product $-x_d^T x(T)$. Consequently, the cost functional is predominantly influenced by this scalar product between the desired state and the final state. Hence, the minimization of $J(x, u)$ is analogous to the maximization of $x_d^T x(T)$, which quantifies the overlap between the final state and the desired state.

Achieving convergence in this optimization process translates to successfully steering the quantum battery from its initial state, x_0, to the desired final state, x_d, through the application of the control signal u. This transition, $x_0 \to x_d$, signifies a successful charging

process, where the battery reaches its target energy level.

Energy E In order to evaluate the efficacy of the charging process, the energy E of the battery in its terminal state will be calculated. This energy measurement will furnish a quantitative assessment of the stored energy within the battery and will serve as a metric for assessing the performance of the Gradient Descent approach in enhancing the charging procedure.

The energy of the quantum system at the final time T is calculated as the expectation value of the Hamiltonian $\hat{H} = \hat{H}_0 + \hat{H}_{int} + \hat{H}_{hop} \otimes \hat{I}_{cav}$ in the final state $x(T)$. Mathematically, this is expressed as:

$$E(T) = \langle \hat{H} \rangle = \mathrm{Tr}\left(\hat{H}\hat{\rho}(T)\right), \tag{6.2}$$

where $\hat{\rho}(T)$ represents the final density operator of the quantum battery system.

In our numerical context, the energy E is calculated through the scalar product:

$$E(T) = c^T x(T), \tag{6.3}$$

where c is a vector of coefficients derived from the Hamiltonian $\hat{H}$. Specifically, c is defined as the vector of coefficients of the basis matrix with respect to the Hamiltonian $\hat{H}$ as reported in Eq. (4.10).

This expression highlights that the energy E is directly influenced by both the Hamiltonian $\hat{H}$ (through the vector c) and the final state $x(T)$. In other words, the value of E depends on the specific configuration of the quantum system and the state reached at the end of the optimization process.

The Role of the Desired State x_d The desired state x_d plays a crucial role in the optimization problem of quantum battery charging. It represents the ideal configuration of the system at the final time T, corresponding to the desired energy level or maximum achievable charge. The choice of x_d determines the specific objective of the optimization: maximizing the overlap $x_d^T x(T)$ means that we are trying to bring the system as close as possible to this ideal configuration. In physical terms, x_d embodies the state in which the battery has stored the maximum useful energy, making it an essential benchmark for evaluating the effectiveness of the charging process. Therefore, a precise definition of x_d is fundamental to guide the optimization algorithm towards the desired solution, ensuring that the quantum battery reaches its optimal performance.

Construction of the Vectors x_0 and x_d The vectors x_0 and x_d are constructed from the eigenvalues and eigenstates of the static Hamiltonian of the quantum battery, $H_0 + H_{int} + \hat{H}_{hop}$. In particular, the minimum eigenvalue λ_0 corresponds to the ground state $|\psi_0\rangle$, while the subsequent eigenvalues λ_d correspond to the excited states $|\psi_d\rangle$.

To construct the vector x_0, we compute the density operator $\hat{\rho}_0$ as the outer product of the ground state:

$$\hat{\rho}_0 = |\psi_0\rangle \langle\psi_0| .$$

Next, we apply the linear map V (defined in Equation (3.7)) to the density operator $\hat{\rho}_0$ to obtain the real vector x_0:

$$x_0 = V(\hat{\rho}_0).$$

The aforementioned procedure is employed to construct the requisite vectors x_d. For each excited state $|\psi_d\rangle$, the relative density operator is calculated as $\hat{\rho}_d = |\psi_d\rangle \langle\psi_d|$, and subsequently, by applying the linear map V, the desired vector $x_d = V(\hat{\rho}_d)$ is obtained.

In this way, the vectors x_0 and x_d represent the ground state and excited states of the quantum battery, respectively, and are used as inputs for the Gradient Descent optimization algorithm.

State Transitions Simulations for charge optimization, initiated with specified initial x_0 and targeted x_d states and employing the Gradient Descent algorithm, yield empirical substantiation of the capability to excite the quantum battery, effectuating a transition from x_0 to x_d. The attainment of convergence towards an optimal value of the cost functional $J(x, u)$ in these simulations underscores the algorithm's efficacy in discerning a control signal u that can effectively transition the system from its initial to the desired final state. From a physical standpoint, this denotes the feasibility of transferring energy to the quantum battery in a controlled manner, elevating it from a lower energy level (denoted by x_0) to a higher energy level (denoted by x_d). Consequently, these simulations not only illustrate the efficacy of the Gradient Descent algorithm but also validate the practicability of modulating the quantum battery's state for energy storage.

The algorithm has been implemented in MATLAB. The optimization parameters were set as follows: maximum number of iterations and gradient convergence tolerance were chosen variably depending on the specific state transition considered. The regularization parameter was set to $\nu = 10^{-8}$. For each result, the specific values of the maximum number of iterations and gradient convergence tolerance used will be reported. The initial states x_0 were chosen to represent different battery charge levels, while the desired states x_d

were selected to explore the maximum possible charge and specific state transitions.

The final energy $E(T)$ was calculated as the expectation value of the final Hamiltonian, using the equation (6.3). The cost functional J was calculated using the equation (6.1).

6.4.2. System Analysis Without Hopping and Dissipation ($t_h = 0$, $\Gamma = 0$)

The convergence analysis of the Gradient Descent algorithm is crucial for evaluating its effectiveness in optimizing the quantum battery charging process. In this section, we will focus on how the cost functional $\hat{J}(u)$ and the gradient norm $\|\nabla_u \hat{J}(u)\|$ vary throughout the iterations. This analysis will provide insights into the algorithm's performance, highlighting both successful convergence scenarios and instances where convergence was not achieved.

Connections and Optimization

In this subsection, we investigate the behavior of the quantum battery system under idealized conditions, specifically without intermolecular hopping ($t_h = 0$) and in the absence of dissipation ($\Gamma = 0$). This setup effectively simulates a closed quantum system, allowing us to focus on the intrinsic dynamics driven by the interaction between the molecular and photonic components.

To visualize the connectivity between the eigenstates of the Hamiltonian of the system, we present the network topology derived from the matrix $A + B$, where A represents the dynamics of the system evaluated without the hopping term $A_{\mathcal{L}_{\hat{H}_{hop}}}$ and without the dissipative superoperators $A_{\mathcal{L}[O_k \otimes I_{cav}]}$. These visualizations provide a clear understanding of the possible transitions between eigenstates and the structure of the Hilbert space of the system.

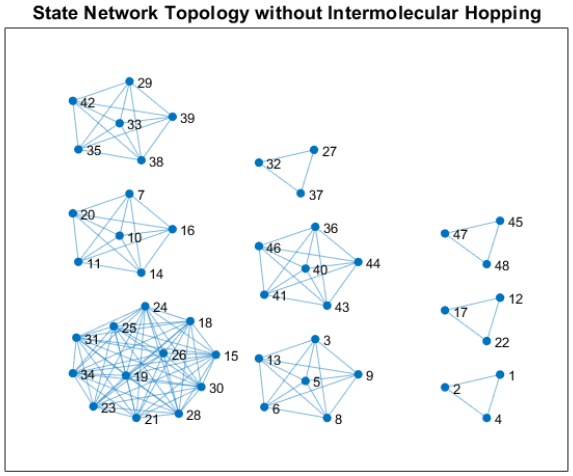

Figure 6.10: Network topology of the system without hopping and dissipation.

In the analysis of the connectivity graphs representing the eigenstates of the Hamiltonian $\hat{H}_0 + \hat{H}_{int}$, we observed the presence of triangular structures formed by three eigenstates each. These triangles (1-2-4, 27-32-37, 12-17-22, 47-48-45) indicate transitions occurring exclusively between photonic states, effectively bypassing any interaction with the molecular subsystem. This phenomenon arises from the fact that these specific eigenstates reside within the kernel of the interaction Hamiltonian $\hat{H}_{int}$.

To verify this, consider an eigenstate $|\psi_1\rangle$ belonging to the triangle 1-2-4. If this state indeed lies within the kernel of $\hat{H}_{int}$, then the following condition must be satisfied:

$$\hat{H}_{int}|\psi_1\rangle = 0. \tag{6.4}$$

This implies that the molecular component of these eigenstates belongs to the kernel of the molecular part of $\hat{H}_{int}$, resulting in a scenario where the molecules do not interact with the photons. Consequently, the control field $\eta(t)$, which introduces photons into the quantum battery to optimize the charging process, in these specific transitions, solely excites the photonic cavity.

Conversely, transitions involving eigenstates outside these triangular structures, such as those within the graph 3-5-6-8-9-13, exhibit an effective charging of the molecular component alongside the photonic component. This distinction highlights the selective nature of the control process, where the ability to excite molecular states depends on the specific eigenstates involved in the transition.

The emergence of these pure photonic transition triangles is attributed to the finite dimensionality of the photon space, constrained to $M = 3$ maximum Fock states. This limitation delineates the possible transitions within the system, leading to the observed triangular patterns.

Upon further investigation, we have verified that these eigenstates indeed satisfy the kernel condition, thus confirming the presence of pure photonic transitions and their specific impact on the charging dynamics of the quantum battery.

Since we are trying to maximize the energy stored in the matter part of the battery, which can be calculated as $\langle \hat{\rho}(T), (\hat{H}_{\text{mol}} + \hat{H}_{\text{hop}}) \otimes \hat{I}_{\text{cav}} \rangle = \text{Tr}\left[\hat{\rho}(T)(\hat{H}_{\text{mol}} + \hat{H}_{\text{hop}}) \otimes \hat{I}_{\text{cav}}\right]$, we will not consider transitions between pure photonic states. The exclusion of photons from the energy calculation is due to the empirical observation that photons leave the battery or cavity at an expedited rate, thereby rendering only the matter excitations as viable constituents of stored energy within the battery.

The subsequent analysis will focus exclusively on state transitions that involve the matter part of the battery, highlighting the convergence properties of the Gradient Descent algorithm and the characteristics of the resulting optimal control.

Successful Transitions To provide a comprehensive overview of the algorithm's performance, we present two tables summarizing the results of various transitions. The first table includes transitions involving both the photonic and matter subsystems, as well as transitions occurring solely within the photonic subsystem. This allows us to assess the algorithm's convergence capabilities under different conditions. The second table focuses specifically on transitions that involve the matter part of the battery, starting from the ground state $x_0 = 3$. This table is particularly relevant for evaluating the effectiveness of the control in charging the matter component of the battery.

These tables will highlight the main features of each transition, providing detailed information about the initial (x_0) and final (x_d) states, the energy (E) at final time istant T, the value of the cost functional ($\hat{J}(u)$), the number of iterations needed for convergence and the norm of the final gradient ($\|\nabla_u \hat{J}(u)\|$). It is important to note that the subscripts of the various vectors signify the corresponding eigenstate of the Hamiltonian $\hat{H} = (\hat{H}_{\text{mol}} + \hat{H}_{\text{hop}}) \otimes \hat{I}_{\text{cav}}$, with these values ranging from 1 to $N \times M$. According to this chosen notation, the vector characterizing the ground state of our quantum battery system is denoted by x_1.

Successful Transitions

$x_0 \to x_d$	Iterations	$E(T)$ [eV]	$\hat{J}(u)$	$\|\nabla_u \hat{J}(u)\|_\infty$
$x_1 \to x_2$	80	-1.331×10^0	-9.999×10^{-1}	8.724×10^{-5}
$x_1 \to x_4$	80	-2.661×10^0	-9.999×10^{-1}	2.725×10^{-5}
$x_2 \to x_4$	21	-2.661×10^0	-9.999×10^{-1}	5.541×10^{-6}
$x_{12} \to x_{17}$	78	-7.791×10^0	-9.999×10^{-1}	8.495×10^{-6}
$x_{12} \to x_{22}$	80	-9.122×10^0	-9.999×10^{-1}	2.725×10^{-5}
$x_{17} \to x_{22}$	21	-9.125×10^0	-9.999×10^{-1}	5.541×10^{-6}

Table 6.1: Results for selected transitions with $\Gamma = 0$ and $t_h = 0$, effectively simulating a closed quantum system without hopping. For these specific transitions, the maximum number of iterations has been set set to 80 and the tolerance on the convergence of the cost functional gradient to $1,0 \times 10^{-6}$.

Successful Transitions for $x_0 = 3$

$x_0 \to x_d$	Iterations	$E(T)$ [eV]	$\hat{J}(u)$	$\|\nabla_u \hat{J}(u)\|_\infty$
$x_3 \to x_5$	2000	-2.793×10^0	-9.278×10^{-1}	6.297×10^{-3}
$x_3 \to x_8$	2000	-2.850×10^0	-9.592×10^{-1}	4.548×10^{-3}
$x_3 \to x_9$	2000	-3.255×10^0	-9.111×10^{-1}	3.513×10^{-3}

Table 6.2: Results for selected transitions with $\Gamma = 0$ and $t_h = 0$, effectively simulating a closed quantum system without hopping. This table is specifically focusing on transitions involving the matter part of the battery, starting from the ground state $x_0 = 3$. We considered for these transitions a maximum number of iterations parameter equal to 2000 and the tolerance on the convergence of the cost functional gradient equal to $1,0 \times 10^{-4}$.

Convergence Analysis of Optimal Transition $x_0 = 3 \to x_d = 8$ To further illustrate the performance and convergence properties of the Gradient Descent algorithm, we now present detailed convergence graphs for the specific transition $x_0 = 3 \to x_d = 8$. This particular transition was selected for its high optimization efficacy, as evidenced by its cost functional value $\hat{J}(u) = -0.9592$, which is among the closest to the ideal value of -1 in Table 6.1.

The transition involves the matter part of the battery, which is central to our objective of

maximizing energy storage. As regards the optimal performance, the value of $\hat{J}(u)$ close to -1 indicates a highly effective optimization, making the convergence graphs particularly representative of the algorithm's best performance. Focusing on a single, well-optimized transition simplifies the presentation and facilitates a clear understanding of the algorithm's behavior.

The following graphs will depict the convergence of energy $E(T)$ over iterations, the convergence of the cost functional $\hat{J}(u)$ over iterations, the evolution of the gradient norm $\|\nabla_u \hat{J}(u)\|$ over iterations and the profile of the optimal control $u^*(t)$.

These visualizations will provide a comprehensive insight into the dynamics of the optimization process and the characteristics of the optimal control solution for this representative transition.

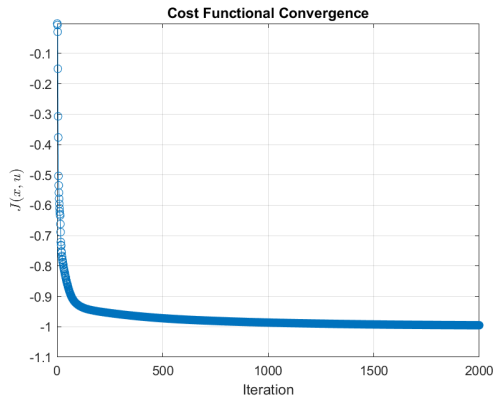

Figure 6.11: Evolution of $\hat{J}(u)$ over iterations for transition $x_3 \to x_8$.

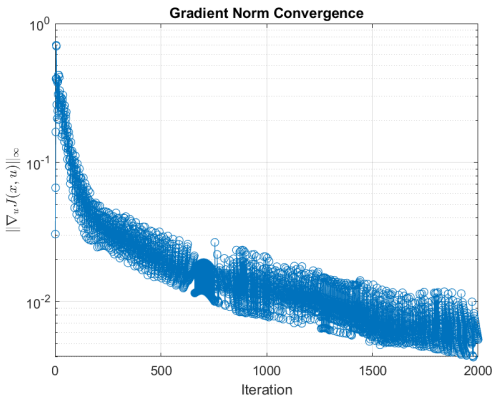

Figure 6.12: Evolution of $\|\nabla_u \hat{J}(u)\|_\infty$ over iterations for transition $x_3 \to x_8$.

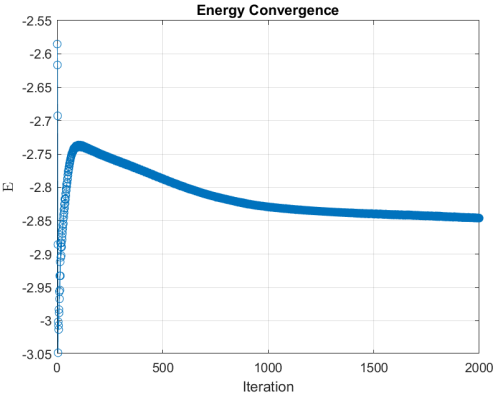

Figure 6.13: Evolution of energy $E(T)$ over iterations for transition $x_3 \to x_8$.

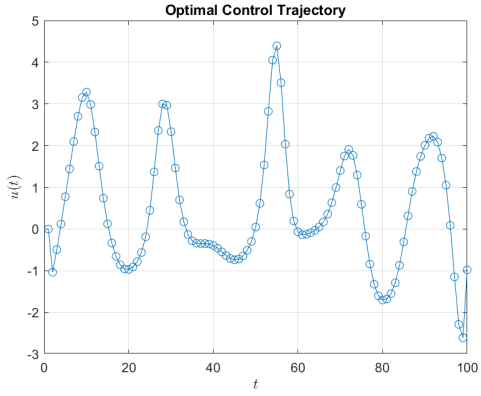

Figure 6.14: Optimal control $u^*(t)$ for transition $x_3 \to x_8$.

Physical Significance of the Results

The convergence of the cost functional $\hat{J}(u)$ to the value of -1 illustrated in Fig.6.11 takes on a very precise physical meaning in the context of quantum battery charging optimization. Recall that the cost functional defined in Eq. (6.1) is calculated via $x(T)$ which represents the final state of the system at time T and x_d which is the desired state, we can note an important result in terms of optimization and optimal control.

The scalar product $x_d^T x(T)$ quantifies the overlap between the final state reached $x(T)$ and the desired state x_d. In the ideal case in which the optimization algorithm manages to bring the system exactly to the desired state, we have $x(T) = x_d$. In this situation, the scalar product $x_d^T x(T)$ reaches its maximum value, which in our case is 1, since the states are normalized.

Therefore, when $J(x, u)$ converges to -1, this means that $-x_d^T x(T) = -1$ and therefore $x_d^T x(T) = 1$. This result indicates that the algorithm has optimized the control u in such a way as to bring the system exactly to the desired state x_d, maximizing the overlap between the final state and the desired state. In other words, convergence to the negative value of -1 indicates a perfect charge of the quantum battery, where the stored energy reaches its maximum possible value.

The convergence of the energy $E(T)$ to a constant value indicates that the quantum battery system has reached a stable state. This stable state represents the final energy level that the system can achieve under the given control conditions and initial state. The convergence of $E(T)$ also suggests that the gradient descent algorithm has successfully minimized the cost functional $\hat{J}(u)$, which is a measure of the difference between the final state $x(T)$ and the desired state x_d. When $\hat{J}(u)$ is minimized, it means that the system has been driven as close as possible to the desired state, maximizing the overlap between the two states. The specific value of the converged energy $E(T)$ depends on the initial state, the desired state, and the dynamics of the system. In general, a higher value of $E(T)$ indicates a higher level of energy stored in the battery.

The optimal control trajectory $u^*(t)$ depicted in Figure 6.14 reveals a complex and dynamically varying profile. In our quantum battery system, $u(t)$ corresponds to $\eta(t)$, which physically represents the amplitude of the external driving field used to inject photons into the cavity. This field directly influences the interaction between the molecular components and the photonic mode, thereby controlling the energy transfer and charging process.

The control signal exhibits significant oscillations, indicating that the photon injection rate

must be rapidly modulated to achieve optimal charging. This suggests that a constant driving field is suboptimal and that precise temporal control is necessary to navigate the quantum dynamics effectively. The amplitude of the oscillations varies over time, implying that the intensity of the driving field needs to be dynamically adjusted. This variation reflects the changing energy landscape of the system as it evolves from the initial state $x_0 = 3$ to the desired final state $x_d = 8$. Furthermore, the absence of a clear periodic pattern in the control signal underscores the necessity for photon injection into the quantum battery to deviate from a periodic regime and instead adhere to a precise temporal trend. Rapid fluctuations in $\eta(t)$ suggest that the optimal charging process involves precise and frequent adjustments to the photon injection rate. These adjustments are likely crucial for coherently manipulating the quantum states and maximizing energy transfer to the molecular components of the battery.

The characteristics observed in $u^*(t)$ highlight the precise control needed for efficiently charging the quantum battery using dynamic, non-periodic, and rapidly fluctuating driving fields. This strategy navigates the complex energy landscape, ensuring efficient energy transfer and maximal energy storage in the battery.

6.4.3. Optimal Control Robustness Analysis

In the previous sections, we have demonstrated the effectiveness of the Gradient Descent algorithm in optimizing the charging process of a quantum battery system under idealized conditions, specifically in the absence of intermolecular hopping ($t_h = 0$) and dissipation ($\Gamma = 0$). However, for practical applications, it is crucial to assess the robustness of these optimal control strategies when subjected to perturbations and non-ideal conditions.

This subsection is dedicated to evaluating the sensitivity of the pre-computed optimal controls $u^*(t)$ to variations in key system parameters, namely the amplitude probability referred to intermolecular hopping (t_h) and the charge hopping rate between the quantum battery and the leads (Γ). To do this, we will use the pre-computed optimal controls $u^*(t)$ as initial guess $u^0(t)$ for new simulations that include these perturbations into the system dynamics. This analysis aims to understand how the perturbations affect the performance of the optimal controls and the overall charging efficiency of the quantum battery.

Specifically, we will analyze the variation of the cost functional $\hat{J}(u^*)$ as a function of both t_h and Γ. This analysis will provide insights into the resilience of the optimal controls and their ability to maintain near-optimal performance in the presence of realistic system imperfections.

The following sections will detail the specific methodologies and results obtained from

this robustness analysis, focusing first on the effects of intermolecular hopping and subsequently on the impact of dissipation set by the Γ rate.

Robustness of Optimal Control Against Intermolecular Hopping (t_h)

In this subsection, we investigate the robustness of the optimal control strategies derived for the quantum battery system in the absence of intermolecular hopping ($t_h = 0$) and dissipation ($\Gamma = 0$). Specifically, we aim to evaluate how the performance of the precomputed optimal controls $u^*(t)$ is affected when the hopping term, characterized by the parameter t_h, is introduced into the system's dynamics.

We will focus on analyzing the variation of the cost functional $\hat{J}(u^*)$ as a function of t_h. This analysis will provide insights into the sensitivity of the optimal control to perturbations induced by intermolecular hopping. By utilizing the optimal controls $u^*(t)$ obtained for the transitions $3 \to 5$, $3 \to 8$, and $3 \to 9$ as input parameters for the system dynamics with varying t_h, we will observe how the cost functional $\hat{J}(u^*)$ deviates from its optimal value.

The expected outcome is a set of graphs depicting $\hat{J}(u^*)$ as a function of t_h for each of the selected transitions. These graphs will illustrate the range of values t_h for which optimal control remains effective, as well as the point at which the hopping term significantly degrades the performance of the system. Based on considerations regarding the overlap of molecular orbitals and the energy scales involved, we anticipate t_h to be within the meV range or a fraction thereof. Furthermore, we will discuss the implications of these findings for the practical implementation of quantum battery charging protocols in real-world scenarios, where intermolecular interactions, although present, must be accurately characterized to guarantee optimal performance.

As shown in Figure 6.15, the cost functional $\hat{J}(u^*)$ remains relatively close to its optimal value for a wide range of t_h values, particularly in the lower range from 10^{-4} eV to approximately $7,5 \times 10^{-2}$ eV. This confirms our expectation that the optimal control strategies are robust against small perturbations in the intermolecular hopping strength, as anticipated based on considerations regarding the overlap of molecular orbitals and the energy scales involved. Specifically, these values fall within the meV range or a fraction thereof, as previously discussed.

However, as t_h increases beyond 10^{-2} eV, we observe a significant degradation in the performance of the control, with $\hat{J}(u^*)$ deviating substantially from its optimal value. This suggests that the control becomes increasingly sensitive to the hopping term when

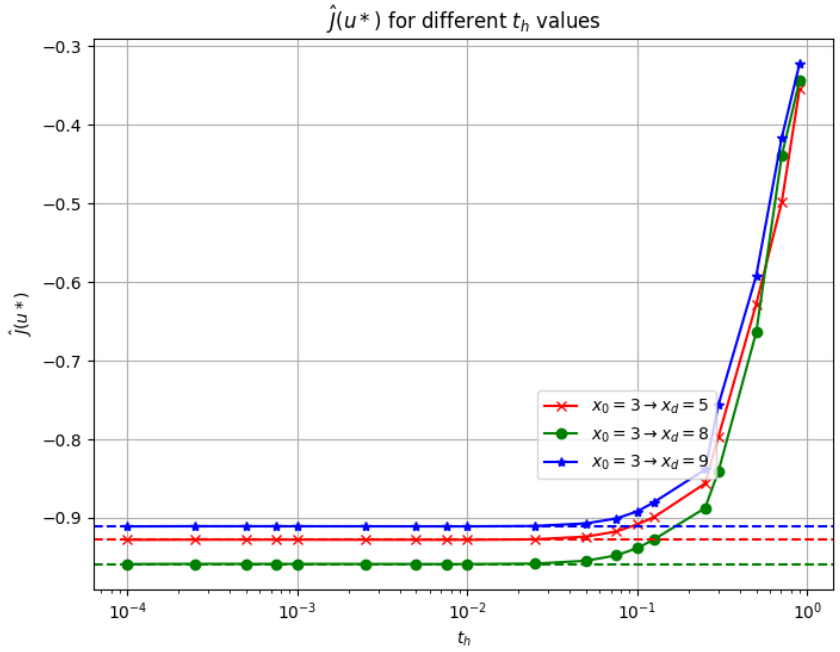

Figure 6.15: Variation of the cost functional $\hat{J}(u^*)$ as a function of the hopping probability amplitude t_h (eV) for the transitions $x_0 = 3 \rightarrow x_d = 5$, $x_0 = 3 \rightarrow x_d = 8$ and $x_0 = 3 \rightarrow x_d = 9$.

t_h exceeds this threshold.

These results highlight the importance of accurately characterizing the intermolecular hopping strength in practical implementations of quantum battery charging protocols. Although optimal control strategies are robust against small variations in t_h, larger deviations can significantly impact charging efficiency. Therefore, careful consideration must be given to the specific parameters of the system and operating conditions to ensure effective control.

Robustness of Optimal Control Against Dissipation (Γ)

In this subsection, we investigate the robustness of the optimal control strategies with respect to dissipation, characterized by the parameter Γ. Our aim is to evaluate how the performance of the pre-computed optimal controls $u^*(t)$ is affected when dissipation is introduced into the system's dynamics.

The charge hopping rate between the quantum battery and the leads is modeled through the Lindblad superoperator. This operator accounts for the loss of coherence and energy as a result of interactions with the environment, which in this case are the leads. By varying Γ, we effectively modulate the strength of this coupling and, consequently, the

charge hopping rate. As discussed in Section 2.3.2, the typical range for Γ in numerous physical systems is $10^8 - 10^{10}\text{s}^{-1}$. In this study, we will consider a broader range of values, with $\Gamma = 1$ corresponding to 10^{12}s^{-1}, to investigate the robustness of the optimal control under different charge hopping regimes. We will focus on analyzing the variation of the cost functional $\hat{J}(u^*)$ as a function of Γ. This analysis will provide insights into the sensitivity of the optimal control to dissipative effects and the influence of charge hopping on the overall charging process.

We will utilize the optimal controls $u^*(t)$ obtained for the same transitions analyzed in the previous subsection, namely $3 \to 5$, $3 \to 8$, and $3 \to 9$. By applying these controls to the system dynamics with varying Γ, we will observe how the cost functional $\hat{J}(u^*)$ deviates from its optimal value.

The expected outcome is a set of graphs depicting $\hat{J}(u^*)$ as a function of Γ for each of the selected transitions. These graphs will illustrate the range of Γ values for which the optimal control remains effective, as well as the point at which dissipation significantly degrades the performance of the system. Furthermore, we will discuss the implications of these findings for the practical implementation of quantum battery charging protocols in realistic environments, where dissipation is unavoidable.

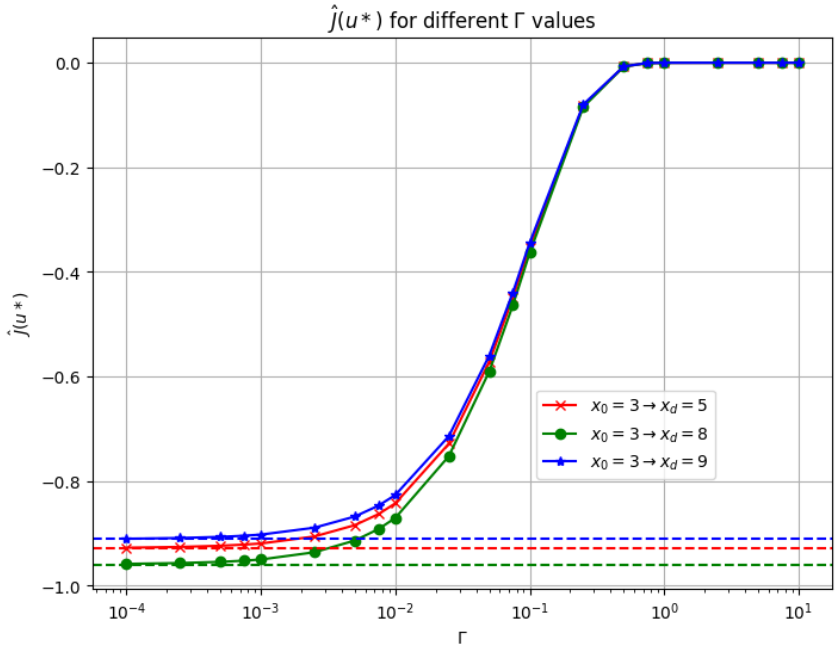

Figure 6.16: Variation of the cost functional $\hat{J}(u^*)$ as a function of the charge hopping rate Γ (s^{-1}) for the transitions $x_0 = 3 \to x_d = 5$, $x_0 = 3 \to x_d = 8$ and $x_0 = 3 \to x_d = 9$.

As shown in Figure 6.16, the cost functional $\hat{J}(u^*)$ remains close to its optimal value for

a wide range of Γ values, specifically up to approximately $\Gamma = 10^{-2}$. This indicates that the optimal control strategies are robust against small to moderate levels of dissipation.

However, as Γ increases beyond 10^{-2}, we observe a significant degradation in control performance, with $\hat{J}(u^*)$ rapidly approaching zero. This suggests that the control becomes highly sensitive to dissipation when Γ exceeds this threshold and leads to a null overlap between the desired state x_d and the ground state x_0.

As previously reiterated, in our simulation, $\Gamma = 1$ corresponds to $10^{12}s^{-1}$. Therefore, the robust region observed in the graph, up to $\Gamma = 10^{-2}$ (which corresponds to $10^{10}s^{-1}$), corresponds to values well within the expected physical range. This confirms that our optimal control strategies are robust under realistic dissipative conditions.

Comparing the different transitions, we observe that the behavior of $\hat{J}(u^*)$ is qualitatively similar across all three cases. However, there are slight variations in the point at which the degradation becomes significant. This suggests that the sensitivity to dissipation may depend on the specific transition being considered.

These results highlight the importance of minimizing dissipation in practical implementations of quantum battery charging protocols. Although optimal controls are robust against moderate levels of dissipation, excessive dissipation can severely impact charging efficiency. Therefore, careful consideration must be given to the environment interacting with the quantum battery system and operating conditions to minimize dissipative effects.

Combined Impact of Hopping and Dissipation on Optimal Control Performance

In the previous subsections, we analyzed the robustness of the optimal control strategies with respect to intermolecular hopping (t_h) and dissipation (Γ) separately. However, in realistic scenarios, both parameters can vary simultaneously, affecting the performance of the control. Therefore, in this subsection, we aim to visualize and analyze the combined impact of t_h and Γ on the cost functional $\hat{J}(u^*)$ using a 3D surface plot.

Specifically, we will examine how the joint variation of the hopping amplitude probability t_h and the charge hopping rate Γ influences the optimization performance of the precomputed optimal controls $u^*(t)$. To do this, we utilize the optimal control $u^*(t)$ obtained for the transitions $x_0 = 3 \rightarrow x_d = 5$, $x_0 = 3 \rightarrow x_d = 8$ and $x_0 = 3 \rightarrow x_d = 9$ in the absence of hopping and dissipation as an initial guess $u^0(t)$ for new simulations with the complete system dynamics, which now includes the terms for intermolecular hopping and dissipation. By varying t_h and Γ simultaneously, we can observe how the cost functional

$\hat{J}(u^*)$ deviates from its optimal value, providing insights into the combined sensitivity of the control to both parameters.

The resulting 3D surface plot will illustrate the regions of robustness and sensitivity, highlighting the interplay between hopping and dissipation in determining the overall performance of the quantum battery charging process.

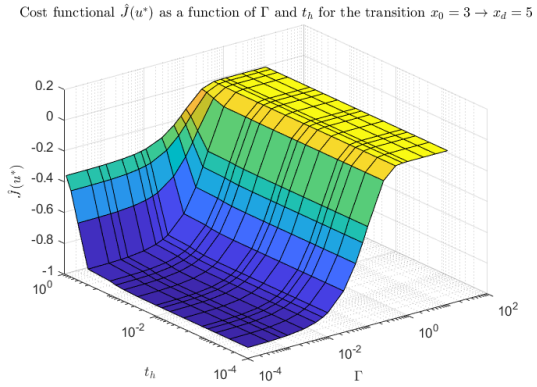

Figure 6.17: $x_0 = 3 \to x_d = 5$.

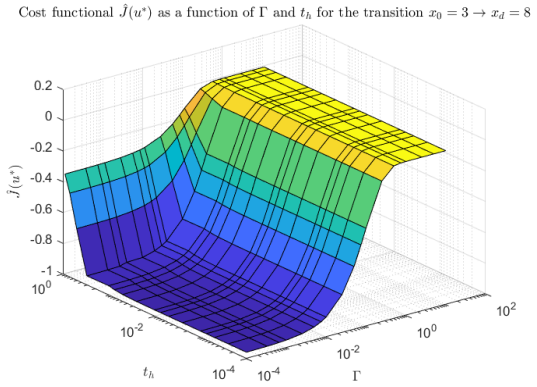

Figure 6.18: $x_0 = 3 \to x_d = 8$.

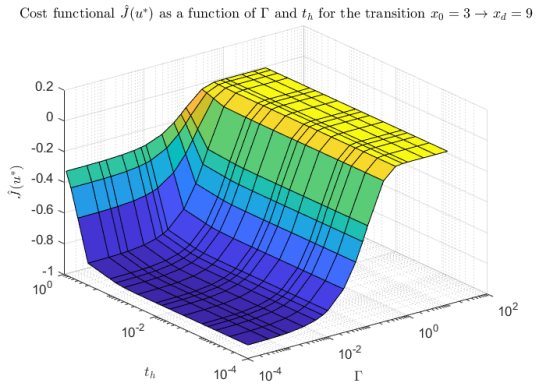

Figure 6.19: $x_0 = 3 \to x_d = 9$.

Figure 6.18 illustrates the combined impact of t_h and Γ on the cost functional $\hat{J}(u^*)$ for the transition $x_0 = 3 \to x_d = 8$. The plot reveals a region of robustness in the lower left corner, where $\hat{J}(u^*)$ remains close to its optimal value (around -1) for small values of both t_h and Γ. This indicates that the optimal control is effective when both intermolecular hopping and dissipation are weak.

As t_h and Γ increase, we observe a gradual degradation in the performance of the control, with $\hat{J}(u^*)$ deviating from its optimal value. However, the plot also shows that the control is more sensitive to variations in Γ than in t_h. Specifically, the degradation becomes more pronounced as Γ increases, even for relatively small values of t_h. This suggests that dissipation has a more significant impact on the performance of the control compared

to intermolecular hopping. The 3D surface plots for the transitions $x_0 = 3 \rightarrow x_d = 5$ and $x_0 = 3 \rightarrow x_d = 9$ (Figures 6.17 and 6.19) exhibit a qualitatively similar behavior, with a region of robustness at low values of t_h and Γ and a gradual degradation as both parameters increase. However, there are slight variations in the shape and extent of the robustness region, indicating that the sensitivity to hopping and dissipation may depend on the specific transition being considered.

These results highlight the importance of considering both intermolecular hopping and dissipation in the design of quantum battery charging protocols. While the optimal control strategies are robust against small variations in both parameters, larger deviations can significantly impact the charging efficiency. Therefore, careful consideration must be given to the specific system parameters and operating conditions to minimize both hopping and dissipation.

6.4.4. Effect of Intermolecular Hopping on State Connectivity

The introduction of the intermolecular hopping term $\hat{H}_{hop}$ into the Hamiltonian of the quantum battery system $\hat{H} = \hat{H}_0 + \hat{H}_{int}$ leads to significant changes in the connectivity between the eigenstates. To visualize this effect, we present in the figure below a series of network topology plots, each corresponding to a different value of the hopping parameter t_h. These graphs illustrate how the connectivity between eigenstates evolves as t_h increases, revealing the emergence of new connections that were absent in the system without hopping.

The adjacency graph in Fig. 6.20 illustrates the connectivity between states in the quantum battery system after the introduction of the intermolecular hopping term $\hat{H}_{hop}$. Similarly to the previous analysis without jumping, the nodes represent states and the edges indicate significant interactions, determined by the absolute values of the elements of the matrix $IAI + IBI$ exceeding a threshold of 10^{-8}. Comparing this graph with Fig. 6.1, we observe a notable increase in connectivity. The introduction of hopping leads to the emergence of numerous new edges, indicating enhanced interactions between previously disconnected states. This increased connectivity could suggest the potential for more efficient energy transfer and charging pathways within the quantum battery system. The graph highlights the structural changes induced by hopping, providing insights into how $\hat{H}_{hop}$ modifies the dynamics of the system and connectivity landscape.

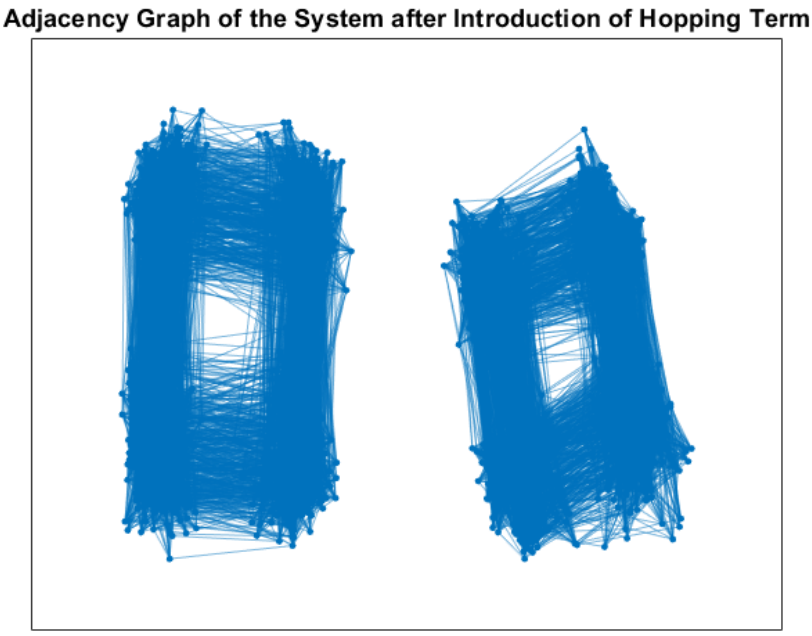

Figure 6.20: Adjacency graph of the quantum battery system after the introduction of the hopping term. Nodes represent states and edges indicate interactions exceeding a threshold of 10^{-8}.

Analysis of Hopping-Induced Transitions

The introduction of the intermolecular hopping term $\hat{H}_{hop}$ into the Hamiltonian of the system $\hat{H} = \hat{H}_0 + \hat{H}_{int}$ significantly alters the connectivity between the eigenstates. This can be observed by comparing the network topology in figures 6.21, 6.22, 6.23, 6.24, which show the evolution of connectivity with increasing t_h, with respect to the network topology in Figure 6.10, where only $\hat{H} = \hat{H}_0 + \hat{H}_{int}$ is considered. The emergence of new connections suggests the possibility of optimizing transitions between previously disconnected states, potentially unlocking new pathways for energy transfer and charging in the quantum battery.

To investigate the significance of these hopping-induced transitions, we selected several state pairs (x_0, x_d) that become connected only in the presence of $\hat{H}_{hop}$. We then attempted to optimize these transitions using the same gradient descent algorithm employed in previous sections. However, regardless of the value of t_h, including large values such as $t_h = 0.1$, the optimization process consistently failed to converge.

Specifically, we observed that the cost functional $\hat{J}(u^*)$ rapidly reached a value close to zero (e.g., 10^{-9}) within the first few iterations, and the gradient norm remained extremely

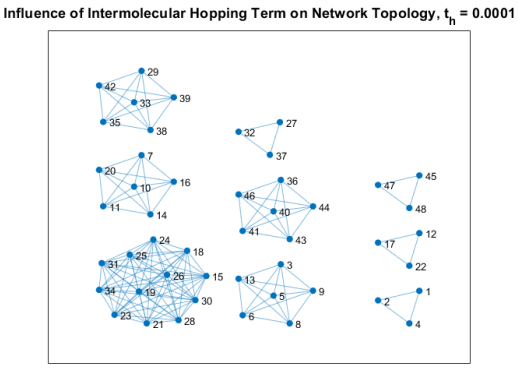

Figure 6.21: $t_h = 10^{-4}$.

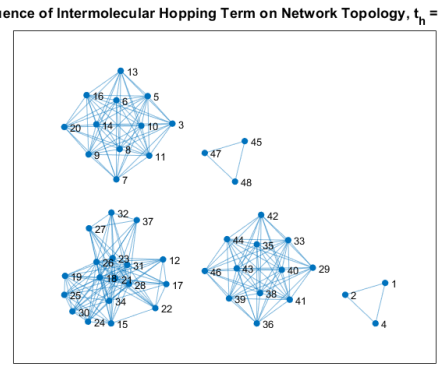

Figure 6.22: $t_h = 10^{-3}$.

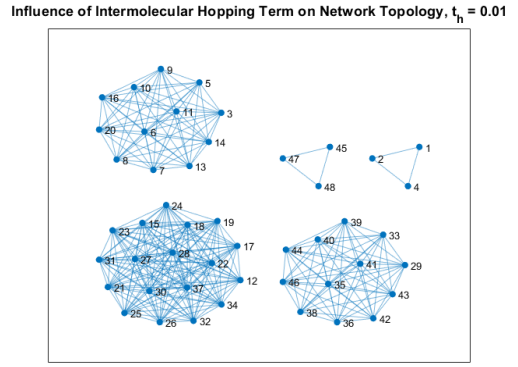

Figure 6.23: $t_h = 10^{-2}$.

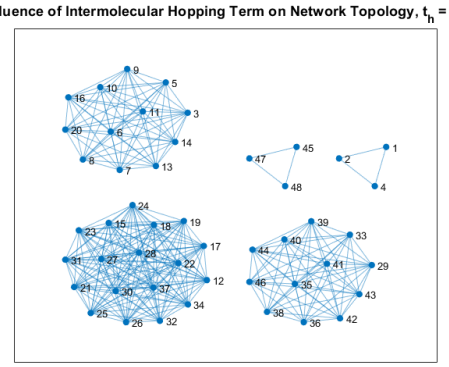

Figure 6.24: $t_h = 10^{-1}$.

low. This indicates that the algorithm quickly converged to a local minimum, suggesting that the hopping-induced connections represent weak transitions that are not energetically favorable.

In essence, while the intermolecular hopping term does create new connections between eigenstates, these connections appear to be "fictitious" in the sense that they do not lead to significant energy transfer or charging improvements. The optimization results suggest that the transitions between these newly connected states are inherently weak, and the system prefers to evolve along the pathways established by the original Hamiltonian $\hat{H} = \hat{H}_0 + \hat{H}_{int}$.

This analysis highlights the importance of not only considering the topological changes induced by hopping but also evaluating the energetic feasibility of the resulting transitions. While hopping can create new pathways, these pathways may not always be conducive to efficient quantum battery operation.

6.4.5. Optimization of Transitions with Hopping and Dissipation

This subsection presents the optimization of the transition $x_0 = 3 \rightarrow x_d = 5$, taking into account the complete dynamics of the system, including intermolecular hopping and dissipation effects. This analysis complements the previous robustness analysis by demonstrating the effectiveness of the optimal control strategy in the presence of both hopping and dissipation.

The dynamics are governed by the Liouvillian superoperator $\mathcal{L}$, represented in matrix form as $A = A_{\mathcal{L}_{\hat{H}_0}} + A_{\mathcal{L}_{\hat{H}_{int}}} + A_{\mathcal{L}[\hat{O}]} + A_{\mathcal{L}_{\hat{H}_{hop}}}$, where each term corresponds to a specific contribution to the dynamics of the system as referred in Section 3.1.1.

We utilize specific values for the probability amplitude of hopping t_h and the charge hopping rate Γ that fall within their respective robustness regimes, as established in the preceding analyses. This ensures that the optimization is performed under realistic and physically relevant conditions. More precisely, we will use a charge hopping rate $\Gamma = 1.0 \times 10^{-3}$ (in practice, $\Gamma = 10^9 \text{s}^{-1}$ and a hopping probability amplitude value $t_h = 1.0 \times 10^{-4}$.

Our goal is to maximize the transition probability from the initial state $x_0 = 3$ to the desired state $x_d = 5$, while minimizing the control effort. This is achieved by optimizing the cost functional $\hat{J}(u)$, which incorporates both the transition probability and a penalty term for the control field.

The graph in Fig.6.25 shows the convergence of the cost functional $\hat{J}$ as a function of the number of iterations. A rapid decrease of the cost functional is observed in the first iterations, followed by a gradual convergence towards a stable value. This indicates that the optimization algorithm successfully finds a control strategy that maximizes the transition probability.

The plot in Fig.6.26 illustrates the convergence of the gradient norm $\|\nabla_u \hat{J}(u)\|_\infty$ as a function of the iteration number. The gradient norm gradually decreases and stabilizes at a low value, confirming the convergence of the optimization algorithm towards a minimum of the cost functional $\hat{J}$.

Fig.6.27 shows the evolution of the energy E of the molecular subsystem during the optimization process. The energy increases rapidly in the first iterations and then converges to a stable value, indicating that the control field effectively drives the system towards the desired state.

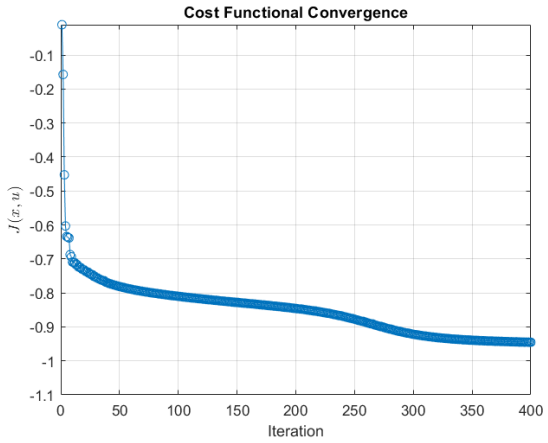

Figure 6.25: Evolution of $\hat{J}(u)$ over iterations for transition $x_3 \to x_5$.

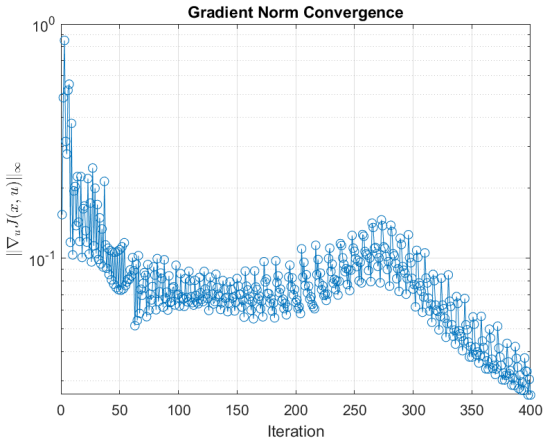

Figure 6.26: Evolution of $\|\nabla_u \hat{J}(u)\|_\infty$ over iterations for transition $x_3 \to x_5$.

Figure 6.28 illustrates the trajectory of the optimal control $u^*(t)$ as a function of time t. In particular, two pronounced peaks occur at the beginning and midpoint of the optimization process, succeeded by a sequence of damped oscillations. This pattern suggests that optimal control necessitates an intense application at the initial and mid-stages of the charging process, followed by a more precise modulation to sustain the optimal charge.

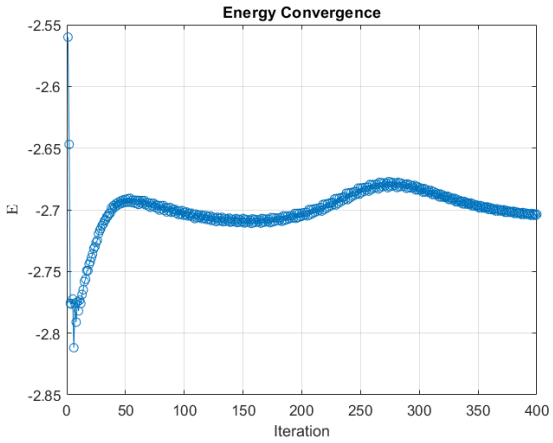

Figure 6.27: Evolution of energy $E(T)$ over iterations for transition $x_3 \rightarrow x_5$.

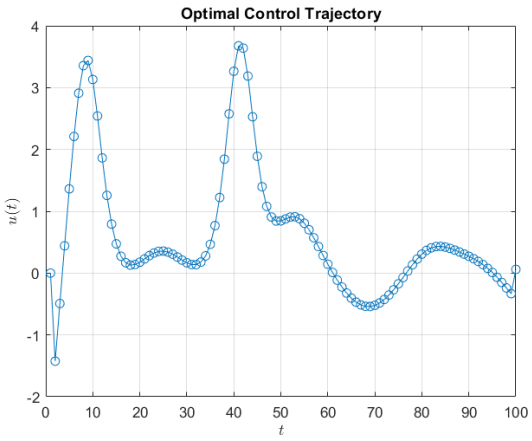

Figure 6.28: Optimal control $u^*(t)$ for transition $x_3 \rightarrow x_5$.

6.4.6. Optimization of Battery Charge

This subsection presents the final optimization experiment focused on maximizing the overall charge of the quantum battery. Unlike the previous subsection, which targeted a specific state transition, this experiment aims to maximize the expectation value of the molecular Hamiltonian, including the hopping term, given by $\langle \rho(T), \left(\hat{H}_{mol} + \hat{H}_{hop}\right) \otimes \hat{I}_{cav} \rangle$.

To achieve this, we utilize the vector c, which represents the coefficients of the molecular Hamiltonian in the chosen basis. As shown in Equation 4.10, this expectation value can be expressed as $c^T x(T)$, where $x(T)$ is the vector of state coefficients at the final time T. Therefore, by maximizing $c^T x(T)$, we effectively maximize the overall charge of the battery.

Similar to the previous experiment, we consider the complete system dynamics, including intermolecular hopping and dissipation effects, that is, the dynamics are governed by the Liouvillian superoperator $\mathcal{L}$, represented in matrix form as $A = A_{\mathcal{L}_{\hat{H}_0}} + A_{\mathcal{L}_{\hat{H}_{int}}} + A_{\mathcal{L}[\hat{O}]} + A_{\mathcal{L}_{\hat{H}_{hop}}}$.

We utilize the same values for the probability amplitude of hopping t_h and the charge hopping rate Γ that were used in the previous subsection. These values fall within their respective robustness regimes, ensuring that the optimization is performed under realistic and physically relevant conditions.

Our goal is to find the optimal control signal $u^*(t)$ that maximizes the final charge of the battery, represented by $c^T x(T)$, while minimizing the control effort. This is achieved by optimizing the cost functional $\hat{J}(u)$, which incorporates both the final charge and a penalty term for the control field.

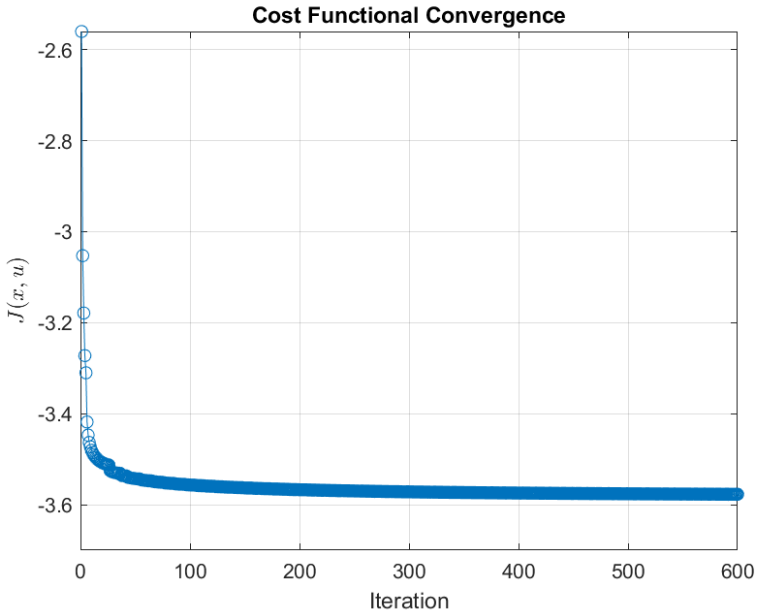

Figure 6.29: Convergence of the cost functional $\hat{J}(u)$ during the optimization of battery charge.

The convergence of the cost functional $\hat{J}(u)$ is represented in Fig. 6.29 as a function of the number of iterations. Since the cost functional in this case reflects the energy stored in the battery, its convergence demonstrates the effectiveness of the optimal control strategy in enhancing battery charge. The gradient descent algorithm successfully minimized the cost functional $\hat{J}(u) = c^T x(T) + \frac{\nu}{2}\|u\|^2_{L^2(0,T)}$.

The graph shows a rapid decrease in the initial iterations, indicating a quick improvement in battery charge. This is followed by a gradual convergence towards a stable value of

approximately -3.58 eV. In particular, this final energy value exceeds the energy level of the state x_9 (as observed in Table 6.2), which was the highest energy state reached in the state transition experiments starting from $x_0 = 3$. This result highlights a key advantage of optimal control: it enables the system to surpass the energy limits imposed by direct transitions between eigenstates. The optimal control $u^*(t)$ effectively guides the system to a local minimum in the energy landscape, corresponding to a state with an energy higher than that of x_9, an eigenstate of the Hamiltonian $(\hat{H}_{mol} + \hat{H}_{hop}) \otimes \hat{I}_{cav}$. This behavior demonstrates the algorithm's ability to efficiently find an optimal control strategy that goes beyond simple state-to-state transitions, maximizing the energy storage in the quantum battery system by accessing a state not directly reachable through those transitions.

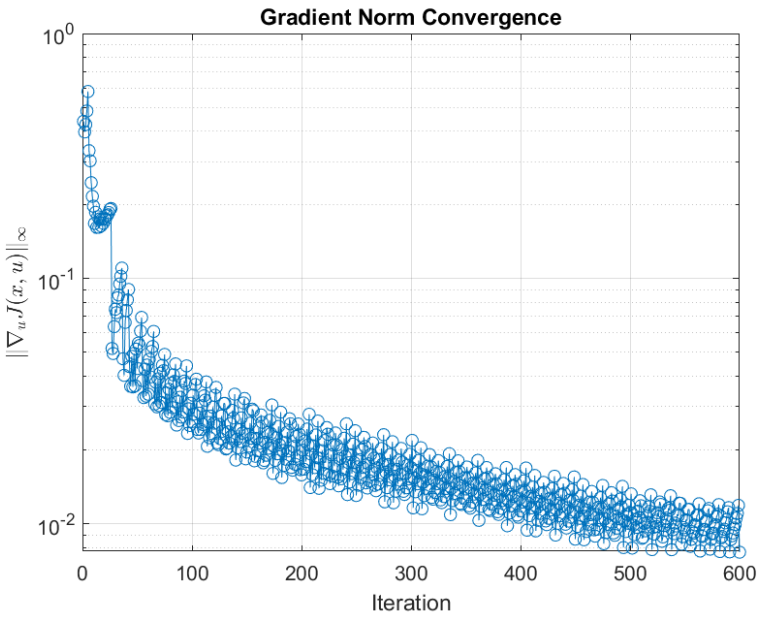

Figure 6.30: Convergence of the gradient norm $\|\nabla_u \hat{J}(u)\|_\infty$ during the optimization of battery charge.

Figure 6.30 illustrates the convergence of the gradient norm $\|\nabla_u \hat{J}(u)\|_\infty$ as a function of the number of iterations. The gradient norm exhibits a rapid decrease in initial iterations, followed by a gradual convergence towards a low value close to $7,7 \times 10^{-3}$. This behavior indicates that the optimization algorithm successfully converges to a stationary point of the cost functional. The oscillations observed during the convergence process suggest the complexity of the functional cost landscape.

Figure 6.31 shows the trajectory of the optimal control $u^*(t)$ as a function of time. The control exhibits two significant peaks at the beginning of the optimization process, followed

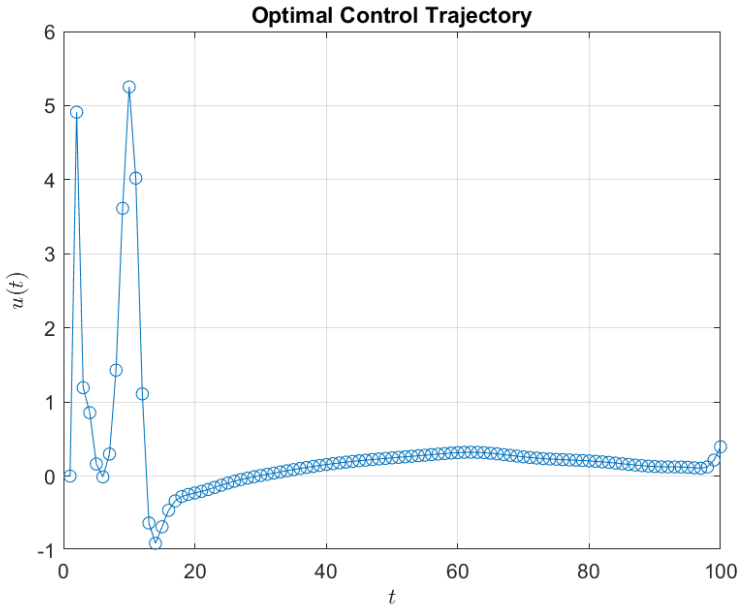

Figure 6.31: Optimal control trajectory $u^*(t)$ for maximizing battery charge.

by a series of damped oscillations and a convergence to a low value close to zero. This pattern suggests that optimal control requires intense application in the initial stages to initiate the charging process, followed by fine modulation to maintain the optimal charge. The complex shape of the control signal indicates the non-linear nature of the charging process and the need for precise control dynamics.

7 | Contribution of the Study and Conclusions

This thesis investigated the possibility of maximizing the charging process of a quantum battery using a time-driving field, with the ultimate goal of achieving energy levels capable of powering electronic devices. Although computational limitations prevented us from fully reaching this ambitious goal, our study nonetheless provides important contributions to the computational field of quantum battery research.

First, we successfully demonstrated the feasibility of controlled energy excitations within the quantum battery system. Using a time-driving field, we achieved targeted transitions between eigenstates, effectively transferring energy to the battery. This result confirms the potential for the use of optimal control techniques to manipulate and enhance the charging process in quantum batteries. However, the observation that even in the smallest system considered ($N_p = 2, M = 3$), achieving large energy transitions proved difficult, raises questions about the efficiency of the time-driving field mechanism for this specific application. While our approach demonstrates the capability of inducing energy transitions, it also highlights the limitations in achieving substantial energy transfer, particularly when scaling to larger systems.

Furthermore, our in-depth analysis of the dynamics of the system revealed crucial insights into the interplay between intermolecular hopping, dissipation and state connectivity. We identified regimes of robustness where the optimal control strategies remain effective despite the presence of these factors. This knowledge is essential for designing practical quantum battery charging protocols that can operate reliably under realistic conditions.

Finally, our study also sheds light on the limitations of the time-driving field approach for maximizing quantum battery charging in computationally constrained scenarios. Although we achieved energy transfer, scaling to levels required for practical applications presents a significant challenge. This finding highlights the need for further research into alternative control strategies or more efficient computational methods.

In conclusion, although the initial goal of achieving a fully charged quantum battery

was not reached, this thesis provides valuable contributions to the understanding and development of quantum battery technologies. Our findings provide a valuable foundation for future research, suggesting potential avenues for addressing the identified limitations and further exploring the capabilities of quantum batteries.

7.1. Research Perspectives

The findings of this study open several avenues for future research. Firstly, exploring alternative control mechanisms beyond the time-driving field approach could lead to more efficient and scalable methods for maximizing quantum battery charging. This could involve investigating different types of control fields, optimization algorithms, or even exploring hybrid classical-quantum control strategies as in [10].

Specifically, as a future step, it would be interesting to perform a Fourier decomposition of the optimal control signals $u^*(t)$ obtained in this work. This analysis would provide insights into the frequency components of these signals, which is particularly relevant for experimental implementation using laser pulses. Understanding the frequency spectrum could reveal potential pathways or resonances that enhance the charging process.

Furthermore, exploring the bias voltage V_b as a control parameter presents a promising direction for further research. Since V_b appears within the Fermi-Dirac functions in the bath-correlation functions of the Lindblad superoperators, it plays a crucial role in energy transfer to the system. Investigating optimal control strategies with multiple control parameters, including both $\eta(t)$ and $V_b(t)$, could lead to significant improvements in the charging process. This would involve solving optimal control problems with $N_C > 1$, where V_b could also be time-dependent.

Secondly, developing more efficient computational methods and leveraging advanced computing resources could enable the simulation of larger and more complex quantum battery systems. This would allow for a more comprehensive exploration of the parameter space and potentially uncover pathways to achieve higher energy storage capacities. Finally, investigating the practical aspects of extracting and utilizing the stored energy in quantum batteries is crucial. This includes exploring methods for converting quantum energy into usable electrical charge and developing prototypes of quantum battery-powered devices.

Bibliography

[1] A. Borzì. *The Sequential Quadratic Hamiltonian Method: Solving Optimal Control Problems (1st ed.)*. Chapman and Hall/CRC, 2023. doi: https://doi.org/10.1201/9781003152620.

[2] A. Borzì, G. Ciaramella, and M. Sprengel. *Formulation and Numerical Solution of Quantum Control Problems*. Society for Industrial and Applied Mathematics, Philadelphia, PA, 2017. doi: 10.1137/1.9781611974843. URL `https://epubs.siam.org/doi/abs/10.1137/1.9781611974843`.

[3] H.-P. Breuer and F. Petruccione. *The Theory of Open Quantum Systems*. Oxford University Press, New York, 2005. ISBN 9780199213900. doi: 10.1093/acprof:oso/9780199213900.001.0001.

[4] G. Ciaramella and A. Borzì. Skryn: A fast semismooth-krylov-newton method for controlling ising spin systems. *COMPUTER PHYSICS COMMUNICATIONS*, 190: 11, 2015. doi: https://dx.doi.org/10.1016/j.cpc.2015.01.006. URL `https://hdl.handle.net/11311/1193340`.

[5] G. Ciaramella, A. Borzì, G. Dirr, and D. Wachsmuth. Newton methods for the optimal control of closed quantum spin systems. *SIAM Journal on Scientific Computing*, 37(1):A319–A346, 2015. doi: 10.1137/140966988. URL `https://doi.org/10.1137/140966988`.

[6] F. Elste and C. Timm. Theory for transport through a single magnetic molecule: Endohedral N@c_{60}. *Phys. Rev. B*, 71:155403, Apr 2005. doi: 10.1103/PhysRevB.71.155403. URL `https://link.aps.org/doi/10.1103/PhysRevB.71.155403`.

[7] D. Ferraro, M. Campisi, G. M. Andolina, V. Pellegrini, and M. Polini. High-power collective charging of a solid-state quantum battery. *Phys. Rev. Lett.*, 120:117702, Mar 2018. doi: 10.1103/PhysRevLett.120.117702. URL `https://link.aps.org/doi/10.1103/PhysRevLett.120.117702`.

[8] K. Hymas and A. Soncini. Mechanisms of spin-charge conversion for the electrical readout of $4f$ quantum states in a $tbpc_2$ single-molecule magnet spin transistor. *Phys.*

Rev. B, 102:045313, Jul 2020. doi: 10.1103/PhysRevB.102.045313. URL https://link.aps.org/doi/10.1103/PhysRevB.102.045313.

[9] K. Hymas and A. Soncini. Origin of the hysteresis of magnetoconductance in a supramolecular spin-valve based on a $Tbpc_2$ single-molecule magnet. *Phys. Rev. B*, 102:125310, Sep 2020. doi: 10.1103/PhysRevB.102.125310. URL https://link.aps.org/doi/10.1103/PhysRevB.102.125310.

[10] J. Li, X. Yang, X. Peng, and C.-P. Sun. Hybrid quantum-classical approach to quantum optimal control. *Phys. Rev. Lett.*, 118:150503, Apr 2017. doi: 10.1103/PhysRevLett.118.150503. URL https://link.aps.org/doi/10.1103/PhysRevLett.118.150503.

[11] J. Q. Quach and W. J. Munro. Using dark states to charge and stabilize open quantum batteries. *Phys. Rev. Appl.*, 14:024092, Aug 2020. doi: 10.1103/PhysRevApplied.14.024092. URL https://link.aps.org/doi/10.1103/PhysRevApplied.14.024092.

[12] J. Q. Quach, K. E. McGhee, L. Ganzer, D. M. Rouse, B. W. Lovett, E. M. Gauger, J. Keeling, G. Cerullo, D. G. Lidzey, and T. Virgili. Superabsorption in an organic microcavity: Toward a quantum battery. *Science Advances*, 8(2):eabk3160, 2022. doi: 10.1126/sciadv.abk3160. URL https://www.science.org/doi/10.1126/sciadv.abk3160.

[13] C. Timm and F. Elste. Spin amplification, reading, and writing in transport through anisotropic magnetic molecules. *Phys. Rev. B*, 73:235304, Jun 2006. doi: 10.1103/PhysRevB.73.235304. URL https://link.aps.org/doi/10.1103/PhysRevB.73.235304.

[14] J. Wiercinski, E. M. Gauger, and M. Cygorek. Phonon coupling versus pure dephasing in the photon statistics of cooperative emitters. *Phys. Rev. Res.*, 5:013176, Mar 2023. doi: 10.1103/PhysRevResearch.5.013176. URL https://link.aps.org/doi/10.1103/PhysRevResearch.5.013176.

[15] M. A. Zeb, P. G. Kirton, and J. Keeling. Incoherent charge transport in an organic polariton condensate. *Phys. Rev. B*, 106:195109, Nov 2022. doi: 10.1103/PhysRevB.106.195109. URL https://link.aps.org/doi/10.1103/PhysRevB.106.195109.

List of Figures

2.1 A schematic representation of the four possible states for each molecule. . . 10
2.2 A schematic illustration for electrons creation/annihilation operators . . . 13
2.3 A schematic representation of open quantum system. 20
2.4 Schematic representation of the quantum battery model, illustrating the coupling between the battery and the electrodes. The system consists of N_p molecular sites (blue circles) representing the quantum battery, connected to a source and drain electrode. The electrodes are modeled as fermionic reservoirs with a bias voltage V_b applied between them, creating a difference in their Fermi levels (ϵ_F). The arrows indicate the flow of electrons (e^-) between the electrodes and the molecular sites, highlighting the charging and discharging processes. The red and green arrows represent electron transfer from the source to the battery, while the orange and purple arrows represent electron transfer from the battery to the drain. 23

3.1 Sparsity pattern of $A_{\mathcal{L}_{\hat{H}_0}}$: visualization of the matrix structure related to the free Hamiltonian, ($N_p = 2, M = 3$). 37
3.2 Sparsity pattern of $A_{\mathcal{L}_{\hat{H}_{int}}}$: visualization of the structure of the matrix related to the interaction Hamiltonian, ($N_p = 2, M = 3$). 37
3.3 Sparsity pattern of $A_{\mathcal{L}[O]}$: visualization of the matrix structure related to Lindblad superoperators, ($N_p = 2, M = 3$). 38
3.4 Sparsity pattern of $A_{\mathcal{L}_{\hat{H}_{hop}}}$: visualization of the matrix structure related to the hopping Hamiltonian, ($N_p = 2, M = 3$). 38
3.5 Structure of A: the sparsity pattern reveals how the components of the free Hamiltonian, the interaction Hamiltonian and the Lindblad superoperators contribute to the dynamic matrix, ($N_p = 2, M = 3$). 40
3.6 Structure of the B matrix: sparsity pattern that highlights coupling with external control, ($N_p = 2, M = 3$). 41

4.1 The schematic represents a simplified model of a quantum battery and its control process. The goal is to show how an input control signal $u^0(t)$ influences the state of the battery, leading to a desired output signal $u^*(t)$. 53

6.1 Adjacency graph representing the connectivity between states in the quantum battery system. Nodes represent states and edges indicate interactions exceeding a threshold of 10^{-8}. 68
6.2 $A + B$ showed before the permutation. 69
6.3 $A + B$ showed after the permutation. 69
6.4 Submatrix of A for the primary connected block. 69
6.5 Submatrix of B for the primary connected block. 69
6.6 Spectrum of matrix A. 71
6.7 Some examples of components of $y(t)$ during free evolution. In top-left, top-middle and top-right we can see the evolutions of the components $y_2(t) = Ax_2(t)$ and $y_9(t) = Ax_9(t)$ which stabilize over time. Instead, in bottom-left, bottom-middle and bottom-right there are the evolutions of $y_{1584}(t) = Ax_{1584}(t)$ and $y_{1728}(t) = Ax_{1728}(t)$ which are oscillating over time. 72
6.8 Norm $\|y(t)\|$ evolution over time. 73
6.9 Norm derivative $\frac{d}{dt}\|y(t)\|$ over time. 74
6.10 Network topology of the system without hopping and dissipation. 79
6.11 Evolution of $\hat{J}(u)$ over iterations for transition $x_3 \to x_8$. 82
6.12 Evolution of $\|\nabla_u \hat{J}(u)\|_\infty$ over iterations for transition $x_3 \to x_8$. 82
6.13 Evolution of energy $E(T)$ over iterations for transition $x_3 \to x_8$. 82
6.14 Optimal control $u^*(t)$ for transition $x_3 \to x_8$. 82
6.15 Variation of the cost functional $\hat{J}(u^*)$ as a function of the hopping probability amplitude t_h (eV) for the transitions $x_0 = 3 \to x_d = 5$, $x_0 = 3 \to x_d = 8$ and $x_0 = 3 \to x_d = 9$. 86
6.16 Variation of the cost functional $\hat{J}(u^*)$ as a function of the charge hopping rate Γ (s^{-1}) for the transitions $x_0 = 3 \to x_d = 5$, $x_0 = 3 \to x_d = 8$ and $x_0 = 3 \to x_d = 9$. 87
6.17 $x_0 = 3 \to x_d = 5$. 89
6.18 $x_0 = 3 \to x_d = 8$. 89
6.19 $x_0 = 3 \to x_d = 9$. 89
6.20 Adjacency graph of the quantum battery system after the introduction of the hopping term. Nodes represent states and edges indicate interactions exceeding a threshold of 10^{-8}. 91
6.21 $t_h = 10^{-4}$. 92

6.22 $t_h = 10^{-3}$. 92
6.23 $t_h = 10^{-2}$. 92
6.24 $t_h = 10^{-1}$. 92
6.25 Evolution of $\hat{J}(u)$ over iterations for transition $x_3 \to x_5$. 94
6.26 Evolution of $\|\nabla_u \hat{J}(u)\|_\infty$ over iterations for transition $x_3 \to x_5$. 94
6.27 Evolution of energy $E(T)$ over iterations for transition $x_3 \to x_5$. 95
6.28 Optimal control $u^*(t)$ for transition $x_3 \to x_5$. 95
6.29 Convergence of the cost functional $\hat{J}(u)$ during the optimization of battery charge. 96
6.30 Convergence of the gradient norm $\|\nabla_u \hat{J}(u)\|_\infty$ during the optimization of battery charge. 97
6.31 Optimal control trajectory $u^*(t)$ for maximizing battery charge. 98

List of Tables

6.1 Results for selected transitions with $\Gamma = 0$ and $t_h = 0$, effectively simulating a closed quantum system without hopping. For these specific transitions, the maximum number of iterations has been set set to 80 and the tolerance on the convergence of the cost functional gradient to $1,0 \times 10^{-6}$. 81

6.2 Results for selected transitions with $\Gamma = 0$ and $t_h = 0$, effectively simulating a closed quantum system without hopping. This table is specifically focusing on transitions involving the matter part of the battery, starting from the ground state $x_0 = 3$. We considered for these transitions a maximum number of iterations parameter equal to 2000 and the tolerance on the convergence of the cost functional gradient equal to $1,0 \times 10^{-4}$. 81

Acknowledgements

I wanted to express my extreme gratitude to all the people who have been by my side over the years and supported me with their help.

I would like to first thank Professor Gabriele Ciaramella for the time and energy he dedicated to me, for everything he taught me, and for the patience he had.

I would like to thank Dr. Kieran Hymas, for his support and knowledge in the field of quantum batteries and for the efforts made, despite a distance of 16.000 km.

In particular, I thank my parents Ambrogio and Elena, my sister Noemi, my girlfriend Ylenia, my grandmother Marisa, my cousin Samuele, my uncles Paolo and Antonella, and all my friends for the help they gave me during the journey. They were all fundamental in this five-year journey with their moral and emotional support.

I would also like to thank those who are no longer here but will always be with me, my grandfather Mario and my uncle Marco; they will never be forgotten.

Finally, I would like to thank myself for never giving up despite all the difficulties I encountered along the way.